Vortex lattice in conventional and unconventional superconductors

by

Louis Lemberger

A thesis submitted to
The University of Birmingham
for the degree of
DOCTOR OF PHILOSOPHY

Quantum Matter Group
School of Physics and Astronomy
College of Engineering and Physical Sciences
The University of Birmingham

January 2016

Abstract

This thesis presents the work done to characterise two superconducting materials.

We study BiPd, a non-centrosymmetric superconductor which is theoretically expected to show signs of spin singlet and triplet mixing due to the strong spin-orbit scattering of its composing elements. We map the field-temperature superconducting phase diagram along two crystal directions using Small Angle Neutron Scattering (SANS), magnetisation and μSR measurements and determine the microscopic parameters defining the superconducting state. We also uncover a rare behaviour displayed in low-κ superconductors, the Intermediate Mixed State, which causes domains of vortex lattice with constant spacing to coexist with Meissner domains at low applied fields. Finally we show evidence that, unlike what was expected, the superconductivity in BiPd behaves conventionally.

The second material studied is Nb_3Sn, widely used to produce large magnetic fields in various devices such as MRI machines. We investigate the superconducting state of several polycrystalline samples with different tin concentrations, as recent evidence point towards a lack of change of the upper critical field with varying Sn doping, in contradiction with older measurements that see a drop in H_{c2} associated with the apparition of a structural (martensitic) crystalline transition. Using SANS, we show that these recent results were likely not measuring the bulk state of Nb_3Sn and that we find large variation of H_{c2} with Sn concentration. We also present indications that the vortex lattice is influenced by non-local effects at large fields by measuring the change in the vortex lattice structure with field. Lastly, our measurements are consistent with a full single gap behaviour in Nb_3Sn.

ACKNOWLEDGEMENTS

I would like to acknowledge Elizabeth Blackburn, Ted Forgan, Charles Dewhurst and Bob Cubitt for giving me the opportunity to take on this PhD. I have greatly enjoyed this period of my life under their guidance, it has been an invaluable learning experience. I would also like to address many thanks to the scientists collaborating with our group as well as the support staff without whom all of this would not have been possible.

Special thanks go to Alex Holmes for his finely honed restaurant recommendation skills, but also for the countless explanations he was kind enough to give me.

In no particular order, I acknowledge Alistair, Josh, Bindu, George, Randeep, Lingjia, Erik, Filippo, Arvid and many more staff and students from the University of Birmingham for the (mostly) interesting discussions and numerous curry expeditions that were carried out.

From my stay in Grenoble, I will fondly remember the silly conversations and crazy adventures with Eron, Ramona, Marco, Diane, Pierre, Eva, Airidas, Ingo, Ida, Alexis and many others.

Finally, I will be forever grateful for the support my friends and family always provided to me.

CONTENTS

LIST OF FIGURES

LIST OF TABLES

CHAPTER 1

INTRODUCTION

1.1 Superconductivity

Superconductivity was discovered by H.K. Onnes, an experimental physicist at the University of Leiden who was the first to achieve the liquefaction of helium in 1908, with a process based on adiabatic expansion of the gas. Interested in studying the behaviour of materials at low temperatures, in 1911 he measured a sudden drop in the resistance of mercury below a critical temperature $T_c = 4.2$ K, shown in figure 1.1.

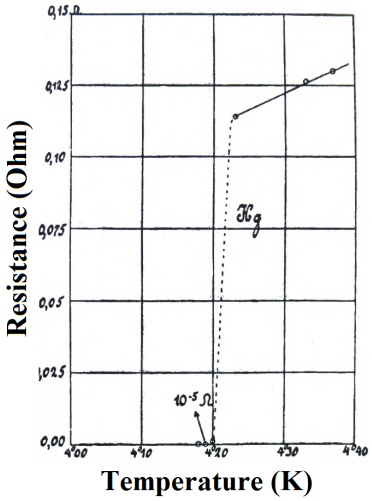

Figure 1.1: Resistance versus temperature of mercury. From Wysokinski [1]

1.1.1 London theory

This was the first observation of superconductivity, which was at that time only understood as perfect conductivity. Using the Drude theory [2] (1900) of an electron gas with a mean free time to the next collision

τ, carrier charge q and mass m

$$m\,\frac{d\boldsymbol{v}}{dt} + \frac{\boldsymbol{v}}{\tau} = -q\,\boldsymbol{E}$$

For a perfect conductor there are no collisions ($\tau \to \infty$) so the drag term is non-existent. Introducing the charge carrier density n and current density $\boldsymbol{j} = -n\,q\,\boldsymbol{v}$ the previous equation yields

$$\frac{\partial \boldsymbol{j}}{\partial t} = \frac{nq^2}{m}\boldsymbol{E}$$

Using Maxwell's equations, this leads to the following equation describing the behaviour of the magnetic field inside the sample

$$\nabla^2\left(\frac{\partial \boldsymbol{B}}{\partial t}\right) = \lambda_L^{-2}\frac{d\boldsymbol{B}}{dt}$$

which means that the time derivative of the magnetic field decays exponentially with a characteristic length-scale λ_L, called the London penetration depth. As a consequence, deep inside the sample for $x \gg \lambda$,

$$\frac{d\boldsymbol{B}}{dt} = 0 \quad \therefore \quad B = constant$$

This shows that a perfect conductor tends to trap the magnetic flux inside the sample, because any time variation of magnetic field is screened. Meissner and Ochsenfeld [3] observed contradictory behaviour in 1933, when they saw expulsion of field, or perfect diamagnetism, in superconductors below a critical temperature T_c (illustrated in figure 1.2) and critical field H_c, above which the superconducting state is suppressed.

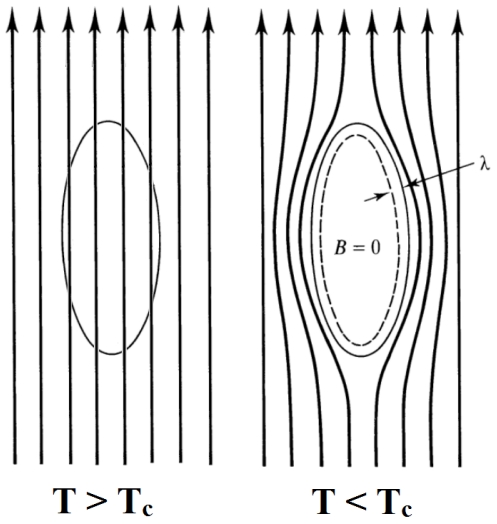

Figure 1.2: Illustration of the Meissner-Ochsenfeld effect in superconductors. Adapted from Tinkham [4]

Indeed, if a magnetic field is applied above T_c and the material is cooled, the value of the field inside the superconductor changes with time and contradicts the previous statement $\frac{d\boldsymbol{B}}{dt} = 0$.
London and London [5] proposed in 1935 to modify the previous equation to account for this effect:

$$\nabla^2 \boldsymbol{B} = \lambda_L^{-2} \boldsymbol{B}$$

leading to

$$\boldsymbol{B} \propto e^{-\frac{x}{\lambda_L}} \quad \text{with} \quad \lambda_L = \sqrt{\frac{m}{\mu_0\, n\, q^2}}$$

x being defined as the distance in the superconducting material from its surface, we see that absolute value of the magnetic field is screened over a length λ_L by the flow of superconducting electrons (supercurrents), characterised by the following relationship

$$\boldsymbol{j} = -\frac{1}{\mu_0\, \lambda_L^2}\, \boldsymbol{A}$$

which is the equivalent of Ohm's law $\boldsymbol{j} = \sigma\, \boldsymbol{E} = -\sigma\, \frac{d\boldsymbol{A}}{dt}$ in metals (valid in the London gauge $\boldsymbol{\nabla . A} = 0$).

1.1.2 Ginzburg-Landau theory

In 1950, Ginzburg and Landau formulated a phenomenological explanation of superconductivity derived from the phase transition theory [6], where the superconducting state is defined by an order parameter (OP) which goes to zero above T_c:

$$\Psi = \sqrt{n(r,t)}\, e^{i\, \theta(r,t)}$$

This represents the macroscopic wave function describing the superconducting phase, with the superfluid density n and an associated phase θ.
Ginzburg-Landau (GL) theory assumes that the expression of the Helmholtz free energy F near the superconducting transition is analytical and can be expanded as a function of even powers of Ψ

$$F_s - F_n = \alpha\, |\Psi|^2 + \frac{\beta}{2}\, |\Psi|^4 + \frac{1}{2\, m} \left| (\frac{\hbar}{i} \boldsymbol{\nabla} - q\, \boldsymbol{A})\, \Psi \right|^2 + \frac{H_c^2}{2\, \mu_0}$$

The penultimate term represents the kinetic energy of the charge carriers of mass m and charge q, and the

last is associated with the energy cost of magnetic field expulsion from the system.

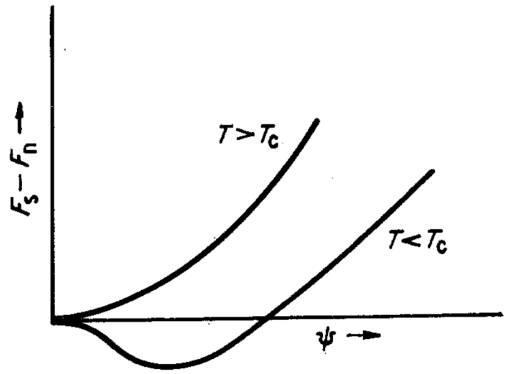

Figure 1.3: Free energy versus order parameter at zero field. From Cyrot [7]

Minimising this expression with the assumption that the amplitude of the OP is spatially uniform ($|\Psi| = \sqrt{n}$), so that any variation of the OP is due to its phase, the current density takes the form:

$$\boldsymbol{j} = \frac{q}{m}(\hbar \boldsymbol{\nabla}\theta - q\,\boldsymbol{A})\,|\Psi|^2$$

We can see that if $\nabla\theta = 0$, we find the equation linking $\boldsymbol{j}$ and $\boldsymbol{A}$ we previously established. This is called the rigidity of the wavefunction: a superconductor with a uniform OP with a constant phase is described by the London theory.

Additional parameters arise from the Ginzburg-Landau theory:

$$\lambda = \sqrt{\frac{m\,\beta}{q^2 \mu_0\ |\alpha|}} \text{ equivalent to the London penetration depth } \lambda_L \text{ if } \frac{|\alpha|}{\beta} = n$$

and

$$\xi = \frac{\hbar}{\sqrt{2\,m\ |\alpha|}} \text{ the coherence length}$$

As previously seen, λ is the first characteristic length of a superconductor and describes the decay the magnetic field inside the material. In the same fashion, the second lengthscale ξ is the parameter that governs the variation of the superfluid density, defining the lengthscale over which the superconductivity varies or is established. The situtation is pictured in figure 1.4.

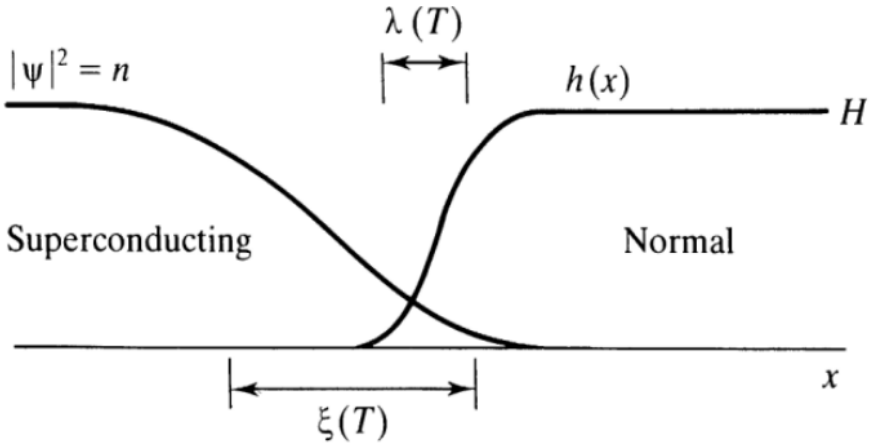

Figure 1.4: Interface between a superconducting and normal domain, from Tinkham [4]

These parameters have a temperature dependence: in the superconducting state, in order for the system to have an analytical solution, α and β are chosen so that:

$$\alpha = -\alpha_0 \, (T - T_c) \quad \text{and} \quad \alpha_0 \, , \, \beta > 0$$

This leads to both superconducting parameters diverging as $T \to T_c$ in the form

$$\xi(T) \, , \lambda(T) \propto (T - T_c)^{-\frac{1}{2}}$$

1.1.3 BCS theory

The importance of the lattice vibrations in the formation of superconductivity was suggested in 1950 by Fröhlich [8] and later experimentally confirmed [9] by observing the isotope effect:

$$H_c \, , T_c \approx M^{-\frac{1}{2}} \approx k_B \, \Theta_D$$

In many superconductors, the presence of phonons leads to an attractive electron-electron interaction. If it is larger than the screened Coulomb repulsion between electrons, the resulting interaction is attractive. The classical picture is that electrons feel a retarded effect of the perturbation of the lattice by other electrons previously walking in their path, the mass of the atoms M having a direct effect on the strength of the interaction.

Subsequently, Cooper showed [10] that two electrons above the Fermi energy E_F will form a bound state with a lower energy in the presence of an arbitrary small attractive interaction.

Following this, Bardeen, Cooper and Schrieffer proposed in 1957 a microscopic theory of superconductivity [11], applying the previous results to a many-body framework.

The attractive electron-electron interaction is mediated by the exchange of a virtual (i.e. short-lived) phonon and the energy change due to this scattering is proportional to $(\hbar\omega - \hbar\omega_D)^{-1}$. This motivates the cutoff energy $\hbar\omega_D = k_B\,\Theta_D$ used to calculate the matrix elements $-V$ of the interaction potential [12], as the energy change becomes positive when $\hbar\omega > \hbar\omega_D$. This cutoff corresponds to the Debye energy, which is the energy required to excite all phonons modes in a crystal.

In the superconducting state, it is energetically favourable for the system to form the previously mentioned bound states (called Cooper pairs), as the energy gain per pair is

$$\frac{\delta\, E}{n_{cp}} \approx \frac{\Delta^2}{E_F} \quad \text{with } n_{cp} \text{ the number of Cooper pairs}$$

In the normal state at $T = 0$, it costs an energy $|E - E_f|$ to put an electron in an excited state because of the Pauli principle. In the superconducting state, this energy cost becomes $\sqrt{(E - E_f)^2 + \Delta^2}$, which means that there is a minimum excitation energy which corresponds to the binding energy of a Cooper pair, or the amount of energy required to break one.

As a result, the system opens a gap 2Δ in the band structure at the Fermi level. It is commonly measured used tunnelling spectroscopy, the first measurement performed by Giaever [13] in 1960 being illustrated in figure 1.5

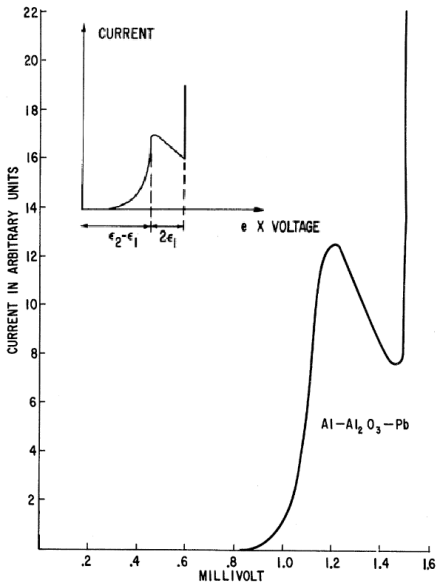

Figure 1.5: Current-voltage curve of the tunneling between two superconductors separated by an insulating layer. ϵ_1 and ϵ_2 are the two correponding gap values. Adapted from Giaever [13]

In the case of a weak electron-phonon coupling, $VN(E_F) \ll 1$ (weak coupling approximation), where V characterises the electron-electron interaction potential and $N(E_F)$ is the density of states at the Fermi level. Tinkham [4] details the calculations leading to the gap value and critical temperature:

$$\Delta(T=0) = 2\,\hbar\,\omega_D\, e^{\frac{1}{V\,N(E_F)}}$$

$$k_B\,T_c = 1.13\,\hbar\,\omega_D\, e^{\frac{1}{V\,N(E_F)}}$$

Looking at the second equation, we can see that we get back to the isotope effect if $VN(E_F)$ is constant for all isotopes of the same element. This is only realised in a few materials, confirmed by the fact that the isotope effect $T_c \approx M^{-\alpha}$ with α close to $\frac{1}{2}$ is only observed in a limited amount of superconductors [14].
The ratio of these two quantities leads to the iconic relationship characterising the gap of BCS superconductors

$$\Delta(T=0) \approx 1.76\,k_B\,T_c$$

BCS theory also describes the coherence length defined earlier as the spatial expansion of Cooper pairs. It is linked to the gap value by

$$\xi_0 = \frac{\hbar\,v_F}{\pi\,\Delta(T=0)}$$

This links the coherence length to microscopic parameters, v_F being the Fermi velocity.

1.1.4 Beyond BCS

The weak-coupling BCS theory is successful in that it provides a microscopic explanation behind a vast number of thermodynamical quantities and specifically ratios independent of the material involved, like $\frac{\Delta}{T_c} = 1.76$ or $\frac{C_s - C_n}{C_s} = 1.43$ characterising the heat capacity jump at T_c [4].
But in the 1960's, experimental deviations from the BCS behaviour were found for some superconductors [15] (e.g. Pb, Zn, Mo...), due to the complexity of the electronic structure and phonon spectrum.
Numerous scientists worked towards a new theory to get around shortcomings of BCS, for example the instantaneous nature of the electron-phonon-electron interaction. As a result, Eliashberg theory [16] takes into account the strength of the electron-phonon coupling λ, and McMillan [17] calculated a new expression of the critical temperature:

$$T_c = \frac{\Theta_D}{1.45} e^{-\frac{1.04\,(1+\lambda)}{\lambda-\mu^*\,(1+0.62\,\lambda)}}$$

where μ^* characterises the Coulomb repulsion taking into account the timescales of the system. It is to be noted that in the limit of small λ, BCS results are recovered from Eliashberg theory.

Because electrons are fermions, the superconducting wavefunction has to be antisymmetric under exchange of particles:

$$\Phi_{\sigma_1\sigma_2}(\boldsymbol{r_1}, \boldsymbol{r_2}) = -\Phi_{\sigma_2\sigma_1}(\boldsymbol{r_2}, \boldsymbol{r_1})$$

In the BCS framework, two electrons with momentum and spin ($\boldsymbol{k}\uparrow, -\boldsymbol{k}\downarrow$) pair in a spin singlet state (antisymmetric) $\chi^{spin}_{\sigma_1\sigma_2} = \frac{|\uparrow\downarrow\rangle - |\downarrow\uparrow\rangle}{\sqrt{2}}$, so the orbital part has to be symmetric. The BCS calculations assume isotropy of the electron-phonon interaction, which dictates the quantum number $L = 0$ (symmetric). This leads to an isotropic gap function

$$\Delta(\boldsymbol{k})\, e^{i\,\theta(\boldsymbol{k})} = \Delta\, e^{i\,\theta}$$

whereby the magnitude of the gap does not depend on $\boldsymbol{k}$ and the Fermi surface the system is fully gapped (s-wave) with a constant phase (figure 1.6).

Unconventional superconductors are materials that do not behave according to BCS theory (i.e. spin-singlet, $L = 0$ and phonon mediated pairing). For example, symmetry of the spatial part of the wavefunction can be realised with other even values of L, and in 1979 Steglich *et al.* [18] discovered the first unconventional singlet d-wave ($L = 2$) in $CeCu_2Si_2$. In this case, the phases of different parts of the Brillouin zone differ by π and the gap value goes to zero along specific directions of the Fermi surface (nodes). A diagram of the situation for a particular situation ($d_{x^2-y^2}$ symmetry) and a circular Fermi surface is shown in figure 1.7.

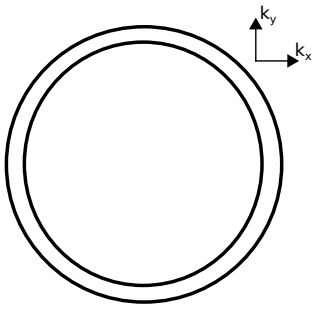

Figure 1.6: Diagram of a fully gapped circular Fermi surface

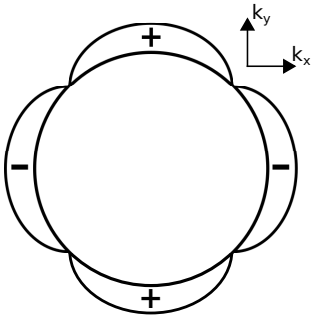

Figure 1.7: Diagram of a gap with $d_{x^2-y^2}$ symmetry and circular Fermi surface, $\Delta(k) = \Delta_0\,(\cos k_x - \cos k_y)$

Many types of unconventional superconductivity exist [19], some materials displaying gaps on different Fermi sheets or even anisotropic gaps. The most impactful discovery took place in 1986, when Bednorz and Müller [20] discovered superconductivity in the cuprate ('copper oxide') LaBaCuO with $T_c = 35\,K$, a critical temperature ∼12 K above the highest T_c found 13 years prior in Nb_3Ge [21], but more importantly above what was thought to be the upper theoretical limit of $\sim 30\,K$ for superconductors with strong electron-phonon coupling. This discovery sparked an intense research effort in these high-T_c superconductors, chasing the possibility to obtain room temperature superconductivity and its potential immense economic impact.

1.1.5 Effect of impurities and non-locality

Pippard noticed that London theory was not accurately describing all superconductors. In 1953, he measured the variation of the penetration depth in tin [22] and found that it varies significantly with the percentage of impurities. In the London picture, adding impurities to the system (to a certain extent) does not significantly alter the electronic properties, so both n and m, hence λ_L only weakly vary with impurity concentration. Looking back at the London equation in section 1.1, we see that the value of the current density $\boldsymbol{j}$ is evaluated at the same point in space as the vector potential $\boldsymbol{A}$. This is a local theory, it assumes that the electrons of the Cooper pairs feel the same vector potential as the center of mass of the pair.
To explain his observations, Pippard proposed [22] a non-local version of the London equation

$$\boldsymbol{j} = -\frac{3}{4\,\pi\,\mu_0\,\lambda_P^2\,\xi^2}\int \frac{\boldsymbol{r'}(\boldsymbol{r'}.\boldsymbol{A}(\boldsymbol{r}-\boldsymbol{r'}))}{r'^3} e^{-\frac{r'}{\xi}} d^3r'$$

ξ characterises the fact that a variation of the supercurrent density cannot take place over an arbitrary small distance. In order to take into account the effect of the reduction of the mean free path with increasing impurity content, he introduced an intrinsic finite coherence length ξ_0 preventing $\xi \to 0$ for $l \to \infty$

$$\frac{1}{\xi} \approx \frac{1}{\xi_0} + \frac{1}{l}$$

$$\text{and a new penetration depth } \lambda_P = \lambda_L \sqrt{\frac{\xi_0}{\xi}} \approx \lambda_L \sqrt{1 + \frac{\xi_0}{l}}$$

In the limit $\lambda_P \gg \xi$, i.e. for a slow-varying vector potential the non-local relationship yields a modified London equation

$$\boldsymbol{j} = -\frac{\boldsymbol{A}}{\mu_0\,\lambda_P^2}$$

These results explain the behaviour of the experimental data illustrated in figure 1.8: the smaller the mean

free path (more impurities), the larger the penetration depth.

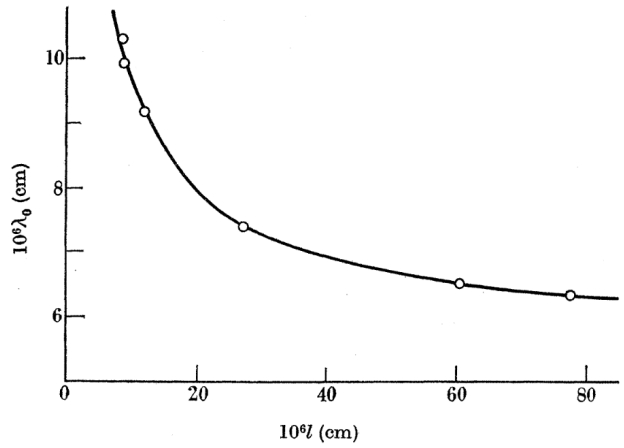

Figure 1.8: Penetration depth versus mean free path in superconducting tin. From Pippard [22]

1.1.6 Different types of superconductivity

In superconductors, the existence of the two lengthscales λ and ξ gives rise to different behaviours. There are two scenarios at play, depending on the values of these parameters.

For $\lambda \ll \xi$, the field inside the sample is quickly screened and the superconductor has to pay the energy cost of diamagnetism. It is energetically unfavourable for the system to form normal/superconducting (N/S) interfaces.

For $\lambda \gg \xi$, the superconducting phase is quickly established within the sample and the magnetic pressure is lessened over λ, i.e. there is condensation energy without the full magnetic cost, the formation of N/S interfaces is promoted.

Ginzburg and Landau showed on the basis of numerical integration (proof by Chapman [23]) that the surface energy σ_{ns} of a N/S interface varies as a function of the so called Ginzburg-Landau parameter $\kappa = \frac{\lambda}{\xi}$ as follows:

$$\begin{cases} \sigma_{ns} > 0 \text{ for } \kappa < \frac{1}{\sqrt{2}} \\ \sigma_{ns} = 0 \text{ for } \kappa = \frac{1}{\sqrt{2}} \\ \sigma_{ns} < 0 \text{ for } \kappa > \frac{1}{\sqrt{2}} \end{cases} \tag{1.1}$$

For $\sigma_{ns} > 0$, the superconductor is of Type I, and the system completely expels the magnetic field up to an applied field H_c and temperature T_c where it is no longer superconducting (figure 1.10). This behaviour is represented in figure 1.9, where the sample magnetisation is opposing the field as $M = -H$ (i.e. $\chi = 1$)

and suddenly drops to zero at H_c.

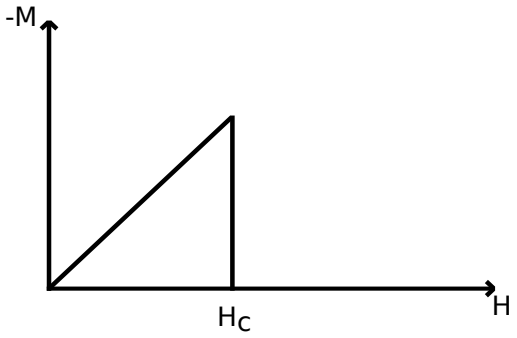

Figure 1.9: Magnetisation versus applied field for a Type I superconductor

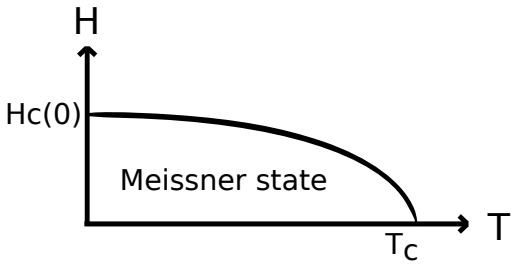

Figure 1.10: Phase diagram of a Type I superconductor

When $\sigma_{ns} < 0$ (Type II superconductivity), the system gives rise to two critical fields (figure 1.12). Up to the first critical field the superconductor behaves like a Type I. Above H_{c1}, in the Mixed state (or Shubnikov phase), increasing the field makes the magnetisation decrease because field enters the sample until superconductivity is destroyed at the second critical field (figure 1.11).
In GL theory, both H_{c1} and H_{c2} are linked to the thermodynamical critical field H_c by the following relationship

$$\frac{H_c}{H_{c1}} \approx \frac{H_{c2}}{H_c} \approx \sqrt{2}\,\kappa$$

We see that the higher κ is, the further apart the first and second critical field are. For the limiting case $\kappa = \frac{1}{\sqrt{2}}$, $H_{c1} \approx H_{c2} \approx H_c$.

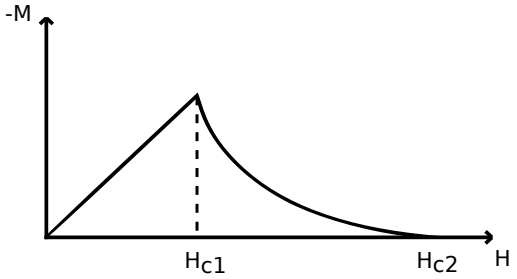

Figure 1.11: Magnetisation versus field for a Type II superconductor

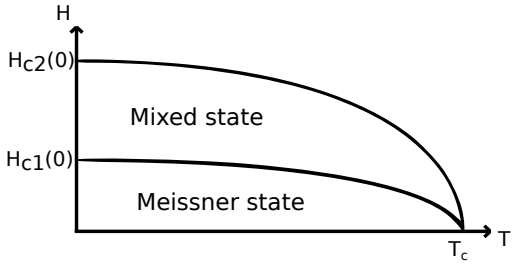

Figure 1.12: Phase diagram of a Type II superconductor

These magnetisation curves only describe an experiment with the field applied along an infinite cylinder-shaped sample, where there is no demagnetising field. In the case of an ellipsoidal shape, the internal field $\boldsymbol{H_{int}}$ is modified by a demagnetising factor N:

$$\boldsymbol{H_{int}} = \boldsymbol{H_{app}} - N\,\boldsymbol{M}$$

In the Meissner state, $\boldsymbol{M} = -\boldsymbol{H_{int}}$ so that

$$\boldsymbol{H_{int}} = \frac{\boldsymbol{H_{app}}}{1-N}$$

We can see that for $N > 0$, the internal field has a larger value than the applied field. This changes the behaviour of the magnetisation curves, as shown in figure 1.13. In samples with non-ellipsoidal shapes, the magnetisation is not homogeneous and alternative numerical approaches are needed (see Chen *et al.* [24]).

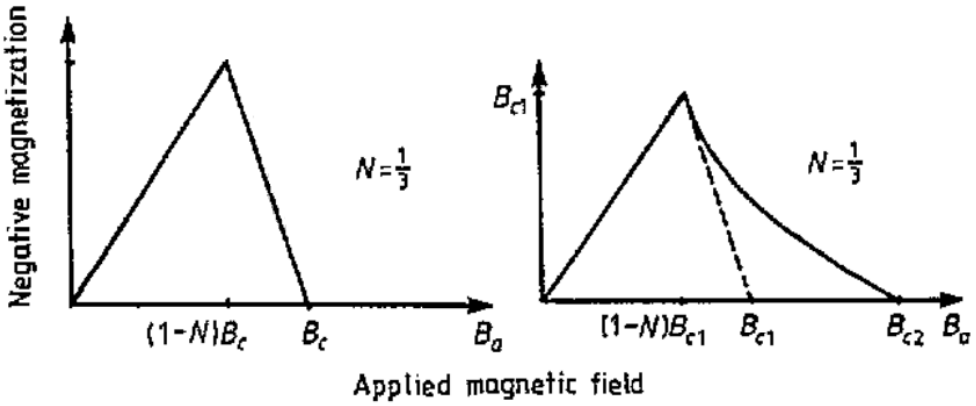

Figure 1.13: Magnetisation versus field of a spherical sample, for a Type I (left) and type II (right) superconductor. Adapted from Brandt [25]

1.2 Vortex lattice and scattering

1.2.1 Vortex lattice

The progressive inclusion of magnetic field inside the sample between H_{c1} and H_{c2} in Type II materials was observed as early as 1936 by Shubnikov *et al.* [26] in B versus H curves of alloys (figure 1.14). However, it was not until 1957 that Abrikosov [27] theoretically described this behaviour using GL theory. This time gap was mainly caused by a lack of understanding of the scientific community of the importance of type II superconductivity, as it considered alloys an 'unsavory business' [28].

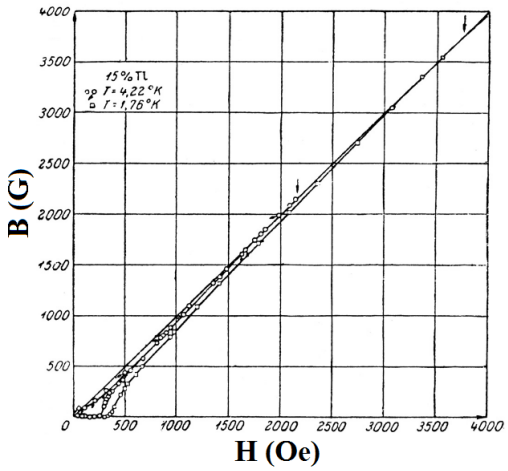

Figure 1.14: Internal field versus applied field for a lead-thallium alloy. From Shubnikov *et al.* [26]

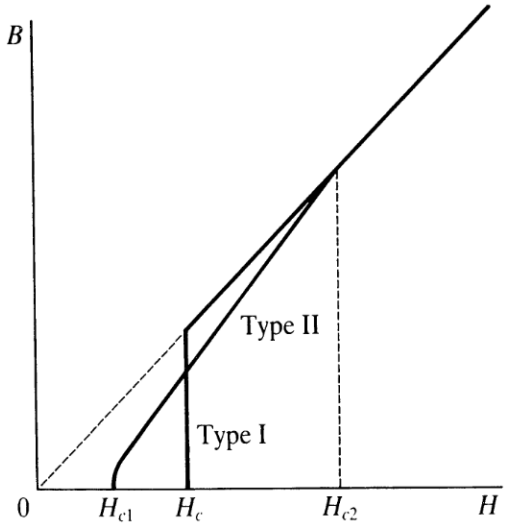

Figure 1.15: Comparison of the internal field versus applied field curve for Type I and II superconductors. From Tinkham [4]

Solving the GL equations with $\kappa > \frac{1}{\sqrt{2}}$, Abrikosov discovered that the magnetic field inside the sample follows a pattern whose periodicity and dimensions are characterised by λ and ξ (figure 1.16). As the applied field increases, it penetrates the sample in the form of magnetic flux lines (also called vortices), which can be seen as cylinders with a core region of radius ξ where the superfluid density reaches zero, with the field gradually screened over a distance λ (figure 1.17).

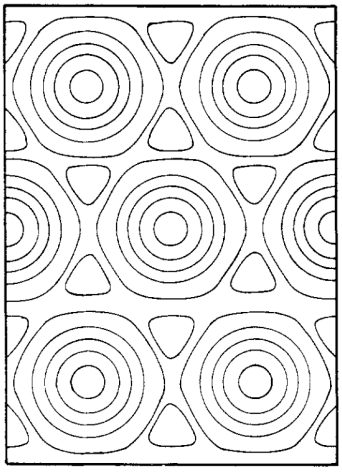

Figure 1.16: Distribution of the magnetic field isolines in a Type II superconductor. From Cyrot [7]

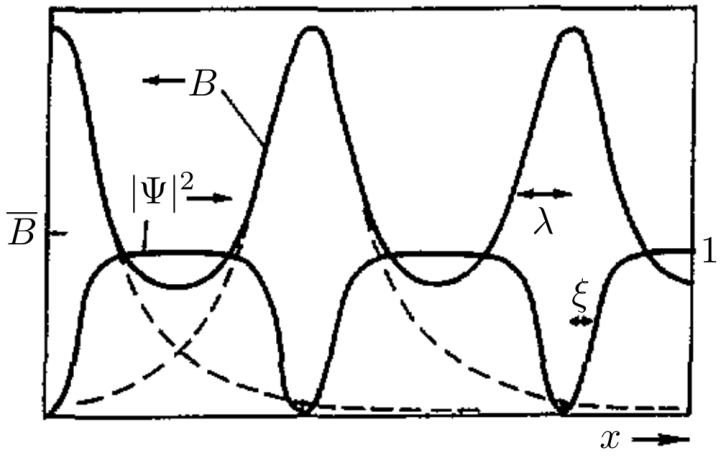

Figure 1.17: One-dimensional diagram of the dimensions of vortices. The dotted lines represent a single vortex. Adapted from Brandt [25]

In Type II superconductors, the overlap of the supercurrents surrounding vortices leads to a repulsive vortex-vortex interaction of the form

$$V \propto (r\,\lambda^3)^{-2}\, e^{-\frac{r}{\lambda}} \qquad \text{for } \lambda \gg \xi \text{ and } r \gg \lambda$$

Abrikosov originally calculated that the arrangement of the flux line lattice (FLL or vortex lattice) having the lowest energy has a square symmetry. Kleiner *et al.* [29] showed subsequently that this was due to a calculation error and that in reality the hexagonal lattice minimises the free energy of the system.
Recalling the expression of the supercurrent density of GL theory in section 1.1 and rearranging gives

$$\boldsymbol{\Delta}\theta = \frac{m}{q\,n\,\hbar}\,\boldsymbol{j} + \frac{q}{\hbar}\boldsymbol{A}$$

The vortex core is normal so the situation is analogous to a multiply-connected superconductor. In this case, in order for the superconducting wavefunction to be single-valued, the integral of the phase around a closed path around the hole/core has to be a multiple of 2π. Integrating along a path at a distance longer than λ to avoid any supercurrents:

$$\frac{q}{\hbar}\int_C \boldsymbol{A}.dl = 2\,\pi\,N \qquad N \text{ integer}$$

$$\text{Using Stoke's theorem } \int_C \boldsymbol{A}.dl = \iint_S \boldsymbol{B}.dS = \Phi_B$$

With Φ_B being the magnetic flux contained in the hole/core. The previous equations lead to Φ_B being a multiple of $\frac{h}{q}$. While London proposed a quantised flux with $q = e$, Schafroth [30] (1950) reckognised that the bosonic behaviour of the pairs should lead to $q = 2\,e$. The first experimental test of this theory was observed in 1961 by Deaver and Fairbank [31] by measuring the quantisation of the trapped magnetic flux inside hollow tin cylinders (figure 1.18). This is the confirmation of Cooper pairing, which means that the previous notations used in section 1.1 correspond to $q = 2\,e$ and $m = m_e$.

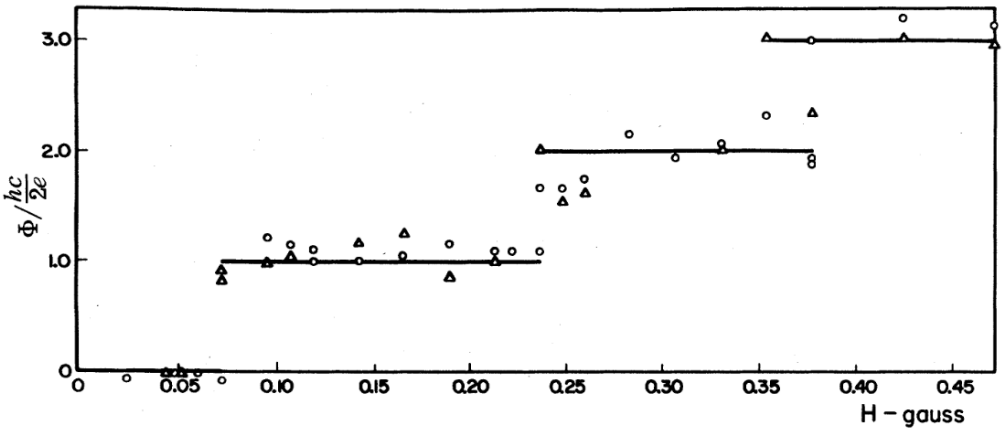

Figure 1.18: Observation of the quantisation of the trapped flux in a hollow superconducting tin cylinder. From Deaver and Fairbank [31].

We see that the magnetic field inside a vortex can be a multiple of the quantum flux $\Phi_0 = \frac{h}{2\,e} \approx 2.07\,10^{-15}\,T.m^2$. While it is possible to get multiquantum vortices by engineering columnar defects [32] or even fractional vortices in more exotic systems [33], in a bulk superconductor of the second kind the formation of $N > 1$ vortices in energetically unfavourable [34].

Tinkham [4] derives two useful relationships from the vortex lattice, linking microscopic quantities to macroscopic ones:

$$H_{c1} = \frac{\Phi_0}{4\,\pi\,\mu_0\,\lambda^2}(ln\,\kappa\,+\,0.5)$$

$$H_{c2} = \frac{\Phi_0}{2\,\pi\,\xi^2}$$

1.2.2 Scattering theory

The flux line lattice is a periodic arrangement of vortices and as such it can be described in terms of reciprocal space. Every point in a 3D Bravais lattice can be described as a combination of its primitive

vectors $(\boldsymbol{a_1}, \boldsymbol{a_2}, \boldsymbol{a_3})$ forming the direct lattice vector

$$\boldsymbol{R} = u\,\boldsymbol{a_1} + v\,\boldsymbol{a_2} + w\,\boldsymbol{a_3}$$

An alternative represention of the lattice can be performed in Fourier or reciprocal space, with a corresponding basis: $(\boldsymbol{b_1}, \boldsymbol{b_2}, \boldsymbol{b_3})$ constructed as

$$\boldsymbol{b_1} = 2\pi\,\frac{\boldsymbol{a_2} \times \boldsymbol{a_3}}{A}$$

$$\boldsymbol{b_2} = 2\pi\,\frac{\boldsymbol{a_3} \times \boldsymbol{a_1}}{A}$$

$$\boldsymbol{b_3} = 2\pi\,\frac{\boldsymbol{a_1} \times \boldsymbol{a_2}}{A}$$

with $A = \boldsymbol{a_1}.(\boldsymbol{a_2} \times \boldsymbol{a_3})$ being the triple product or the area of the real space unit cell. In turn, every point of the reciprocal lattice is described as a reciprocal lattice vector

$$\boldsymbol{G} = h\,\boldsymbol{b_1} + k\,\boldsymbol{b_2} + l\,\boldsymbol{b_3} \quad \text{h, k, l integers}$$

Every such vector is perpendicular to a series of planes in real space, characterised by Miller indices (h, k, l) and their order n such as $\boldsymbol{G} = n\,\boldsymbol{G_0}$ (n integer). The distance (in real space) between those equidistant parallel planes is noted

$$d = \frac{2\pi}{|\boldsymbol{G}|}$$

In 1912, Laue established the equations [35] governing the diffraction of a wave by a crystal lattice. An incident wave with a scattering vector $\Delta\boldsymbol{k} = \boldsymbol{k_f} - \boldsymbol{k_i}$ has to obey the following relationships:

$$\boldsymbol{a_1}.\Delta\boldsymbol{k} = 2\pi\,h$$

$$\boldsymbol{a_2}.\Delta\boldsymbol{k} = 2\pi\,k$$

$$\boldsymbol{a_3}.\Delta\boldsymbol{k} = 2\pi\,l$$

This means that the scattering vector must be oriented along a specific direction of the crystal lattice.
In order for scattering to occur, the Laue condition $\Delta\boldsymbol{k} = \boldsymbol{G}$ has to be fulfilled. In the case of elastic scattering, this means that the reciprocal lattice points have to lie on a sphere of radius $k = |\boldsymbol{k_f}| = |\boldsymbol{k_i}|$.

This yields (see figure 1.20):

$$2\,d\,sin\,\theta = n\,\lambda$$

This corresponds to Bragg's law, proposed by W.L. Bragg [36] in 1913 to explain the intensity of the diffraction pattern of scattered X-rays in solids.

The physical origin of this phenomenon is due to the constructive interference of Rayleigh scattered waves by a crystal. For clarity, the situation in both real and reciprocal space can be seen in figures 1.19 and 1.20.

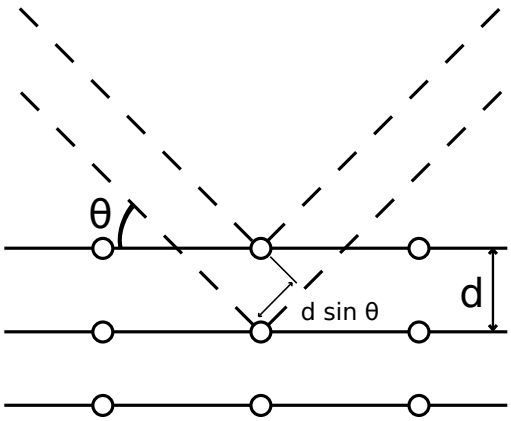

Figure 1.19: Real space representation of Bragg's law

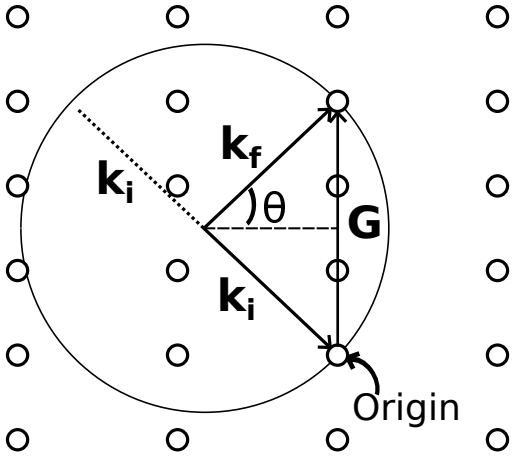

Figure 1.20: Reciprocal space view of Bragg's law, with the Ewald's sphere of radius $k = \frac{2\pi}{\lambda}$

A scattering event is the interaction of a wave with a potential $V(r)$, described by the Lippmann-Schwinger equation. This equation can be expressed using Born series (expansion in powers of V) and a common approximation is the (first order) Born approximation and is valid for the majority of experimental situations (a notable exception is grazing-incidence scattering) and can be interpreted in several ways:

- each scatterer is excited only by the incident wave (instead of the sum the outgoing and incoming wave)
- single scattering: the waves are only scattered by one scattering centre (absence of multiple scattering).
- the potential is weak enough that the scattered wave only slightly differs from the incident plane wave.

In simpler terms, the effect of scattering turns a plane wave $\Phi = e^{i\boldsymbol{k}.\boldsymbol{r}}$ into a spherical wave:

$$\Phi'(r) = f(\boldsymbol{k}, \boldsymbol{k'})\,\frac{e^{i\boldsymbol{k'}.\boldsymbol{r}}}{r} \qquad (r \to \infty)$$

$$\text{where } f(\boldsymbol{k}, \boldsymbol{k'}) = -\frac{m_n}{2\pi\hbar^2}\left|\int V(\boldsymbol{r})\,e^{i\boldsymbol{\Delta k}.\boldsymbol{r}}\,d\boldsymbol{r}\right|^2$$

$f(\boldsymbol{k}, \boldsymbol{k'})$ is the scattering amplitude. The scattering event causes a phase-shift δ between the scattered wave and the incoming wave.

In order to understand the physical meaning of $f(\boldsymbol{k}, \boldsymbol{k'})$, we note that for small δ, the Born approximation is equivalent to a plane wave expansion of $f(\boldsymbol{k}, \boldsymbol{k'})$ (i.e. a sum of spherical waves).

Scattering off a hard sphere potential ($V = \infty$ for $r < b$, else 0) and taking only the zeroth order term $l = 0$ (s-wave or spherical potential) yields:

$$f \approx \frac{\delta_s}{k} \approx -b \qquad \text{where } k = \frac{2\pi}{\lambda}$$

We can see that f has the unit of a length. In this low energy approximation, the scattering amplitude $f(\boldsymbol{k}, \boldsymbol{k'})$ is called the scattering length and characterises the dimension of the scatterer i.e. the radius b of the sphere.

The probability that a scattering event takes place is described by its total cross-section σ in units of m^2

$$[\sigma] = (\#\text{ of incident neutrons})\ \text{second}^{-1}[\phi_n]^{-1}$$

$$\text{and the neutron flux } [\phi_n] = (\text{total count of incident neutrons})\ \text{cm}^{-2}\ \text{second}^{-1}$$

In the classical realm, the cross-section σ represents the probability of collision of a particle beam with a disk of area $\sigma = \pi\, b^2$.

In the quantum world, is often expressed as a differential cross section $\frac{d\sigma}{d\Omega}$ which quantifies this probability for a given solid angle $d\Omega$, which is linked to the scattering length by:

$$\frac{d\sigma}{d\Omega} = |f(\boldsymbol{k}, \boldsymbol{k'})|^2 \underset{kb \ll 1, l=0}{=} b^2 \quad \therefore \quad \sigma = 4\pi\, b^2 = \pi(2b)^2$$

Taking a step up in complexity by considering an ensemble of scatterers, the scattering length can be described as a complex number and the total cross-section can be separated in three components:

$$\sigma_{tot} = \sigma_{coherent} + \sigma_{incoherent} + \sigma_{absorption}$$

The coherent cross section depends on $\boldsymbol{k}$ and is proportional to the mean value of the scattering length $< b >$.

The incoherent component does not contain any structural information and is a function of $\text{var}(b) =< b^2 > - < b >^2$.

The imaginary part of the scattering length represents the absorption cross-section.

1.2.3 Neutron diffraction and vortex lattice

In reality, the steps outlined above to help us understand the meaning of $f(\boldsymbol{k}, \boldsymbol{k'})$ are too simplistic to describe the system.

Taking a crystallographic point of view, the diffracted signal can be described as a convolution of a contribution originating from the crystal basis $F(\boldsymbol{r})$ (the form factor) and the part arising from its distribution in the unit cell, the structure factor $S(\boldsymbol{r})$.

Neutrons are spin-1/2 particles of mass m_n composed of three quarks which are at the origin of the neutron magnetic moment μ_n. The potential felt by neutrons is linked to the internal magnetic field of the sample:

$$V(\boldsymbol{r}) = -\boldsymbol{\mu_n}.\boldsymbol{B}(\boldsymbol{r})$$

This means that the system is not composed of point-scatters, but that the (continuous) spatial distribution of the field is going to determine the cross-section.

As a consequence of the fact that $f(\boldsymbol{k}, \boldsymbol{k'})$ is the Fourier transform of the potential, we have:

$$\frac{d\sigma}{d\Omega} = |F(q)|^2 \, S(q)$$

In 1954, Van Hove [37] expressed the potential/field distribution created by scatterers as a pair correlation function. In real space, it is described by its correlation length which characterises its decay: the distance over which the signal becomes dissimilar to its value at the origin. Applying this to the FLL in reciprocal space, this results in diffraction spots having characteristic dimensions corresponding to the reciprocal space correlation lengths.

Therefore, in order to calculate the intensity of the signal, we have to integrate over all reciprocal space. For a given *(h,k)* spot in the reciprocal lattice, the calculation (detailed by Egetenmeyer [38]) leads to:

$$I(\boldsymbol{q_{h,k}}) = 2\pi V \phi_n (\frac{\gamma}{4})^2 \frac{\lambda_n^2}{\Phi_0^2 \, \boldsymbol{q_{h,k}} cos(\zeta)} \, |F(\boldsymbol{q_{h,k}})|^2$$

where V is the volume of the sample, γ the neutron moment, $\lambda_n = \frac{h}{m_n \, v}$ the de Broglie wavelength of the neutrons. To understand the meaning of the parameter ζ, we have to describe a FLL neutron scattering experiment.

The inter-vortex distance d is large (typically of the order of 100 nm), so Bragg's law place a constraint on the values of θ and λ_n. However, the neutron wavelength cannot be experimentally arbitrarily high as the flux (for a reactor source like ILL) varies as:

$$\phi_n \propto v^3 \, e^{-\frac{1}{2} m \, v^2 / k_B \, T} \mathrm{d}v \propto \frac{1}{\lambda_n^4}$$

where T is the temperature of the moderator. For thermal neutrons (T$\sim$ 290 K), the peak flux is typically at $v \sim 2.2$ km s^{-1} ($\lambda_n \approx 1.8$ Å or $E \approx 25.3\, meV$). Bragg's law then dictates that in order to see a reflection, the scattering angle must be small. This is achieved by working with a large sample-detector distance, with an experimental setup schematised in figure 1.21. Monochromating the neutron beam to an arbitrarily low limit is unfeasible as it restricts the flux of neutrons. The beam goes through a velocity selector, a rotating turbine which selects a range of wavelength (typically $\Delta\lambda \approx 0.1\,\lambda$); this causes the Ewald's sphere to acquire a width. Neutrons are scattered in the directions where the sphere is in contact with reciprocal lattice spots. As seen in figure 1.22 and 1.23, a way to reach all reciprocal space is to tilt the vortex lattice (i.e. the crystal and magnet at the same time) to allow the sphere to cut through the whole reciprocal space. The Lorentz angle ζ appears here to correct for the overestimated q-value of a spot that does not lie directly on the direction perpendicular to the axis of rotation.

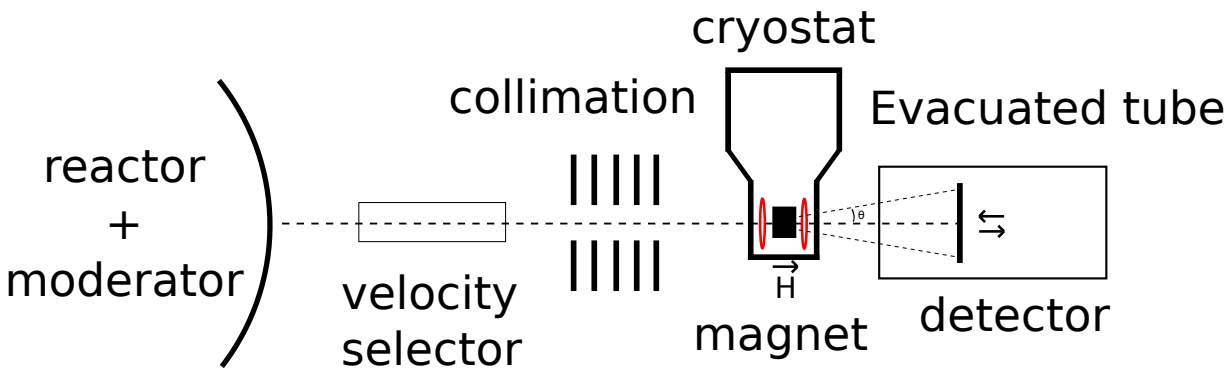

Figure 1.21: Diagram of the principal components of a small-angle neutron scattering beamline

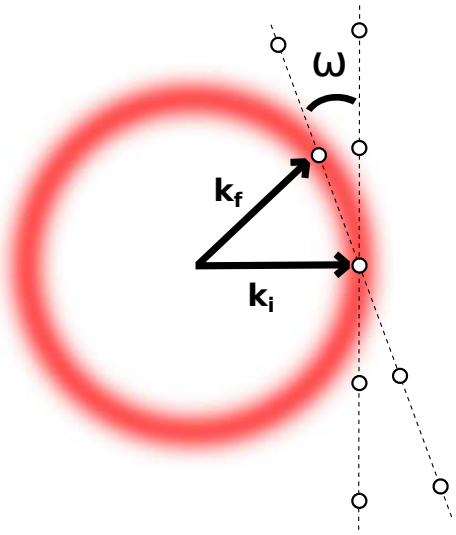

Figure 1.22: Top view representing a 'rock', i.e. changing the sample orientation for the Ewald's sphere to explore the reciprocal lattice.

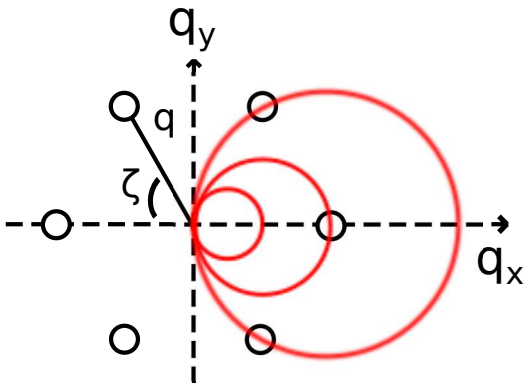

Figure 1.23: Vertical slice of the reciprocal space for different rocking angles.

The possibility of observing the flux line lattice was first suggested by de Gennes and Matricon [39] and seen in 1964 using neutron scattering by Cribier *et al.* [40]. The Bragg peaks due to neutron scattering off the vortex lattice lie on top of a $I \propto q^{-4}$ background described by Porod's law, as seen in figure 1.24

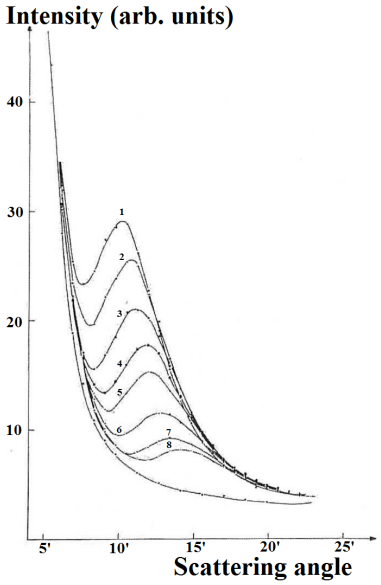

Figure 1.24: Bragg peaks of the FLL in niobium at 4.2 K, where the labels 1 to 8 represent increasing fields. From Cribier *et al.* [41]

We see that the Bragg peaks angle increases with increasing field. The first Brillouin zone (i.e. the area enclosing one vortex) encapsulates a flux quantum, which translates into the following formula for a

hexagonal lattice:

$$\frac{4\pi^2}{q^2 \sin(\frac{\pi}{3})} = \frac{\Phi_0}{B_{int}}$$

and Bragg's law: $q = \dfrac{4\pi\, sin(\theta)}{\lambda_n}$

For small angles, this leads to: q , $\theta \propto \sqrt{B_{int}}$

As the field increases, the vortices are packed closer together, which is reflected in the q-value. Using London theory, an ensemble of vortices can be modelled as:

$$\lambda_L^2 \nabla^2 \boldsymbol{B} - \boldsymbol{B} = \Phi_0 \sum_i \delta^{(2)}(\boldsymbol{r} - \boldsymbol{r_i})\boldsymbol{z}$$

The magnetic field can be expressed as a Fourier series $B(\boldsymbol{r}) = \sum_{\boldsymbol{G}} \boldsymbol{B_G}\, e^{i\boldsymbol{G}.\boldsymbol{r}}$. Replacing this in the previous equation yields the form factor:

$$B_G = \frac{< B >}{1 + \lambda_L^2 \, |\boldsymbol{G}|^2}$$

1.3 Cryostat and dilution refrigeration

In order to get a well-established superconducting state, a general rule of thumb is to reach temperatures below $\frac{T_c}{3}$. This can be often achieved by cooling with liquid ^{4}He, whose boiling point sits at 4.2 K. It is possible to go to lower temperatures by pumping the liquid-gas interface thus lowering the vapor pressure (evaporative cooling), theoretically reaching temperatures down to 1 K.

In practice, the cryostat and sample have to be shielded from thermal perturbations like heat transfer by conduction (e.g. instrumentation wires, poor vacuum) and black-body radiations. In order to mitigate these effects, the design of vacuum and thermal shields (e.g. 77 K and 4 K) is commonly used to minimise heat transfer between different sections of the cryostat. As temperatures decrease, the ability of the system to cool decreases and by definition reaches zero at base temperature. A typical value of the cooling capacity, measured in Watts, is of the order of one milliwatt at 2 Kelvin.

To counterbalance the heat load induced by the imperfect thermal shielding, which is more problematic as temperature decreases, the cooling capacity has to be increased to match the demands of the experiment (what base temperature? How large is the sample?...). The size of the liquid-gas interface or the pumping power can be increased to provide more cooling, or even changing the cryogenic liquid to ^{3}He, reaching temperatures of 200 mK.

In various situations, this is not enough. The scientific community widely relies on the use of dilution refrigerators to reach temperatures down to milikelvins. Their basic principle, first proposed by London in 1951 [42], relies on the fact that a mixture of ^{3}He and ^{4}He separates in two phases (below $T \approx 870$ mK), a dilute phase (^{3}He-rich) and concentrated phase (^{4}He-rich). Because ^{3}He atoms are lighter, the concentrated phase forms an arrangement of ^{3}He atoms surrounded by the heavier ^{4}He atoms. This situation is equivalent to the 'liquid-gas' system described earlier. The vapor pressure of ^{3}He is the highest, so pumping on the dilute phase will destroy the equilibrium between the two phases, which is restored by ^{3}He migration from the 'ordered' concentrated phase to the gas-like dilute phase. This evaporation creates an energy deficit at the interface.

The key point that makes dilution refrigeration possible is that there is a lower bound of $\sim 6.6\%$ for the concentration of ^{3}He in the concentrated phase, resulting in a non-zero cooling power as $T \to 0$ (see figure 1.25). Reinjecting the pumped ^{3}He makes continuous cooling possible: a simple diagram of the situation is presented in figure 1.26.

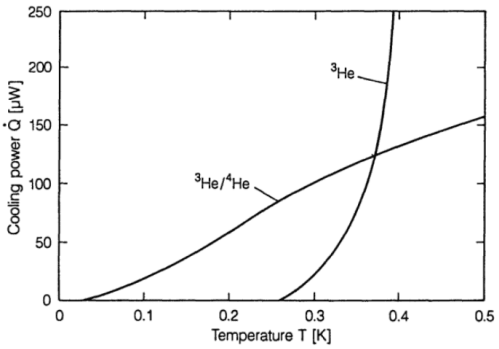

Figure 1.25: Cooling power of ^{3}He and a ^{3}He-^{4}He mixture versus temperature. From Pobell [43]

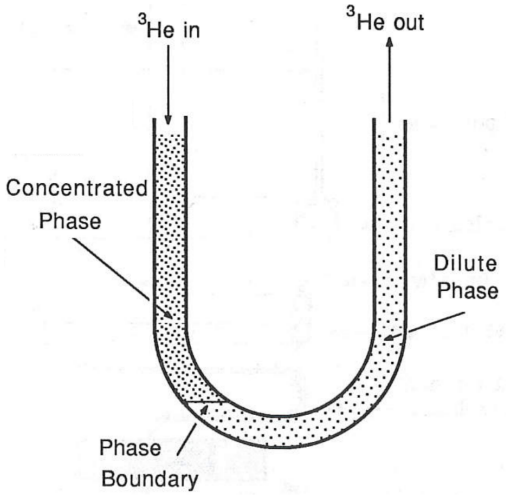

Figure 1.26: Simplified diagram of the dilution refrigeration principle, from Smith *et al.* [44]

CHAPTER 2

BiPd

2.1 Non centrosymmetric superconductors

The discovery of superconductivity in the non-centrosymmetric compound $CePt_3Si$ (Bauer *et al.*, 2004 [45]) triggered a broad interest in non-centrosymmetric superconductors (NCS). This class of materials does not possess a unit cell with inversion symmetry, which is the property to have for every lattice point (*x,y,z*) an indistinguishable *(-x,-y,-z)* point. Rashba first described this lack of inversion symmetry in semiconductors [46] in 1959. It causes an asymmetric crystal field ∇V yielding a spin-orbit interaction $(\boldsymbol{k} \times \nabla V) \cdot \boldsymbol{\sigma}$, acting on electrons with spin $\boldsymbol{\sigma}$ and momentum $\boldsymbol{k}$, affecting the electronic structure of non-centrosymmetric materials. It can for instance give rise to a topological phase, involving Majorana fermions, potentially useful for applications in quantum computing and spintronics due to a long coherence time [47]. Parallels with the physics of the superfluid phase of ^{3}He also have been made [48].

In NCS, antisymmetric spin-orbit coupling (ASOC or Rashba-type coupling) is akin to a Zeeman effect in a magnetic field, as it breaks the spin degeneracy of the band energy $E_{\boldsymbol{k}}$. The Fermi surface is split into two sheets with different spin states (*spin helicities*) [49] and energies $E_{\boldsymbol{k},\pm}$,

$$E_{\boldsymbol{k},\pm} = E_{\boldsymbol{k}} \pm \alpha|\boldsymbol{g}_{\boldsymbol{k}}|$$

where $\alpha|\boldsymbol{g}_{\boldsymbol{k}}|$ characterises the k-dependent contribution of the spin-orbit coupling. The Fermi sheets touch when $\boldsymbol{g}_{\boldsymbol{k}} = 0$. In these materials, instead of the common odd-parity / spin-triplet, even-parity / spin-singlet paradigm (see section 1.1) found respectively in e.g Sr_2RuO_4 and BCS-type superconductors, the ASOC gives rise to a mixture of spin-singlet and spin-triplet pairing channels.

This channel mixture gives rises to a variety of effects: e.g. for a single-band superconductor, this can lead

to a two-component gap function $\Delta_\pm$ of the following form [49]:

$$\Delta_\pm = \Delta_s \pm \Delta_t \, |\boldsymbol{g_k}|$$

Δ_s being the spin-singlet order parameter (OP) and Δ_t the spin-triplet OP. This (hypothetical) simple system now has two different gaps, whose experimental signatures can be detected in many ways (e.g. tunnel diode oscillations [50], heat capacity [51], muon spin relaxation [52]). Complexity arises when the electronic structure consists of a large number of Fermi sheets, but also with the magnitude of the spin triplet component relative to the spin-singlet, creating possible nodes in the gap [53]. Lastly, in addition to inversion symmetry breaking, some NCS show time-reversal symmetry breaking depending on the underlying crystalline symmetry of the material [54]. Evidence of this behaviour can be found by detecting small spontaneous internal fields using muon spin relaxation [55].

2.2 Motivation

The effect of ASOC on the superconducting pairing state is still controversial. On one hand, multiple NCS have been shown to exhibit BCS-type superconductivity, due to a small spin-orbit scattering ($Y_2C_{3-\delta}$, Mg_2Al_3, $BaPtSi_3$...). On the other hand, many NCS are heavy-fermion superconductors ($CePt_3Si$, UIr, $CeRhSi_3$...) and the study of the ASOC in these materials is complicated by strong electronic correlations and the presence of magnetic phases.

In this regard, BiPd is interesting as it does not have heavy-fermion features but is a good candidate for large spin-orbit scattering from the heavy bismuth atoms (ASOC $\propto$ Z and Z_{Bi}= 81). In addition to that, the large density of states of conduction electrons in BiPd makes it favourable to observe a spin triplet component, in contrast with many NCS with low density at the Fermi level [56].

The BiPd samples we study exhibit a high residual resistivity ratio ($\frac{\rho_{300K}}{\rho_{4K}} \approx 160$) and de Haas van Alphen oscillations were observed, both signs of a very clean sample. A high sample quality is especially important in the search for spin-triplet signatures, because impurity scattering tends to smear the superconducting gap in dirty superconductors (Anderson, 1959 [57]).

Figure 2.1 shows the unit cell of BiPd, containing 16 atoms (4 equivalent + 4 inequivalent site for each atom type). BiPd has a monoclinic structure, close to orthorhombic, with a = 5.6284(4) Å, b = 10.6615(4) Å, c = 5.6752(4) Å, $\alpha = \gamma = 90°$ and $\beta = 101°$.

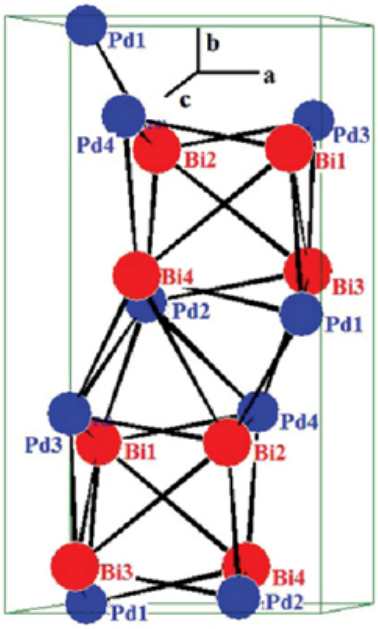

Figure 2.1: Unit cell of BiPd, from Joshi *et al.* [56]

The sample is grown using a modified Bridgman technique, which consists in heating the separated Bi and Pd components in a vacuum sealed quartz tube until they melt. The melted compounds are then cooled in contact with a seed crystal, helping the crystal growth to be in a given crystallographic orientation. This technique, along with a specific heat treatment was used by Joshi *et al.* [56] to grow the samples studied in this thesis.

Joshi *et al.* report $\mu_0 H_{c1}(0) = 123$ G, $\mu_0 H_{c2}(0) = 7000$ G and $T_c = 3.8K$ from heat capacity and resistivity measurements, as pictured on figure 2.2

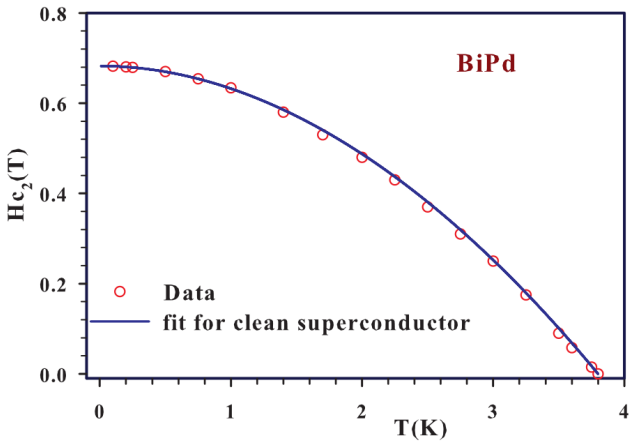

Figure 2.2: Phase diagram of BiPd, from Joshi *et al.*[56]

2.3 Experimental results

2.3.1 Crystal orientation

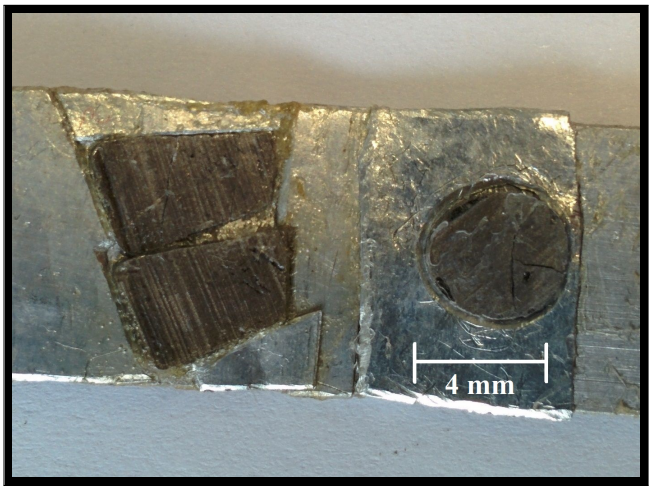

Figure 2.3: Samples surrounded by Cadmium. Notes from the sample growers indicate faces $\perp$ (010) (right) and (100) (left).

The sample growers (Joshi *et al.*) provided us with rectangular and disk-shaped of single crystals, oriented along different directions, as detailed in figure 2.3.

In order to further determine the details of the orientation of these crystals, we performed neutron and X-ray Laue experiments. It turns out to be difficult to distinguish **a*** from **c***, because the sample growers find a ratio $R = \frac{c}{a} = \frac{c^*}{a^*} = 1.008$, leading to the reciprocal space geometry represented in figure 2.4, when looking down the **b** axis. The difference in norm between **a*** and **c*** has been exaggerated for clarity.

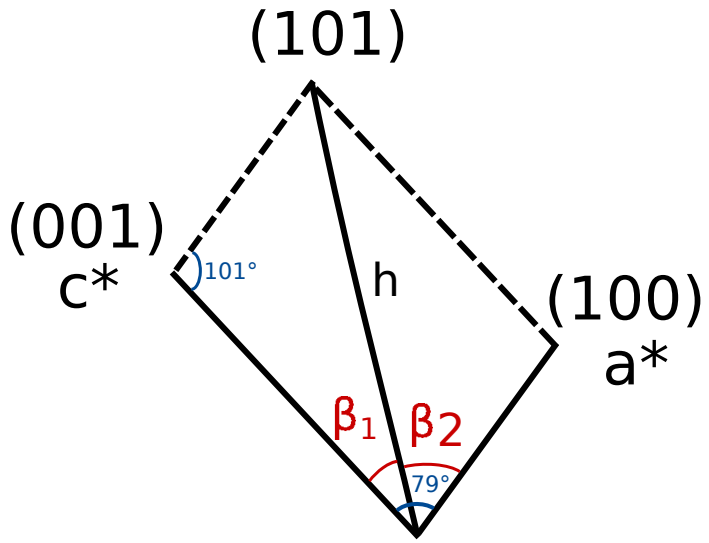

Figure 2.4: Diagram representing the reciprocal space of BiPd, b axis out-of-plane

Using the law of cosines, we calculate the angles β_1 and β_2:

$$h = \sqrt{1 + R^2 - 2\,R\,\cos(101°)}$$

$$\beta_1 = \text{acos}(\frac{1 - R^2 - h^2}{2\,R\,h})$$

$$\Delta\beta = \beta_1 - \beta_2 = 2\,\beta_1 - 79$$

We find that $\Delta\beta \approx -0.38$ degree. Figure 2.5 shows a neutron Laue diffraction pattern taken at ILL in backscattering mode on the Orient Express instrument. The uncertainty on the measure of angles ($\sim$1 degree) due to the the size of the diffraction spots makes it impossible to tell **a*** and **c*** apart.
However we can still identify two directions: $\{101\}$ and $\{10\bar{1}\}$, represented by the white arrows (90° between axes), as well as $\{100\}$ and $\{001\}$ by the red ones (79°).

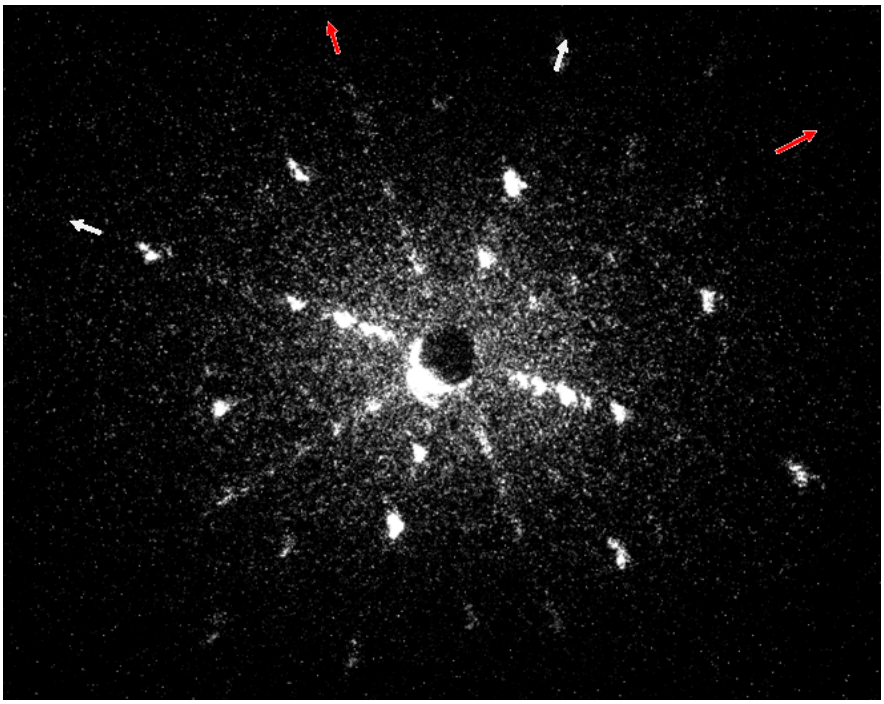

Figure 2.5: Neutron Laue picture of BiPd with the beam along (010)

Determining the orientation of the second type of sample proved to be a more involved endeavour. The sample growers indicated the out-of-plane orientation to be along (100), but taking a diffraction patterns along that axis showed a pattern with weak intensity, seemingly in a random crystal orientation (figure 2.6).

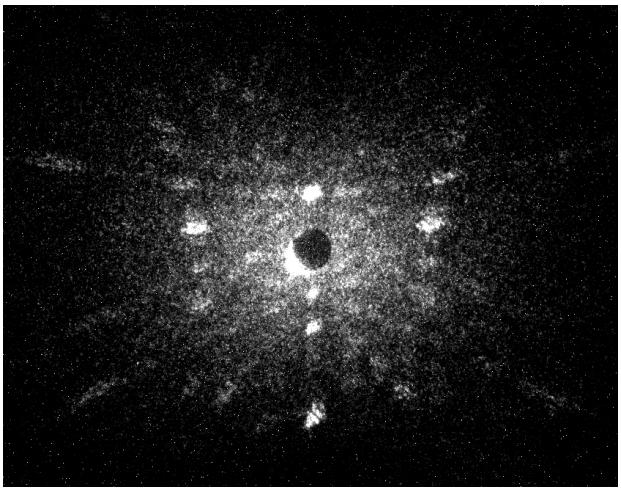

Figure 2.6: "(100)" Laue pattern with phi = 0

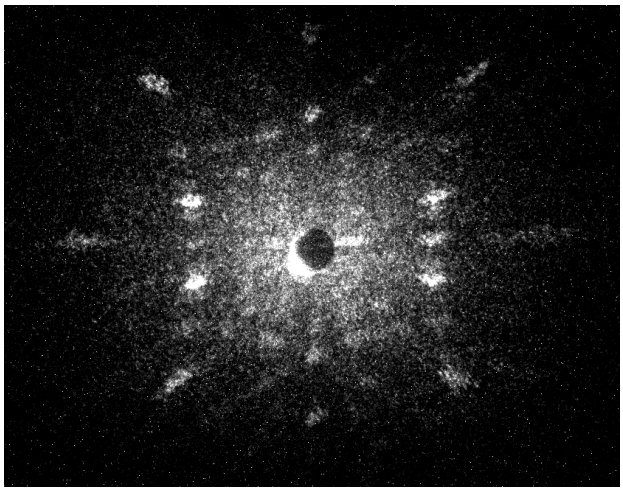

Figure 2.7: "(100)" Laue pattern with phi = 13

It is only when rotating 13 degrees around the horizontal axis 'phi' that a symmetric pattern appears (fig-

ure 2.7), with two mirror planes, suggesting that the original orientation differs from that proposed. Indeed, if the crystal were aligned along **a** (respectively **c**), we should have been able to see both **a*** (respectively **c***) and **b*** directions orthogonal to each other in the diffraction pattern.

As seen in figure 2.8, it seems the axes that display such a symmetric diffraction pattern are {101} and {10$\bar{1}$}.

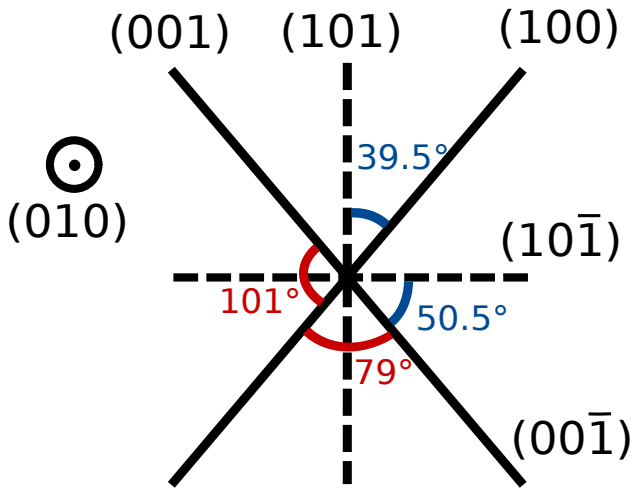

Figure 2.8: Diagram representing the reciprocal space of BiPd, b axis out of the plane. The angle values assume a* = c*.

If the beam is along {101} (respectively {10$\bar{1}$}), the in-plane axes will be **b*** in the vertical direction, and {10$\bar{1}$} (respectively {101}) in the horizontal (orthogonal) direction.

We use the lattice dimensions and Laue equations $\boldsymbol{b^*}.\boldsymbol{b} = 2\pi$ to calculate the angles for various reciprocal lattice spots and compare the values to those measured directly for several equivalent angles on the diffraction pattern.

The first column of table 2.1 is the ratio of the tangents: we divide the tangent of the different spots' angles ('exp. angle' column) by the tangent of one of the the smallest angle found on the diffraction pattern. This provides a guide to see multiplicity relationships between different spots, which is then used to calculate the theoretical values for different beam orientations.

It turns out that the experimental data agrees most with a diffraction taken with the beam along {101} rather than {10$\bar{1}$}. The spots associated with the smallest angles correspond within experimental error (around 1 degree) to (11$\bar{1}$) and equivalent Miller indices.

Several experiments were performed before doing this analysis, as we had no reasons to doubt the sample grower's orientation analysis. In this thesis, we refer to the original (without 13° tilt) direction as "{100}". After this, we switched to the {101} direction for the beam to be along a well-defined crystal axis.

$\frac{\tan(\text{angle})}{\tan(\text{angle}_{\min})}$	**exp. angle**	**angle for beam ∥ {101}**	**angle for beam ∥ {10$\bar{1}$}**
1.00	18.83	18.63	11.56
0.98	18.49	18.63	11.56
0.99	18.65	18.63	11.56
0.97	18.37	18.63	11.56
2.64	42.02	45.33	31.53
3.00	45.66	45.33	31.53
3.01	45.72	45.33	31.53
2.87	44.39	45.33	31.53
8.11	70.12	69.66	58.57
7.89	69.6	69.66	58.57
2.03	34.68	33.99	22.25
2.02	34.55	33.99	22.25

Table 2.1: Comparison between calculated and experimental value of angles along two beam directions. The first column is the experimental ratio of angles, a guide to calculate the theoretical angles in each beam direction

Yelland and coworkers analysed an X-ray Laue diffraction pattern on a different BiPd crystal, grown by a different research group. Their analysis brings to light the possibility that a and c differ by no more than 0.4%, whereas Joshi *et al.* claim a 0.8% difference. This evidence suggests that these lattice parameters are most likely equal.

BiPd can crystallise in two different symmetries summarised in table 2.2. Yelland and coworkers also find a better Laue fit for a $CmC2_1$ crystal symmetry, although close to the reported [56] $P2_1$ symmetry. It is to be noted that the heat treatment is designed to maximise the growth of the α-BiPd phase, supposedly with an unknown amount of β-BiPd phase remaining.

compound name	α-BiPd	β-BiPd
symmetry group	$P2_1$	$CmC2_1$
characteristics	monoclinic	orthorhombic
	$a \neq b \neq c$	$a \neq b \neq c$
	$\alpha = \beta = 90°, \gamma = 101°$	$\alpha = \beta = \gamma = 90°$

Table 2.2: The two crystalline structures of BiPd. The sample undergoes a structural transition from β-BiPd to α-BiPd when the temperature goes below 210°C

As the measurements presented above were done on crystals different from our own and grown in a different laboratory, definitive conclusions cannot be drawn. In particular, the effect of twinning (see section 2.3) adds uncertainty to the situation. In all cases, the possible change of crystal symmetry does not affect the non-centrosymmetry aspect of this study as both $Cmc2_1$ and $P2_1$ lack inversion symmetry.

2.3.2 Preliminary analysis

A variety of scans were performed along the three crystal orientations {010}, "{100}" and {101}, described in the previous section. Figure 2.9a to 2.9c show an overview of the data in field-temperature phase space that were gathered over six SANS experiments at the Institut Laue-Langevin in France (D33) and the Paul Scherrer Institute in Switzerland (SANS-1). For D33, a typical neutron wavelength used was 20 Å with a sample-detector distance $D = 13$ m. When performing experiments on SANS-1, $\lambda_n = 17$ Å and $D = 20.5$ m. All the measurements were obtained by field cooling: that is, the sample is first brought above T_c, a given magnetic field is applied and it only then cooled to the desired temperature. This is done in order to ensure reproducibility, as vortex pinning would play too big an influence in the case of a zero field cool procedure.

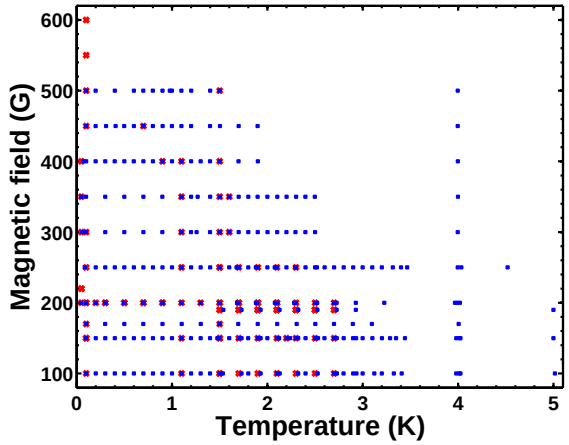

(a) Scans for B ∥ "{010}"

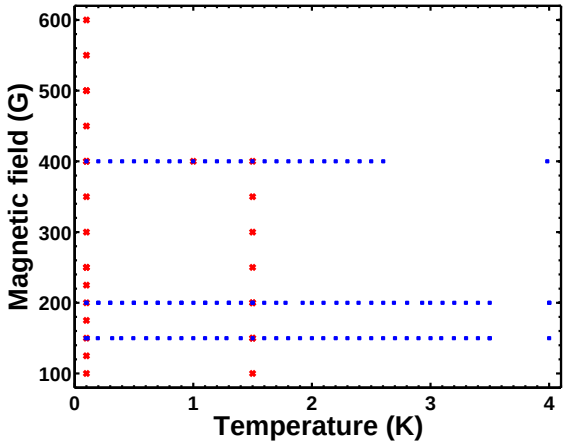

(b) Scans for B ∥ "{100}"

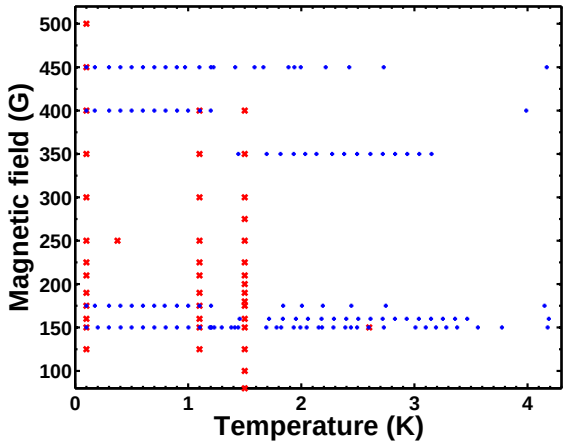

(c) Scans for B ∥ {101}

Figure 2.9: SANS scans performed at different orientations. The red and blue crosses represent field and temperature scans.

A typical diffraction pattern for the beam and field along {010} is shown in figure 2.10, assembled from san and phi scans (sample rotations around the vertical and horizontal axes). We can immediately see a hexagonal symmetry, with two spots having weaker intensities.

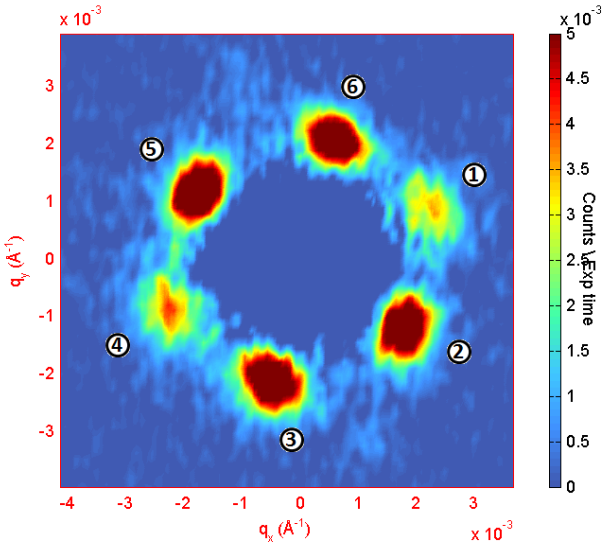

Figure 2.10: Diffraction pattern of the FLL for B ∥ {010} at 200 G and 1.5 K

By overlapping the crystal directions identified with the techniques and limitations detailed previously, we can see in figure 2.11 that the weak spots seem to be aligned along the {103} direction.

In general, the FLL tends to align along directions of high crystal symmetry. Because of the difference between a* and c* (although small) and the lack of inversion symmetry, there is no high symmetry axis in this plane, so we do not expect the flux line to align along a particular axis. It can then be argued that this apparent alignment of the vortex lattice on the underlying crystal is just random.

The same treatment is shown for B ∥ "{100}" in figure 2.12 (a similar FLL is seen for B ∥ {101}). In this case, the inability for the flux line to distinguish between **b*** and **-b*** (the FLL is centrosymmetric) coupled with the fact that there is a 90° angle between b* and $\{10\bar{1}\}$ gives rise to mirror planes on which the vortex lattice aligns.

Looking at the reciprocal lattice vector norm q of each spot (figure 2.13), we can clearly see that the two weak spots have a higher value. We identify two q-values, q_L being the average q of the minority of spots (large q-value) and conversely q_S, the majority with a smaller q-value. A reasonable question to ask is: are the minority spots of the second order, explaining the weak intensity? A simple calculation involving the

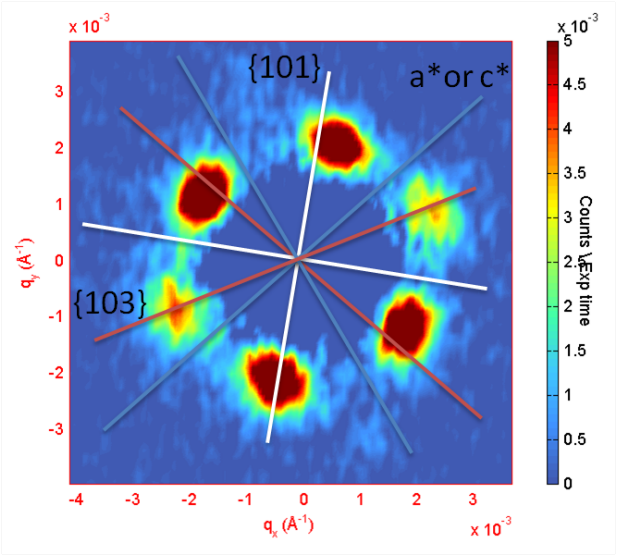

Figure 2.11: Overlap of the crystal lattice directions on the FLL pattern for B ∥ {010} at 200 G and 1.5 K

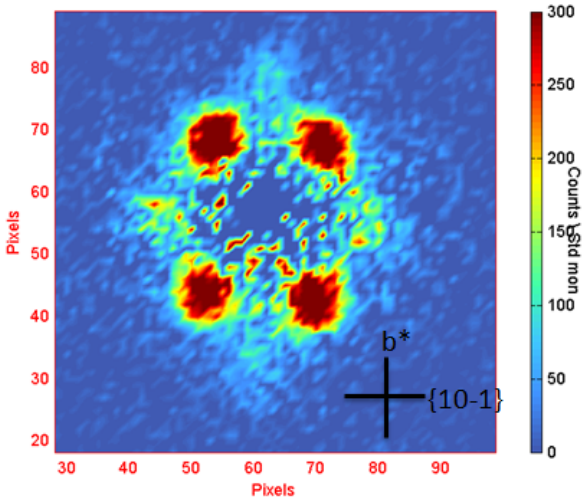

Figure 2.12: Overlap of the crystal lattice directions on the FLL pattern for B ∥ "{100}" at 200 G and 1.5 K

diamond formed by the two adjacent diffraction spots leads to the following value:

$$q_{2^{nd}\text{order}} = 2\, q_S\, \cos(\frac{\text{angle}_{6-2}}{2}) = (2.49 \pm 0.05)\, 10^{-3}\text{Å}$$

This value is slightly larger than the experimental $q_L = (2.39 \pm 0.018)\, 10^{-3}$. We can therefore conclude that these weak spots are of the first order.

The anisotropy is problematic when comparing experimental data with theory: which q-value is suitable to compare with e.g. the q obtained from an isotropic Abrikosov lattice?

The hexagonal vortex lattice is shortened (vertical direction) and lengthened (horizontal) by an amount Γ, and q_Δ is the undistorted q-value. It follows that

$$q_L = q_\Delta\, \Gamma$$

$$q_S = q_\Delta \sqrt{\frac{3}{4\,\Gamma^2} + \frac{\Gamma^2}{4}}$$

From the experimental data we can calculate a q anisotropy ratio q_{ani}. The Γ parameter has the following relationship to this ratio,

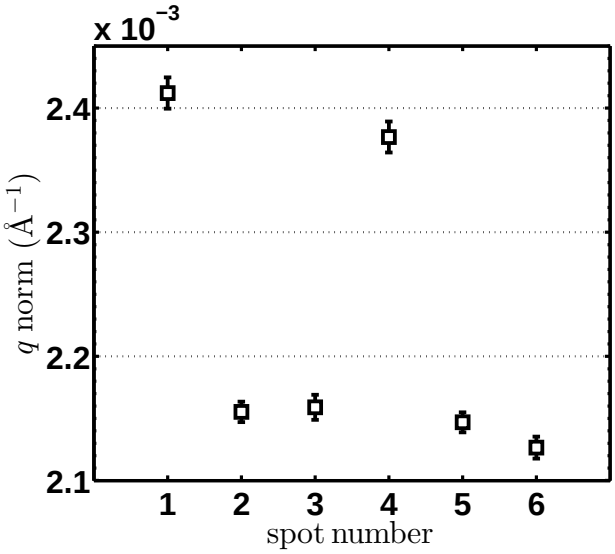

Figure 2.13: Q-values of the diffraction pattern for B ∥ "{100}" at 200 G and 1.5 K

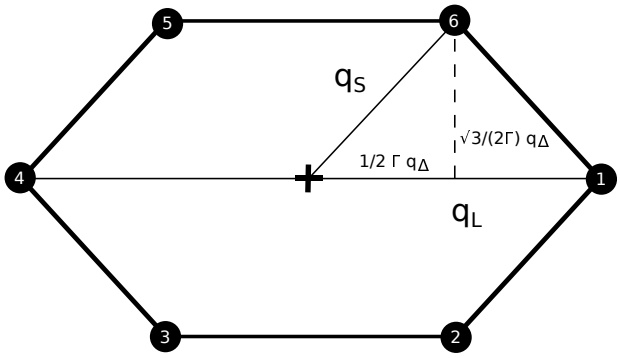

Figure 2.14: Diagram of a distorted hexagon

$$q_{ani} = \frac{q_L}{q_S} = \frac{\Gamma}{\sqrt{\frac{3}{4\,\Gamma^2} + \frac{\Gamma^2}{4}}}$$

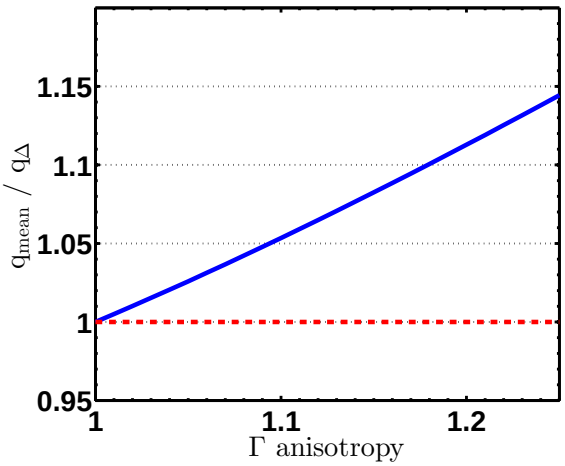

Figure 2.15: $\frac{q_{mean}}{q_\Delta}$ versus FLL anisotropy. The dotted red line shows $q_{mean} = q_\Delta$

Solving q_{ani} for Γ leads to values of q_S and q_L. This can be linked to the experimental quantity q_{mean}, the average of the q-values of all diffraction spots and used to calculate the undistorted q_Δ

$$\frac{q_{mean}}{q_\Delta} = \frac{4\,q_S + 2\,q_L}{6}$$

We see in figure 2.15 the gap between q_Δ and q_{mean} increases with increasing FLL anisotropy. A typical value is $q_{ani} \approx 1.1$, leading to $\Gamma \approx 1.08$. This represents a difference in q of approximately 4%, well above experimental error bars.

To summarise, for each diffraction pattern, we calculate q_{ani}, deduct Γ and finally calculate q_Δ from q_{mean}.

The angle difference between each spots is shown in figure 2.16. The values are centered around 60°, with the smallest angle difference corresponding to the large q spots. From this data and the q-values shown previously we calculate the area of each spots in reciprocal space (see section 1.2), which is linked to the flux quantum by:

$$A_s = \frac{4\pi^2 \, \Phi_0}{B_{int}}$$

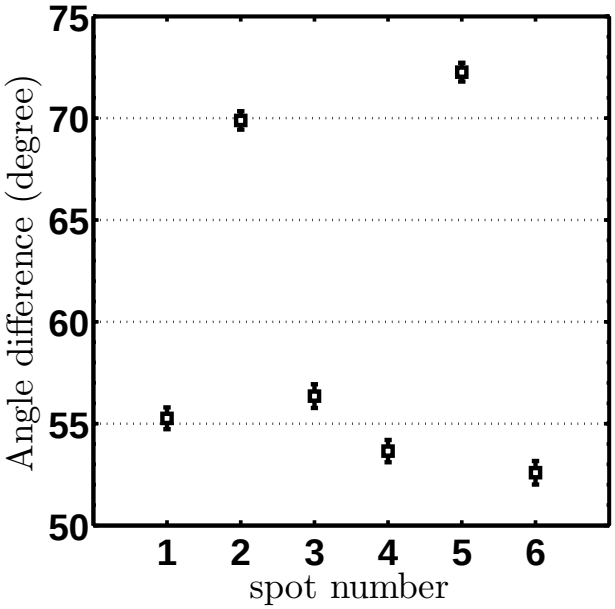

Figure 2.16: Angle difference between adjacent spots for B ∥ (010) at 200 G and 1.5 K

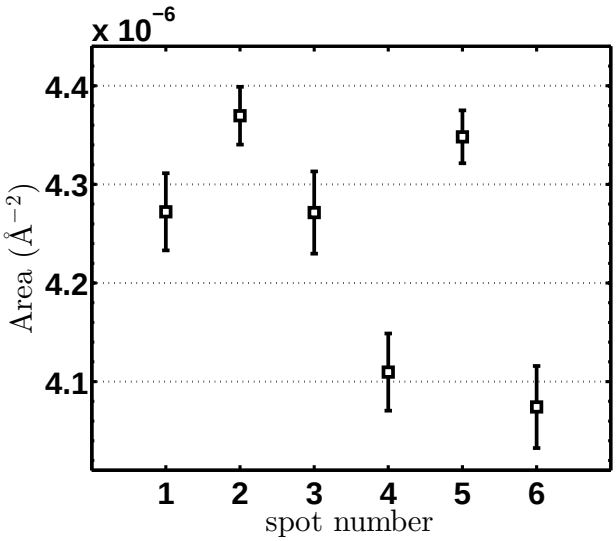

Figure 2.17: A_s corresponding to each spots (see text), B ∥ (010) at 200 G and 1.5 K

Superconductivity dictates that this area has to be the same for each spots, however we find (figure 2.17) that it varies outside of error bars in several cases. This is not the sign of a fundamental deviation from quantum mechanics, but rather it illustrates the fact that even for a good flux line lattice with enough count time and well defined spots, there are always unaccountable systematic errors.

2.3.3 Phase diagram - the superconducting domain

We start by determining the boundaries of the superconducting domain.

Intensity of the signal versus temperature

The various temperature scans performed allow us to identify the point at which the signal on the diffraction pattern disappears. As the temperature increases, so does the penetration depth, until it diverges at T_c. This increase of λ in turn affects the magnetic potential felt by the neutrons inside the sample, which is linked to the scattered intensity (see section 1.2). Measuring the variation of the neutron count of one or several diffraction spots (the intensity) then tells us about the limits of the superconducting phase.

Close to T_c, according to GL theory (see Brandt [25]) the square root of the signal intensity varies linearly with temperature. In principle, this should allow us to clearly pinpoint T_c as showed in figure 2.18.

However, in practice, the uncertainty of the measurements and the lack of smaller temperature steps due to experimental constraints makes it difficult to see that linear behaviour, as illustrated in figure 2.19. In most cases we resort to estimate T_c 'by eye', and report the appropriate (larger) uncertainties accordingly.

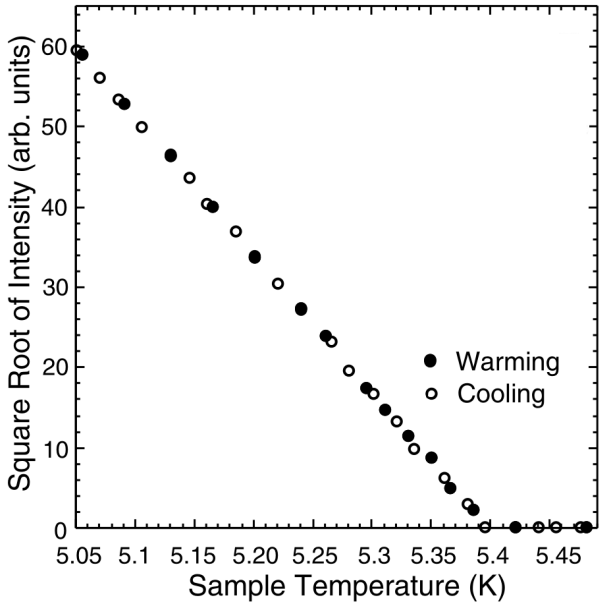

Figure 2.18: $\sqrt{\text{Intensity}}$ versus temperature in niobium. Adapted from Forgan *et al.* [58]

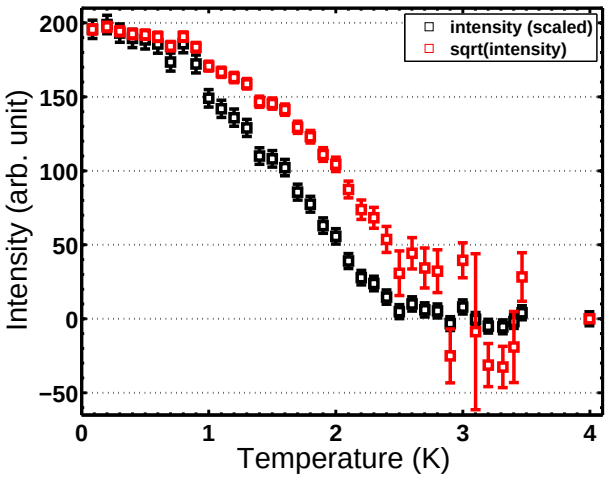

Figure 2.19: Intensity of the signal versus temperature for B ∥ {010} and B = 250 G

Magnetisation measurements

It is difficult to use SANS field scans as a way to probe the limits of the superconducting state. This is due to the fact that in between each field scan, we have to go above T_c and back down or risk having the sample move and the quality of the FLL affected by pinning. In addition to issues of exact reproducibility, this is also a time-intensive process.

Another method to look at the superconducting phase is to measure the magnetisation as a function of field and temperature. To do this, we use a Quantum Design MPMS which reaches a base temperature of 1.8K by ^{4}He pumping. When looking at field scans for a fixed temperature (figure 2.20), we define H_{c2} to be the point where the derivative of the magnetisation is zero. Because of the experimental fluctuations of the data, this point is difficult to accurately estimate: we could either select point 1, where it is approximately zero, or point 2 where the magnetisation actually reaches zero. An *a posteriori* verification of the data tells us the first method yields sensible results.

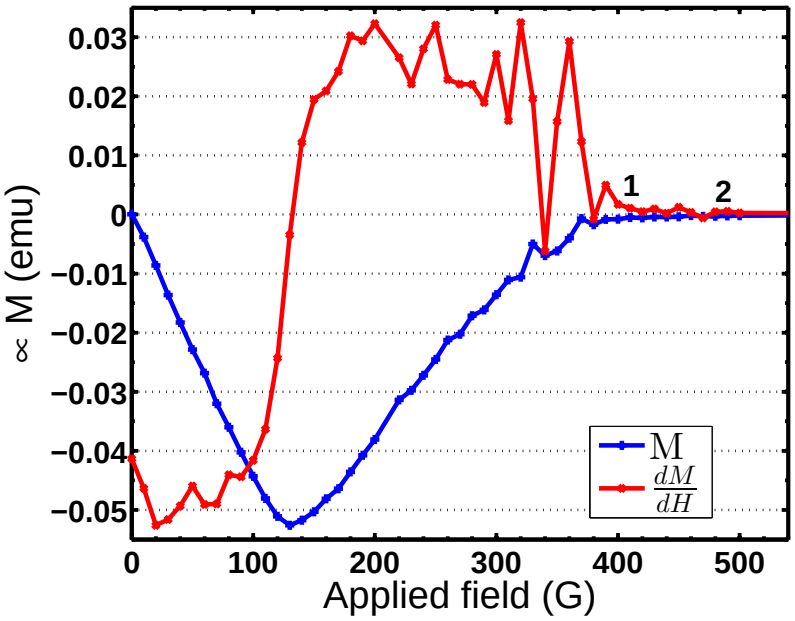

Figure 2.20: .
[mass]) versus applied magnetic field for B ∥ {010} at 1.8 K]Magnetisation versus applied magnetic field for B ∥ {010} at 1.8 K. The derivative is normalised to be on the same scale. The meaning of points 1 and 2 is discussed in the text.

We can offer an rough explanation: for high-κ superconductors, we expect a long thin tail of the magnetisation for fields $H_{c1} \ll H < H_{c2}$. In this case, it is delicate to pinpoint H_{c2} because the errors associated with the measurement may drown this tail in the background noise. However, with a low-κ material, this

problem, although still present, does not lead to such a large error on the value of H_{c2}. The situation is clearly represented in figure 2.21.

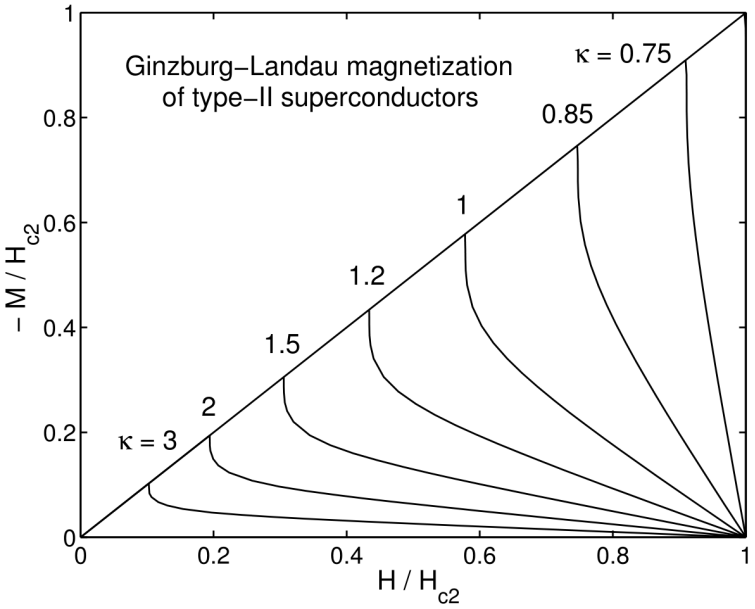

Figure 2.21: Theoretical curve of M vs B for various κ values, from Brandt [59]

A naive interpretation of the magnetisation curve could lead us to claim the minimum value of the magnetisation as H_{c1}. However, because of the presence of a demagnetising factor due to the shape of the sample (further discussed in section 2.3), the correct method to measure H_{c1} would be to linearly extrapolate from the magnetisation curve near the peak [60], as pictured in figure 2.22. But this is only possible in a theoretical scenario: pinning sites cause an hysteresis of the magnetisation, altering the slope. Using this method in practice yields unphysical results, with values of H_{c1} well into the region where a signal is observed. We are therefore unable to deduct a value of H_{c1} using magnetisation measurements.

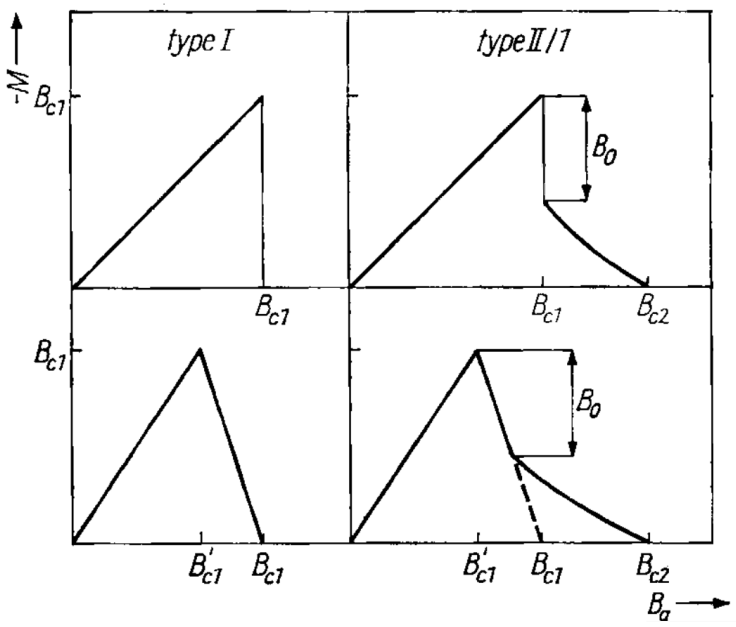

Figure 2.22: Theoretical curve of M vs B for various scenarios, from Brandt *et al.* [60]. Upper row: infinitely long cylinder. Lower row: spherical sample

For the temperature scans, we define the T_c to be the mid-point of the transition. It simply corresponds to the maximum in the derivative, as pictured in figure 2.23, which we fit using a Gaussian.

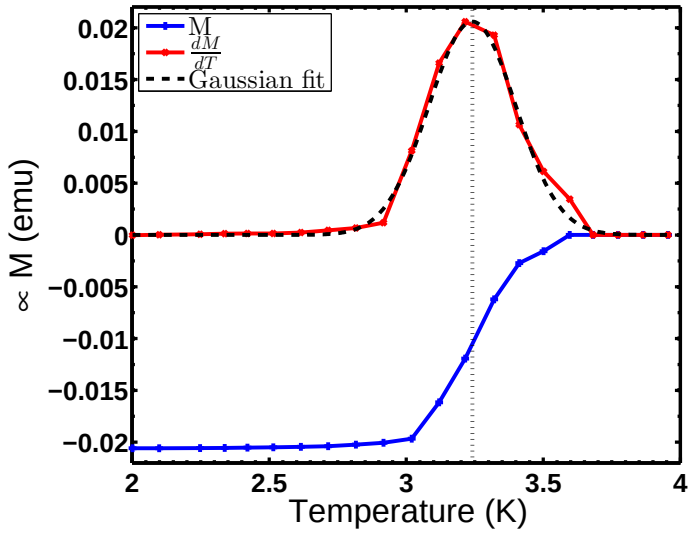

Figure 2.23: Magnetic moment (units: [M].[mass]) versus temperature (B = 50 G) for B ∥{010} and its derivative (scaled)

On a side note, significant time was spent trying to measure the superconducting transition of BiPd using a heat capacity setup, previously used to measure niobium [61]. Unfortunately, no meaningful signal was

observed.

Figures 2.24 and 2.25 summarise the measurements listed previously. From the intensity of the diffraction pattern at low temperature, we estimate H_{c2} to be 650 ± 50 G for B ∥ {010} and 700 ± 50 G for B ∥ {101}/"{100}" respectively. This is estimated by noticing that at 600 and 650 G, the diffraction pattern are extremely weak (barely above background noise), so we argue it is likely for the signal to disappear 50 G above that point.

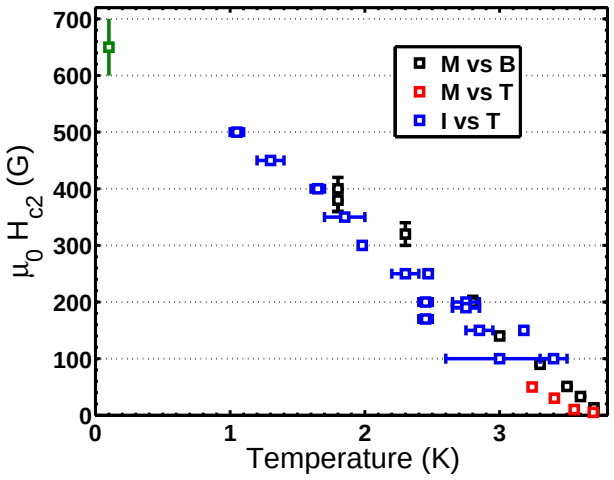

Figure 2.24: H_{c2} versus temperature for B ∥ {010}. The origin of the low temperature point (green) is explained in the text.

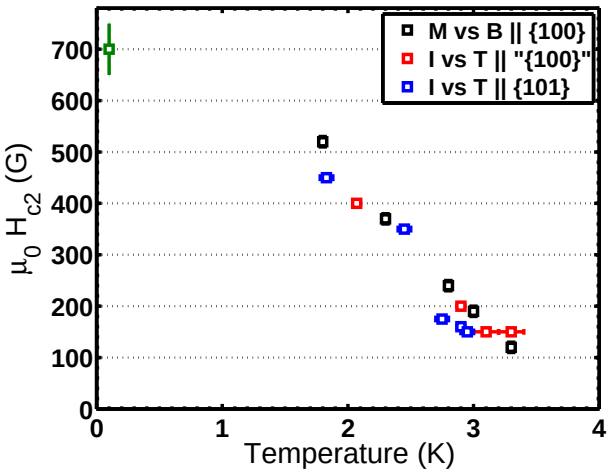

Figure 2.25: H_{c2} versus temperature for B ∥ {101} and "{100}"

Discussion

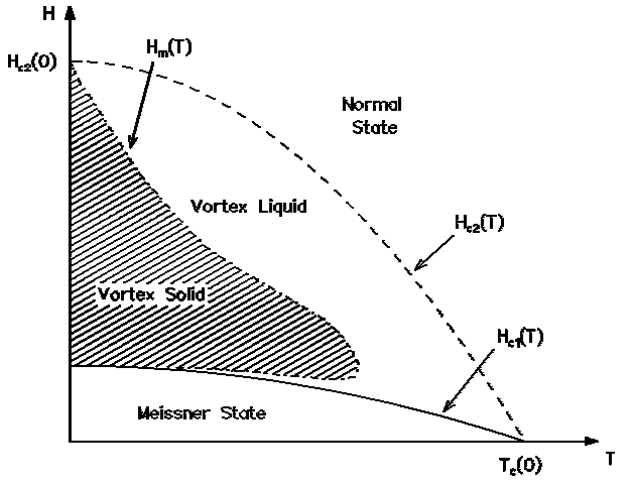

Figure 2.26: Illustration of the melting of the FLL in high-T_c superconductors. From J.E. Sonier [62]

In high-T_c superconductors, the presence of a vortex liquid phase has the effect of driving the intensity of the signal to zero before the end of the superconducting phase [63] (figure 2.26). The transition at which the melting occurs, H_m, has the following form

$$\frac{H_{c2}(T) - H_m(T)}{H_{c2}(0)} \propto \left[\frac{t\,(1-t^2)}{c_L^2}\right]^{\frac{2}{3}} \sqrt{G_i}$$

Where the reduced temperature $t = \frac{T}{T_c}$, c_L is the Lindemann number, characterising the melting transition as the point where thermal fluctuations reach a fraction of the vortex lattice spacing, $l = c_L\, a_{FLL} \approx 0.2\, a_{FLL}$ [64]. $G_i \propto \frac{1}{\xi^3(0)}$ is the Ginzburg number describing the strength of the fluctuations.

For low-κ superconductors, ξ is large and we expect the melting transition to be close to H_{c2}. Indeed, studies in the low-κ superconductor niobium estimated the melting line to be of the order of 7 mK [58] below H_{c2}. Furthermore, it is worth to mentioning that experimental evidence of melting has not been seen in this material [61].

This means that, while the presence or absence of a melting transition cannot be asserted with confidence, given the experimental precision and the scope of the present study, the possible presence of the melting transition is not a cause of concern.

We can notice the similarity between data collected with the beam oriented along "{100}" and {101}. Unfortunately, both the lack of additional data, especially at low temperatures, and the precision of the measurements prevent us from drawing any conclusions about a potential anisotropy between these orientations. Comparing this with the {010} data however leads to a typical ratio

$$\frac{H_{c2}\{101\}}{H_{c2}\{010\}} \approx 1.2 - 1.3$$

Plotting our data in figure 2.27, along with the values of $H_{c2}(T)$ reported by Joshi *et al.* [56] for B $\parallel$ {010}, we can immediately notice a significant difference. The resulting large ratio $\frac{H_{c2}(\text{sample grower}))}{H_{c2}(\text{data})} \approx 10$ is also observed by Sun *et al.* [65] (see figure 2.29).

It has been proposed that an enhancement of H_{c2} takes place near defects in non-centrosymmetric superconductors, due to magnetoelectric effects inhibiting the formation of supercurrents [66]. We cannot directly see if our samples have such twin boundaries, but STM experiments [65] performed on a different BiPd sample, looking at the modulation of the height and the interatomic distance were able to image two twinned domain orientations (010) and $(0\bar{1}0)$ (figure 2.28).

This enhancement is not a bulk effect, so it is not noticeable when measuring the magnetisation of the sam-

ple. When probing H_{c2} with resistivity (Joshi *et al.*), twin boundaries will govern the signal because of the enhanced H_{c2}. Reducing the drive current allows regions with lower H_{c2} to contribute to the signal and features consistent with lower H_{c2} appear [65].

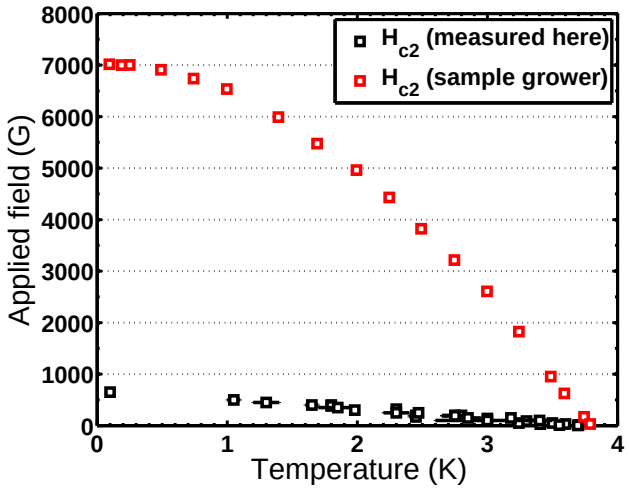

Figure 2.27: Comparison of different measurements of the upper critical field versus temperature for B ∥ {010}

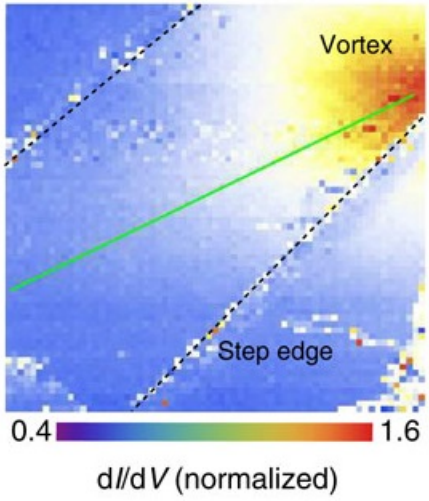

Figure 2.28: STM scan of BiPd showing a vortex pinned to the twin boundary. From Sun *et al.* [65]

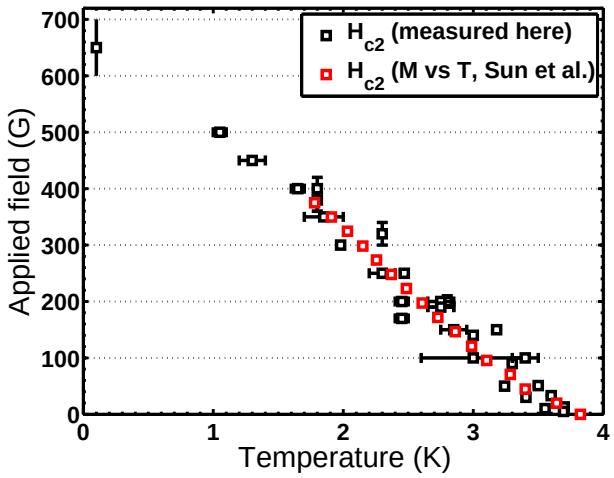

Figure 2.29: H_{c2} versus temperature, B ∥ {010}

As previously outlined, the lack of measurements in the low temperature part of the phase diagram makes the determination of $H_{c2}(0)$ hard. A possible way of doing this is to linearly extrapolate the high temperature measurements: although a linear fit leads to a relatively sensible value of $\sim$ 750 G for B ∥{010} (see figure 2.24), the the same treatment for B ∥{101} gives rise to an unrealistic value larger than 900 G (figure 2.25). Given the experimental evidence, this inconsistency makes it difficult to judge whether this is a valid method.

Assuming orbital pair-breaking is dominant, we can estimate two values of $\xi = \sqrt{\frac{\Phi_0}{2\pi H_{c2}}}$:

$$\text{B} \parallel \{010\}\text{: } \xi \approx 710 \pm 30\text{Å}$$

$$\text{B} \parallel \{101\} \text{ or } \text{“}\{100\}\text{”: } \xi \approx 685 \pm 30\text{Å}$$

Most of the values found in the literature (Joshi *et al.* [56] and Jiao *et al.* [67]) are based on the high $H_{c2}(0)$ measured using resistivity, leading to an artificially low $\xi \approx 230$ Å that does not characterise the bulk behaviour. For B $\parallel \{010\}$, Sun *et al.* [65] find a slightly higher $H_{c2}(0) \approx 750$ G from linear extrapolation of the magnetisation at low temperature, leading to a coherence length of 660 Å. They also derive a ξ value of 600 Å from STM measurements, corresponding to $H_{c2}(0) \approx 915$ G.

Setting aside the issue of consistency between their measurements, we can see that our estimated value lies below their estimates. This can be caused by disorder/impurities, lowering the value of H_{c2}. A common way to estimate the upper critical field taking into account the effect of impurities is to use the Werthamer-Helfand-Hohenberg (WHH) formula [68]. It links the slope of H_{c2} near T_c to $H_{c2}(0)$ by

$$H_{c2}(0) = -0.69 \frac{\mathrm{d}H_{c2}}{\mathrm{d}T} T_c \quad \text{in the dirty limit}$$

$$H_{c2}(0) = -0.73 \frac{\mathrm{d}H_{c2}}{\mathrm{d}T} T_c \quad \text{in the clean limit}$$

Orientation	$\boldsymbol{H_{c2}(0)}$ **(dirty limit)**	$\boldsymbol{H_{c2}(0)}$ **(clean limit)**	$\boldsymbol{H_{c2}(0)}$ **(observed)**
B $\parallel \{010\}$	463 Å	490 Å	650 Å
B $\parallel \{101\}$	613 Å	648 Å	700 Å

Table 2.3: WHH formula applied to BiPd

Results are shown in table 2.3. They are difficult to interpret: we previously determined by the observation of dHvA oscillation and high RRR that our samples do not contain a large amount of impurities and have a large mean free path $l \gg \xi$ [56]. The clean limit value being closer to the observed $H_{c2}(0)$ tends to confirm this. At the same time, there is a large difference of 150 G between the observed and predicted value for B $\parallel \{010\}$, while the clean limit values for B $\parallel \{101\}$ are within 50 G.

We could explain these differences by recalling that the WHH theory is describing a single band BCS superconductor, whereas the situation of BiPd is likely to be more exotic.

2.3.4 The Intermediate Mixed State

Looking at the field dependence of the reciprocal lattice vector norm q, Figure 2.30 shows that BiPd displays a peculiar behaviour:

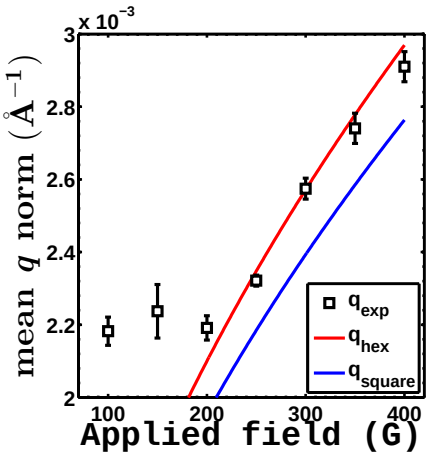

Figure 2.30: Average q versus B, B ∥ {010} at T = 1.1 K

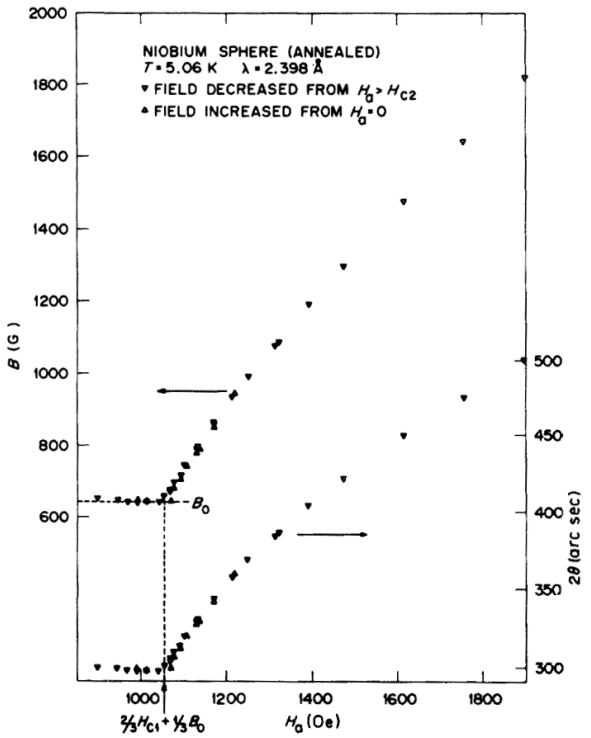

Figure 2.31: Scattering angle 2θ and calculated flux density of a niobium sphere versus applied field, for T = 5.06 K. From Christen *et al.* [69]

The red and blue lines correspond to hexagonal ($\theta_{FLL} = 60°$) and square ($\theta_{FLL} = 90°$) predictions for the flux line lattices.

At high fields, the data agrees with the ideal Abrikosov hexagonal lattice $q = \sqrt{\frac{B \sin(\theta_{FLL})}{\Phi_0}}$ dependence. At low field, q deviates from this behaviour and stays constant. This is the hallmark of a phenomenon called the Intermediate Mixed State (IMS), observed by SANS in niobium by Christen *et al.* [69] (figure 2.31).

In Type II superconductors, the supercurrents created by the vortices overlap, leading to a repulsive vortex-vortex interaction. This is in contrast with Type I materials where, because of the low κ value, the normal-superconducting wall energy is positive (attractive interaction) and macrosopic normal domains appear (Intermediate State).

Superconductors showing an IMS display a behaviour between Type I and II. It is often called Type II/1 superconductivity, to be distinguished from the more common Type II (also 'Type II/2') superconductors.

Indeed, in such materials, Type II regions coexist with Meissner domains, as seen in figure 2.32. More precisely, these Type II regions have a constant FLL spacing due to a minimum in the vortex-vortex interaction potential (long-range attraction, short-range repulsion [70]), possibly coming from an imaginary value of the penetration depth, arising from non-local dynamics [71].

In the IMS, the constant FLL spacing implies constant flux density, but the total flux still has to vary when the field changes. As a result, in the IMS, the volume fraction of superconducting domains (with constant q) varies as a function of the applied magnetic field.

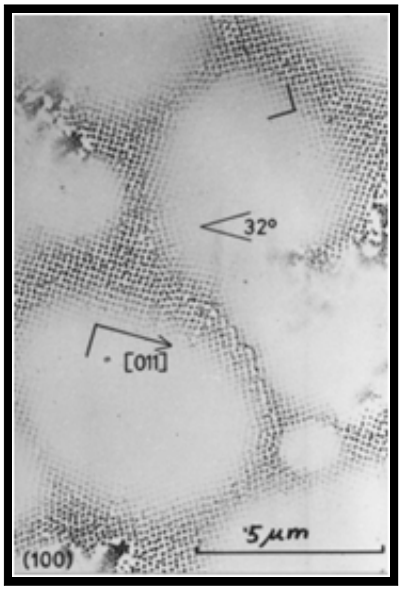

Figure 2.32: IMS in high purity niobium disk by decoration of Fe microcrystallites. From Brandt *et al.* [71]

This behaviour appears in the range of magnetic fields between

$$(1-n)\,H_{c1} < H_{app} < (1-n)\,H_{c1} + n\,B_0$$

where n is the demagnetising factor, H_{app} the applied field and B_0 the limiting flux density.

Above this region, the superconductor behaves like a Type II material; at lower fields, it displays a Type I behaviour.

In the IMS region, the integrated intensity is proportional to the volume fraction of constant FLL (see figure 2.34), denoted $\eta(H_a) \propto \frac{H}{H_{IMS}}$ where $H_{IMS} = (1-n)\,H_{c1} + n\,B_0$ is the upper bound of the IMS.

The IMS is seen in a few materials such as niobium, lead-indium or tantalum-nitrogen alloys [71]. Figure 2.33 shows the phase diagram of niobium: in addition to the presence of an IMS, the rich FLL structure is determined by the Fermi surface reconstruction and non-local effects [73].

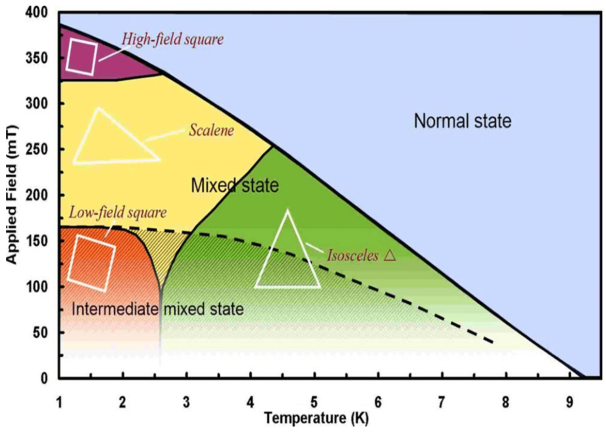

Figure 2.33: Phase diagram of niobium for B ∥ (001), from Laver *et al.* [72]

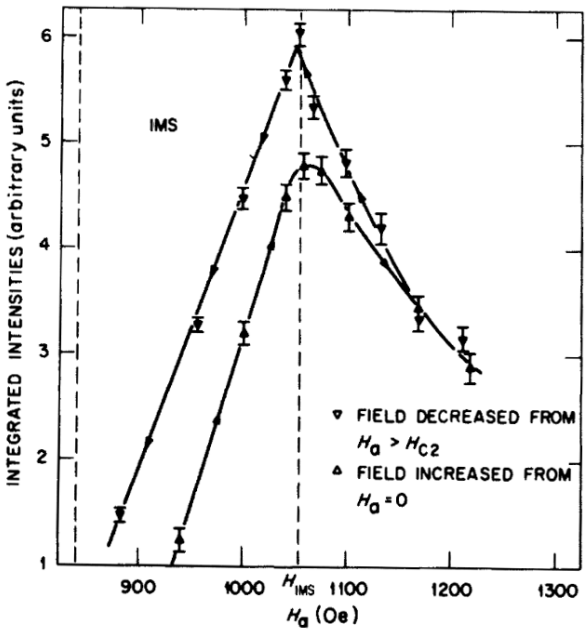

Figure 2.34: Integrated intensity versus field for a niobium sphere at T = 5.06 K. From Christen *et al.* [69]

In the same fashion, we can use SANS to map the superconducting phase of BiPd.

Field scan analysis

As seen above, a straighforward way of defining the boundary of the IMS is to look at the point that separates the theoretical $q \propto \sqrt{H_{app}}$ and constant q regions when varying the field.

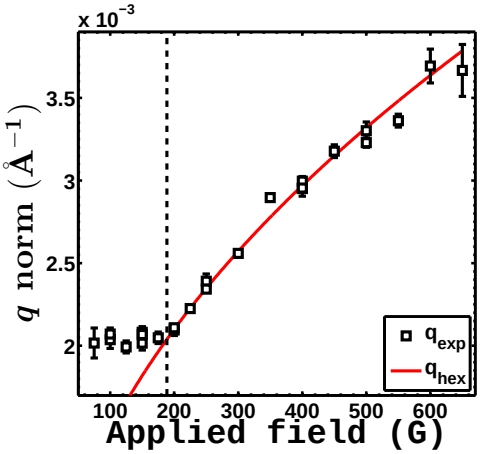

Figure 2.35: q versus B, B ∥ "{100}", T = 0.1 K

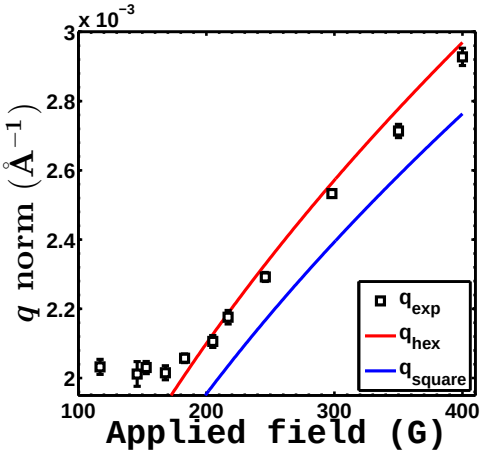

Figure 2.36: q versus B, B ∥ {101}, T = 0.1 K

We notice small deviations from the hexagonal lattice above the IMS upper boundary in a few cases, as pictured in figure 2.36. Although great care has been exerted to correctly calibrate the magnets, the unusually low working fields applied may be shifted by small non-linearities of or remnant field in the electromagnet. Another potential cause could be the fact that because the superconducting samples are not ellipses, the internal magnetisation is not homogeneous, although this effect diminishes as the applied field approches H_{c2}, because M becomes smaller.

Table 2.4 lists the H_{IMS} values obtained for the upper bound of the IMS.

Orientation	**T**	$\boldsymbol{H_{IMS}}$	$\boldsymbol{\sigma_{H_{IMS}}}$
$\parallel$**{010}**	0.05	223.3	2.3
	0.1	229.2	3.1
	1.1	218.1	5.3
	1.5	218.7	2.8
$\parallel$**"{100}"**	0.1	190.3	5.8
	1.5	166.6	6.7
$\parallel$**{101}**	0.1	187.5	10.7
	1.1	188.6	3.0
	1.5	176.2	7.8

Table 2.4: Quantities extracted from q vs B curves

A different way of approaching the problem is to calculate the internal field, which is linked to the magnetic flux quantum Φ_0 by

$$B_{int} = \frac{4\,\pi^2\,\Phi_0}{A_s}$$

the denominator being the area of the first Brillouin zone previously defined.

Figure 2.37 shows a typical B_{int} versus magnetic field curve. Fitting this calculates two quantities:

- the point on the x-axis where the internal field changes from a constant to varying value is H_{IMS}
- the low-field constant value on the y-axis is a direct measure of B_0

We report the results of the fits in table 2.5, figures 2.49 and 2.50. These values of H_{IMS} are consistent with the previous results of table 2.4. We see that the values of H_{IMS} and B_0 are equal within error bars:

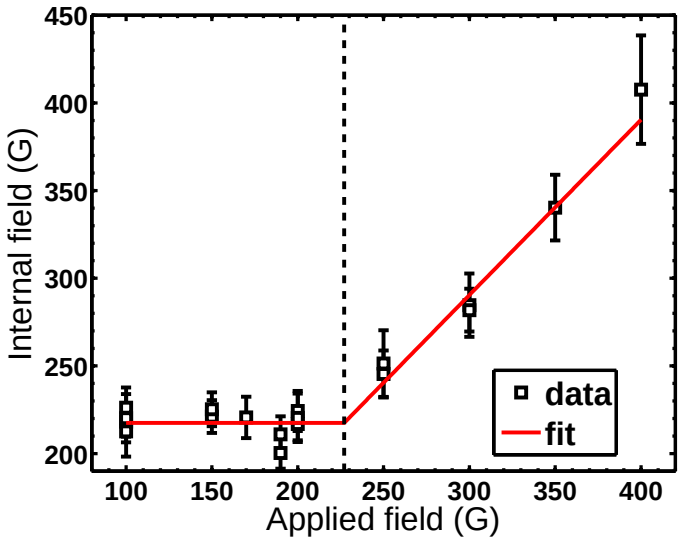

Figure 2.37: Internal field (calculated from FLL) versus applied field, B ∥ {010} T = 1.5 K

Orientation	**T**	H_{IMS}	$\sigma_{H_{IMS}}$	B_0	σ_{B_0}
∥**{010}**	0.05	227.1	4.9	224.4	2.9
	0.1	237.2	6.7	229.6	2.6
	1.1	220.5	6.0	216.4	5.0
	1.5	227.1	5.3	217.5	2.2
∥**"{100}"**	0.1	186.1	5.4	183.6	3.4
	1.5	170.0	9.2	161.3	5.8
∥**{101}**	0.1	189.7	5.2	178.1	3.4
	1.1	187.8	4.9	178.2	3.2
	1.5	185.2	3.9	173.5	2.3

Table 2.5: Quantities extracted from B_{int} versus B curves

Our samples have a geometry which resembles a flat plate, with an associated value of the demagnetising factor close to 1. Recalling the expression of H_{IMS}, this directly leads to $H_{IMS} \sim B_0$.

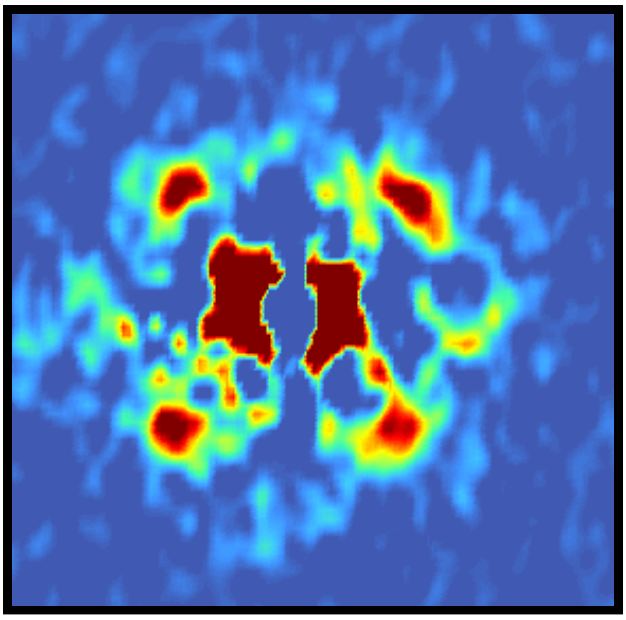

Figure 2.38: Diffraction pattern in the IMS phase (B = 100 G, T = 1.5 K), beam ∥ {101}

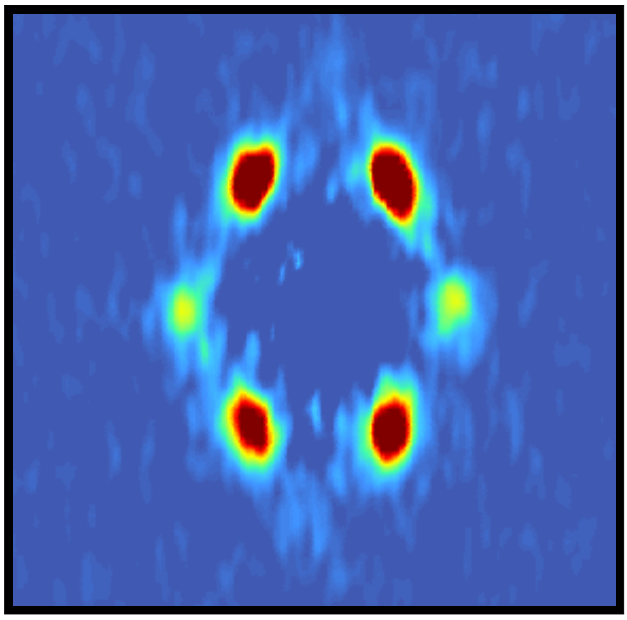

Figure 2.39: Diffraction pattern out of the IMS phase (B = 250 G, T = 1.5 K), beam ∥ {101}

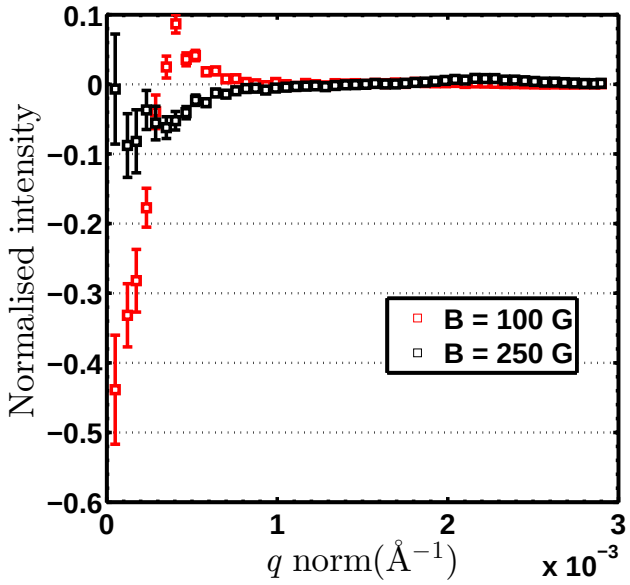

Figure 2.40: Intensity of the signal as a function q, in (red) and out (black) of the IMS

As previously seen, the IMS consists in the coexistence of Type I and Type II domains, on a much larger scale than the typical interplanar distance of the FLL. In this phase, we can observe low-q scattering of these domains because of the difference in magnetic potential experienced by neutrons. This scattering can be seen as additional intensity near the centre of the diffraction pattern, in a region usually masked by a beamstop,

used to prevent the detector from being damaged from neutron exposure. This effect is shown in figures 2.38 and 2.39. We can also reduce the signal from 2D to 1D by summing the intensity around the origin as a function of distance (interchangeably, q).

After background substraction, we plot this I vs q curve in figure 2.40. It shows a dip near the origin: this is simply the intensity being scattered away from the direct beam to the low-q features.

We can measure and model this behaviour using the foreground and background data. Let I_{FG} be the intensity observed for the foreground data, excluding the signal coming from the vortex lattice, we can model it by the following:

$$I_{FG} = I_{BG}\, x + \frac{I_{IMS}}{\sqrt{2\,\pi}\,\sigma_{IMS}}\, e^{\frac{-q^2}{2\,\sigma_{IMS}^2}}$$

The variable x represents the amount of intensity scattered away from the direct beam. We model the IMS by a gaussian contribution, parametrised by its peak intensity I_{IMS} and variance σ_{IMS}.

Testing this model on the field dependence, we use at first a fitting routine that allows all the parameters to vary to find the value of σ_{IMS} to fix, shown in figure 2.41.

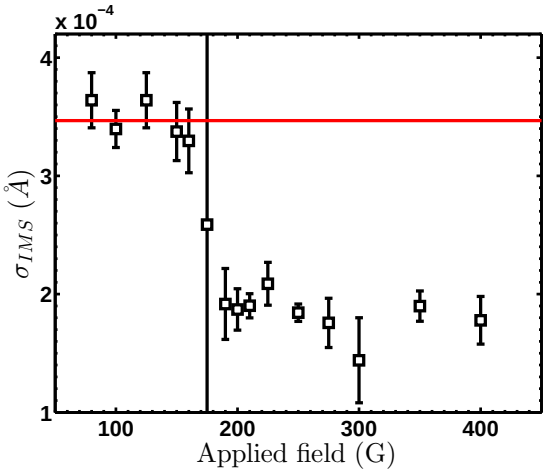

Figure 2.41: σ_{IMS} versus applied field for B ∥ {010}, T=1.5 K. The red line represents the value in the IMS

Assuming only the height of the peak changes as field increases (meaning the range of distribution of domain size does not change, only their total volume) we can then model the remaining parameters, shown in figure 2.42 and 2.43.

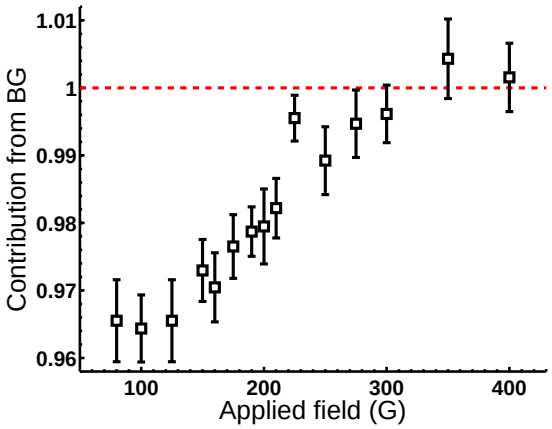

Figure 2.42: Background contribution versus B, B ∥ {101}, T = 1.5 K

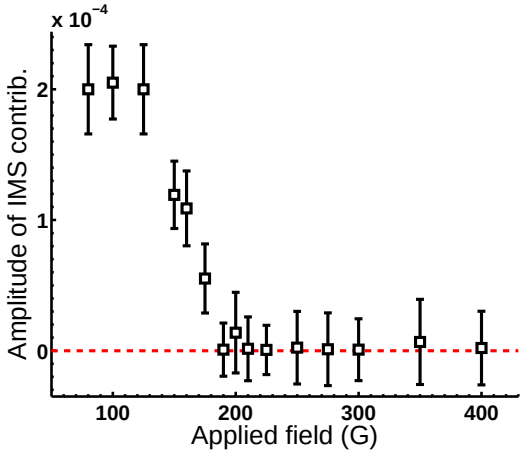

Figure 2.43: Contribution of the IMS versus B, B ∥ {101}, T = 1.5 K

We find $H_{IMS} = 190 \pm 5$ G for B ∥ {101} at T = 1.5 K.

Temperature scan analysis

Temperature dependences were analysed in the same fashion at 150 G and 160 G. Both point to the disappearance of the IMS at approximately 2.5 K (figure 2.44). The vertical blue line represents T_c at this field. Attempts were made to improve the results by using a cryostat with lower background in the hope of reducing the low-q scattering, but similar results were found with no improvements.

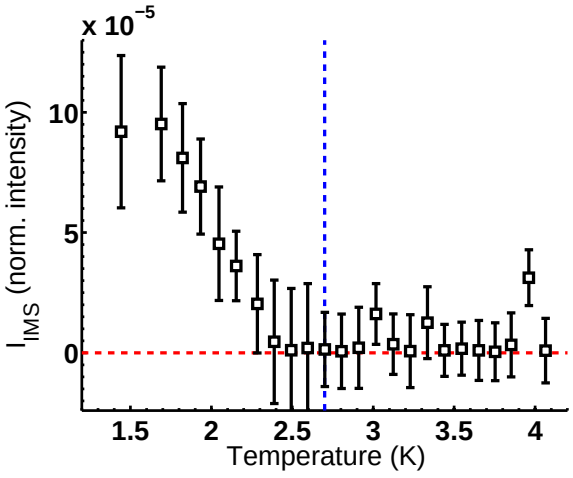

Figure 2.44: Contribution of the IMS versus temperature, B ∥ {101}, $H_{app} = 150$ Oe

Below H_{IMS}, both the reciprocal lattice vector and the internal field should follow the same behaviour, drawn in figure 2.45

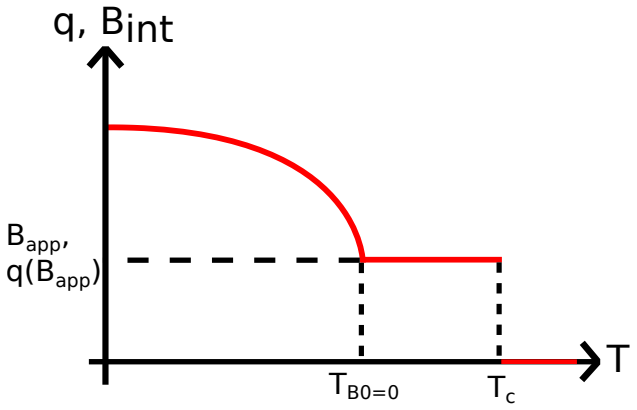

Figure 2.45: Diagram representing the internal field or the q vector versus temperature for $H < H_{IMS}$

This is because q and B_{int} alike follow the shape of $B_0(T)$, up to a first plateau where $B_0 = 0$, and then remaining in the superconducting but non-IMS phase until dropping to zero at T_c.

The data however are very ambiguous as to the extent of the IMS phase, in most cases not even reaching the first plateau as seen in figure 2.46

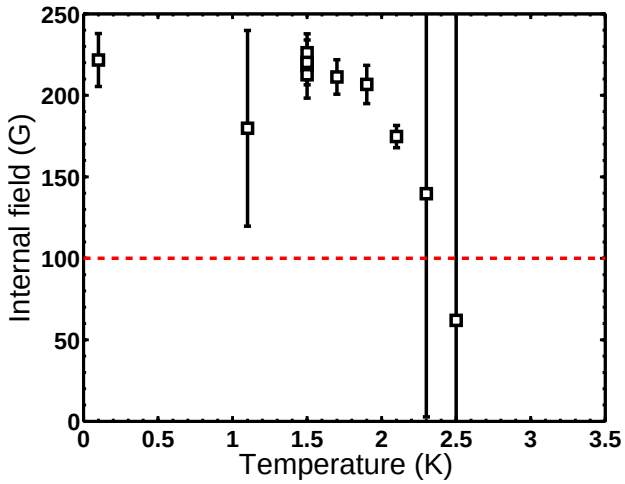

Figure 2.46: Internal field versus temperature for B = 100 G and B ∥ {010}

Keeping the above in mind, we find the following results for B ∥ {010} and "{100}" (table 2.6):

Orientation	H_{app} (Oe)	$T(B_0 = 0)$ (K)	$\sigma_{T(B_0=0)}$ (K)
‖{010}	100	2.5	0.1
	150	2.75	0.15
	190	1.95	0.15
	200	1.9	0.2
‖"{100}"	150	2.3	0.3

Table 2.6: Quantities extracted from B_{calc} versus temperature

Gathering the data described above allow us to plot the the limits of the IMS in a field-temperature phase diagram, For both B ‖ {010} and "{100}" or {101} in figure 2.47 and 2.48.

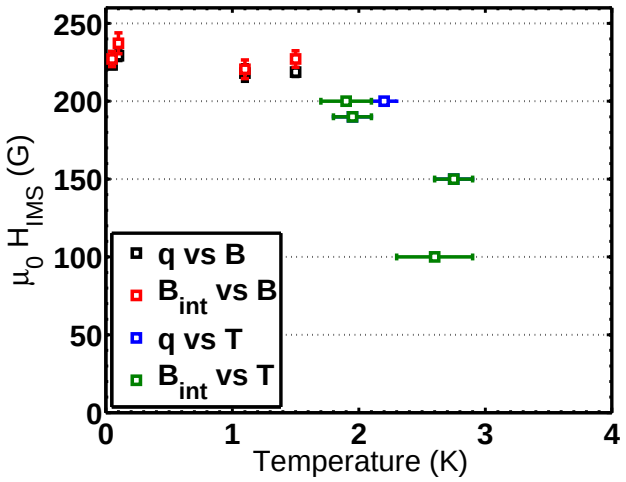

Figure 2.47: Phase diagram of the IMS for B ‖ {010}

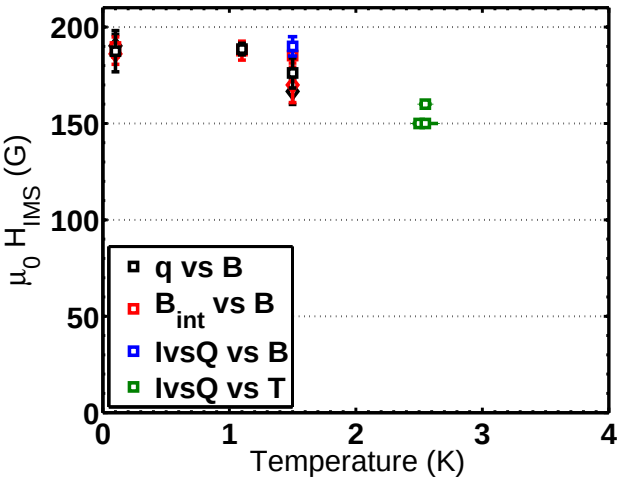

Figure 2.48: Phase diagram of the IMS for B ‖ "{100}" or {101}

Discussion

The following graphs summarise the phase diagram of BiPd along the different orientations.

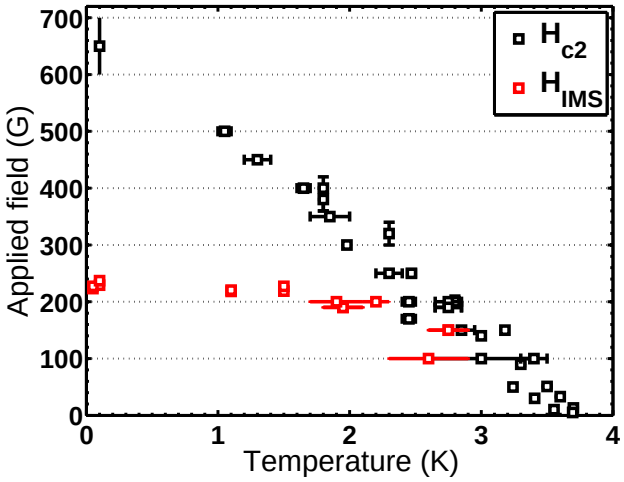

Figure 2.49: Phase diagram of BiPd for B ∥ {010}

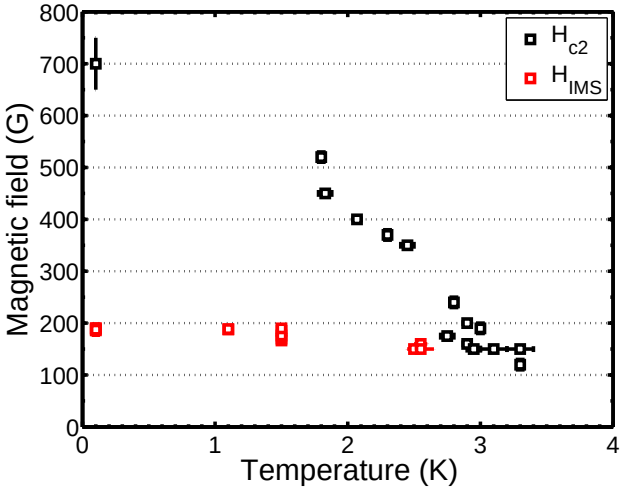

Figure 2.50: Phase diagram of BiPd for B ∥ "{100}" or {101}

The same situation arises as when comparing H_{c2}: there is no experimental difference of the values of H_{IMS} between "{100}" and {101}, and we also observe a typical H_{IMS} ratio of 1.2 - 1.3 between {010} and {101}.

The aim of this last section was to map the extension of IMS on the phase diagram, more precisely to try to determine how it varies as temperature increases. While the data seem to display a small decrease in temperature, suggesting that the IMS subsists until the superconducting transition, the quality of the FLL at low fields and high temperatures prevents us from making a strong claim.

The question of the extent of IMS remains.

2.3.5 Form factor analysis

We calculate the form factor of the reciprocal lattice (see section 1.2):

$$FF_{h,k} = \sqrt{\frac{\mathrm{II}\,\Phi_0^2\, q_{h,k}\, \cos(\zeta)}{2\,\pi\, V\, \phi_n\, (\frac{\gamma}{4})^2\, \lambda_n^2}}$$

Figure 2.51 shows the form factor for each spots. We notice that two of them have a lower form factor than the rest. They correspond to the weak (or high-q) spots identified previously. London theory states the form factor as

$$FF = \frac{B}{1 + q^2\,\lambda^2}$$

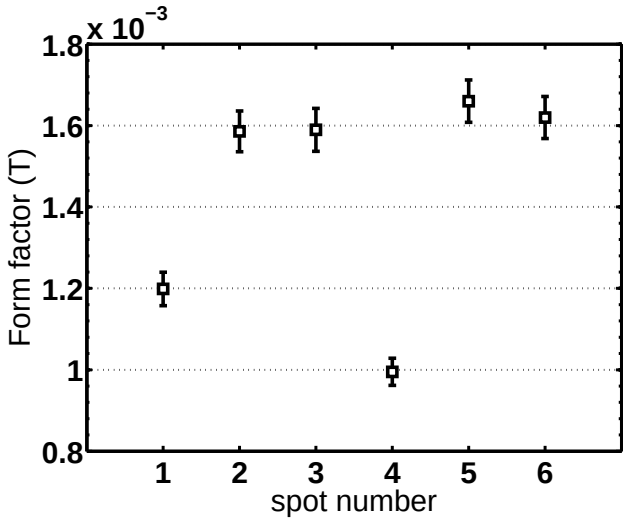

Figure 2.51: Form factor versus spot number, B ∥ (010) at 200 G and 1.5 K

A common approximation is $q^2\lambda^2 \gg 1$ (large λ), and since $q \propto \sqrt{B}$ we see that within this theory, the form factor is constant (therefore it does not depend on q). Figure 2.51 clearly shows that these assumptions, no vortex core ($\xi = 0$, field diverges at the core centre) and the absence of non-local effects do not describe the vortex lattice in BiPd well.

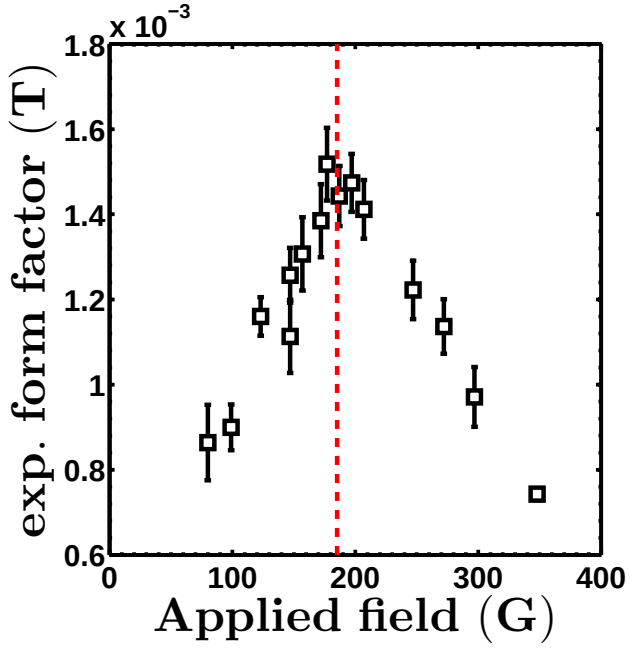

Figure 2.52: Form factor versus B, B ∥ {101} T = 1.5 K

Figure 2.52 shows a typical variation of the experimental form factor with applied field. This is a slight misuse of the name for practical purposes: because the q-value is constant in the IMS, the value of the form factor is also constant [69]. The integrated intensity varies as

$$\mathrm{II} \propto |FF|^2 \, V_{FLL}$$

$$V_{FLL} = V \, \eta(H_{app})$$

V_{FLL} is the volume of sample containing a flux line lattice. In the IMS, V_{FLL} is only a fraction of V, the superconducting volume above the IMS: this effect is taken into account by multipling V by η, the volume fraction of FLL. It follows that the 'form factor' plotted here is actually

$$FF_{plot} = FF \, \eta(H_{app})$$

This is merely a convenience to treat the data more easily, as $\eta(H_{app})$ is not experimentally determined in this thesis. We assume it has the form $\eta = \frac{H_{app}}{H_{IMS}}$: at the upper boundary of the IMS ($H_{app} = H_{IMS}$), $\eta = 1$ and the entire superconducting volume is filled with a flux line lattice ($V_{FLL} = V$). The form factor is modelled using a modified London model, adding to the previous expression a core-correction term, modelling

the effect of the presence of a vortex core:

$$\mathrm{FF}_{lon} = \frac{\mathrm{B}e^{-q^2\,\xi^2}}{1+q^2\,\lambda^2}$$

In the IMS, we fit

$$\mathrm{FF}_{fit} = \eta\,\mathrm{FF}_{lon}(H_{IMS}) = \frac{H}{H_{IMS}}\,\mathrm{FF}_{lon}(H_{IMS}) = \mathrm{FF}_{lon}(H)$$

This means that for this model, the fits for both the IMS and the Type II region are the same. It is expected, because in the IMS the q-value stays constant, the calculated form factor decreases with B.
A typical fit is shown in figure 2.53, and the resulting data in table 2.7. The jaggedness of the fitted curve is caused by the irregularities in q. These irregularities come from the relative lack of reproducibility between experiments: the value of q for each spot is determined by fitting a two-dimensional Gaussian, which in the case of low statistics (e.g. a scan with low counting time, or at low and high fields where the quality of the FLL is not optimal) is skewed by artefacts.

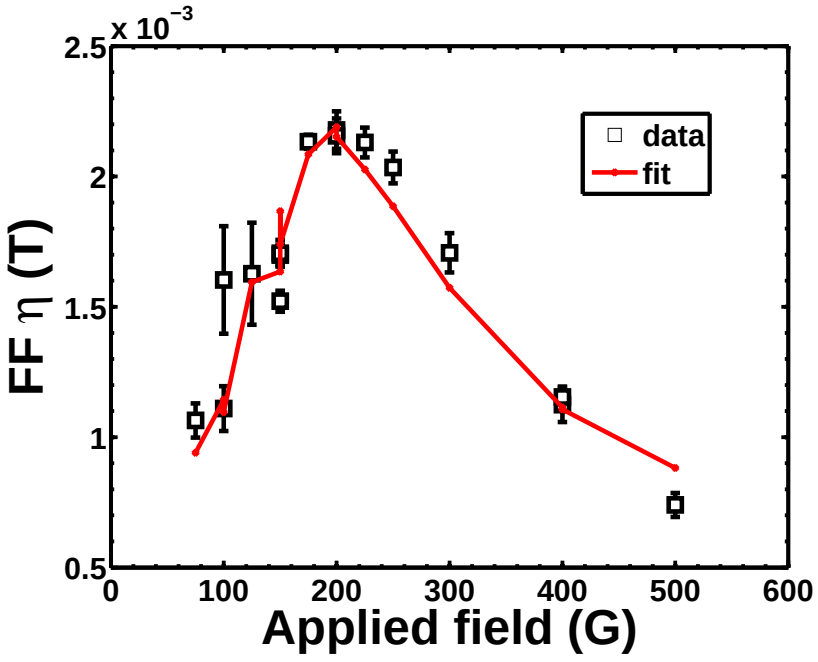

Figure 2.53: Form factor versus B, B ∥ "{100}" T = 0.1 K. The red curve shows London model with core correction

Orientation	**T**	$\boldsymbol{\lambda}$ (Å)	$\boldsymbol{\sigma_\lambda}$ (Å)	$\boldsymbol{\xi}$ (Å)	$\boldsymbol{\sigma_\xi}$ (Å)	$\boldsymbol{\kappa}$	$\boldsymbol{\sigma_\kappa}$
$\|\{010\}$	0.05	871	120	597	61	1.46	0.25
	0.1	616	104	713	57	0.86	0.16
	1.1	413	190	863	90	0.48	0.23
	1.5	297	196	969	78	0.31	0.20
$\|$"{100}"	0.1	826	38	607	23	1.36	0.08
	1.5	852	163	716	82	1.19	0.27
$\|\{101\}$	0.1	744	99	712	40	1.04	0.15
	1.1	765	85	724	40	1.06	0.13
	1.5	757	57	802	26	0.94	0.08

Table 2.7: Quantities extracted from core-corrected London model fit to the experimental data

However, even with a core correction, the London model is still suited only for fields far below H_{c2}, where the flux lines are separated enough not to 'feel' the effect of the vortex core. This condition is fulfilled in high-κ superconductors where H_{c2} is large. In the case of BiPd, working magnetic fields span the range

$$\frac{1}{6} < \frac{H}{H_{c2}} < 1$$

and justifing the validity of such a model becomes problematic.

Surprisingly, very few articles in the literature deal with such constraints. Kealey *et al.* [74] used an algorithm created by Brandt [75] studying Sr_2RuO_4 ($\kappa \approx 2$) and a square FLL. Taking the code used in their analysis, we modify it to suit our needs.

The algorithm itself consists in minimising the Ginzburg-Landau free energy by iterating over a set of equations [75], implementing several numerical tricks to reduce the computational load of the algorithm. This allows to calculate the field distribution and Fourier coefficients of a superconductor with an arbitrary $\kappa \geqslant \frac{1}{\sqrt{2}}$ and $10^{-3} \leqslant \frac{H}{H_{c2}} < 1$.

We integrate this algorithm in the non-linear least square fitting routine (see appendix A). A model curve and results are presented in figure 2.54 and table 2.8.

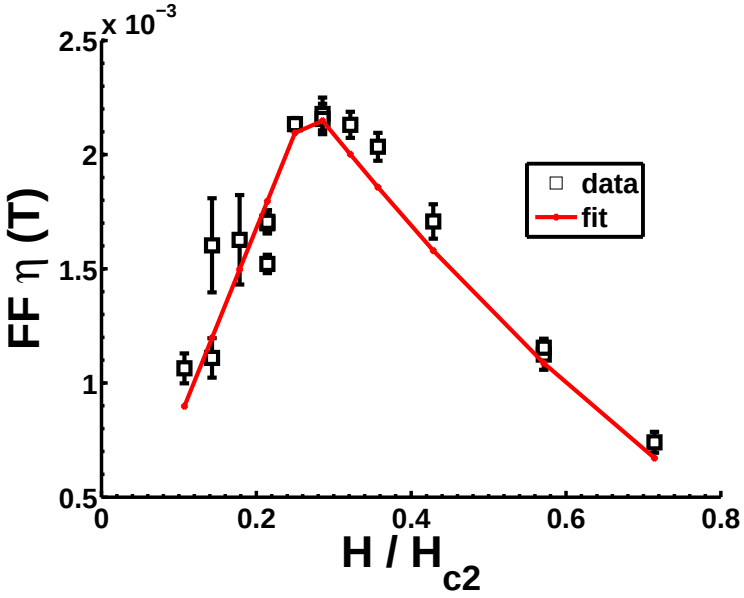

Figure 2.54: Form factor versus B, B ∥ "{100}" T = 0.1 K, fitted using Brandt's method [75]

Orientation	**T (K)**	κ	σ_κ	λ (Å)	ξ (Å)
∥ {010}	0.05	1.09	0.05	776	712
	0.1	1.05	0.05	747	712
	1.1	0.96	0.01	786	820
	1.5	0.91	0.01	804	885
∥ "{100}"	0.1	1.14	0.07	782	686
	1.5	1.13	0.01	864	767
∥ {101}	0.1	1.2	0.06	823	686
	1.1	1.16	0.05	838	723
	1.5	1.14	0.01	874	767

Table 2.8: Quantities extracted from fitting FF vs B (Brandt's algorithm)

Discussion

Looking at the results of the London model fits (table 2.7), we see that it gives us a wide distribution of values. Their variation is enough to confirm that is it indeed not a suitable model for BiPd, but it still manages to capture a correct average value of $\kappa \approx 1$, which is surprising considering it is inexact.

Brandt's algorithm shows a consistent decrease of κ with temperature amongst all orientations, slightly outside error bars.

The algorithm takes an initial value of κ and uses H_{c2} to get ξ and fit λ to the data. Given the uncertainty of H_{c2} (thereby ξ) at low temperature discussed previously (see section 2.3), it would be reasonable to doubt the accuracy of κ. However, it turns out that manually modifing the input values of H_{c2} to account this uncertainty, we find that the value of κ is surprisingly stable, and we reflect the resulting uncertainty by modifing σ_κ in table 2.8.

Currently, all absolute values of λ reported in the literature [56][67] are linked to the wrong values of H_{c2} and ξ in various ways. For the first time we can estimate unbiased values at 0 K:

Orientation	$\boldsymbol{\lambda}$ (Å)	$\boldsymbol{\xi}$ (Å)	$\boldsymbol{\kappa}$
$\parallel\{010\}$	750 ± 50	710 ± 30	1.06 ± 0.05
$\parallel\{101\}$	820 ± 50	690 ± 30	1.19 ± 0.05

Table 2.9: Estimation of superconducting parameters at 0 K

2.3.6 Correlation lengths and instrumental resolution

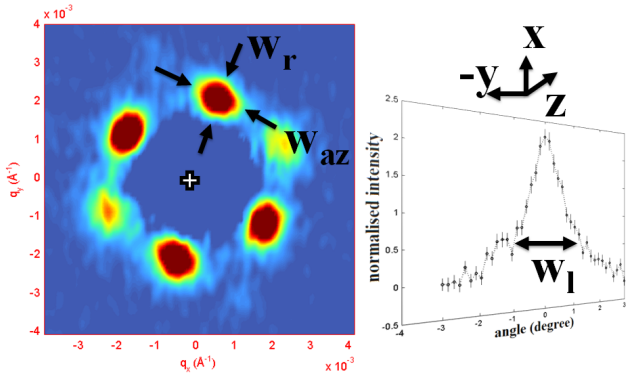

Figure 2.55: Illustration of the geometry of a SANS experiment, showing the longitudinal correlation length w_l along the z direction

The vortex lattice has a quasi-2D geometry, with the flux line extending through all the sample along the z direction. In reciprocal space, this translates into spots whose FWHM along different dimensions correspond to correlation lengths, that is the lengthscale characterising the decay of the autocorrelation function of the magnetisation inside the sample (see section 1.2).

In practice, these spots are pancake-shaped, as the component along q_z is smaller than the ones in-plane. Three dimensions are usually considered: the radial, azimuthal and longitudinal width, as illustrated in figure 2.55.

The radial correlation length w_r is directly measured on the detector, but the other two require additional calculations to transform them into reciprocal space quantities:

$$w_l = q\ \cos(\zeta)\ \tan(\text{FWHM}_{long.})$$

$$w_{az} = q\ \sin(\text{FWHM}_{azim.})$$

To calculate the instrumental resolution, we follow the treatment of Cubitt *et al.* [76] where the authors assume a Gaussian distribution FWHM of the incoming neutron beam a, mosaic spread b and Bragg angle $c = \theta\sqrt{(\frac{\delta\lambda}{\lambda})^2 + (\frac{\delta d}{d})^2}$.

θ is the centre of the rocking curve and the two terms under the square root are respectively the contribution from the wavelength spread and lattice parameter.

Since our goal is to calculate the contribution of the experimental setup only, leaving aside everything coming from the superconducting sample, we set $b = \frac{\delta d}{d} = 0$. It follows that

$$W_r = \sqrt{\frac{a^2\,c^2}{a^2+c^2}}$$

$$W_{az} = \sqrt{a^2+c^2}$$

$$W_l = a$$

W_r, W_{az} and W_l being the radial, azimuthal (in scattering plane) and longitudinal (out-of-plane, i.e. in the direction of the rock) FWHM of the angle distribution, that is the different components of the instrumental resolution.

Because the sample acts as a pinhole, we can calculate a by directly measuring the FWHM of the direct beam. c is straightforward knowing the typical wavelength resolution for SANS instruments is 0.1.

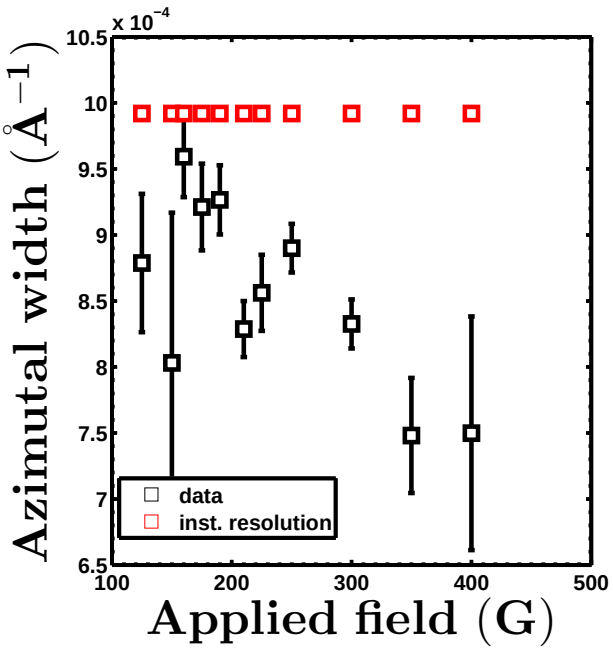

Figure 2.56: Azimutal width versus field, B ∥ {101}, T = 1.1 K

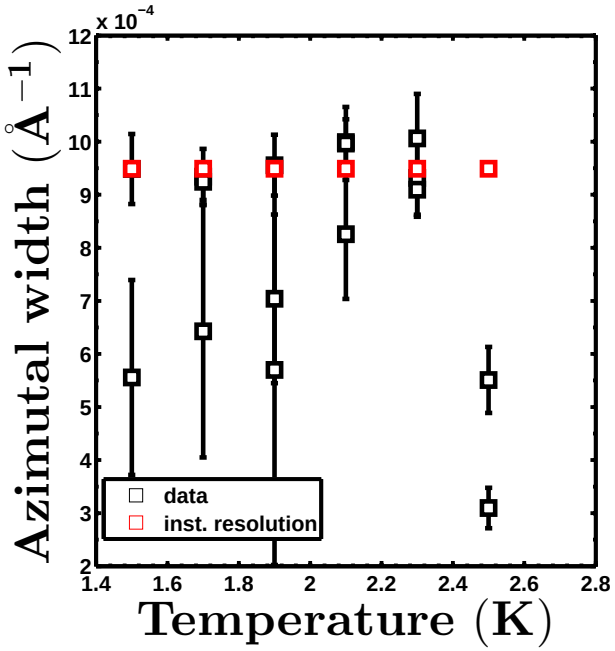

Figure 2.57: Azimutal width versus temperature, B ∥ {010} and B = 190 G

Figures 2.56 and 2.57 show typical variations of the azimuthal width of the spots. In this case, experimental width values are equal to or lie below the resolution, meaning that the measurement is restricted by the instrument's precision and subject to untraceable systematic errors, preventing us from drawing conclusions.

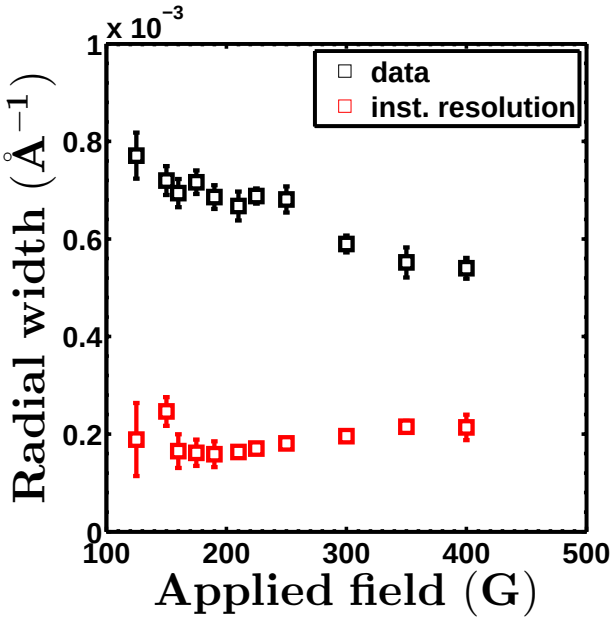

Figure 2.58: Radial width versus field, B ∥ {101}, T = 1.1 K

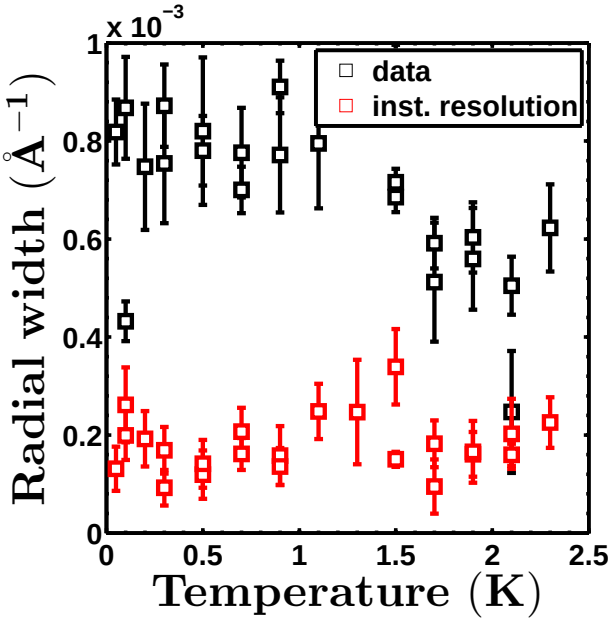

Figure 2.59: Radial width versus temperature, B ∥ {010} and B = 200 G

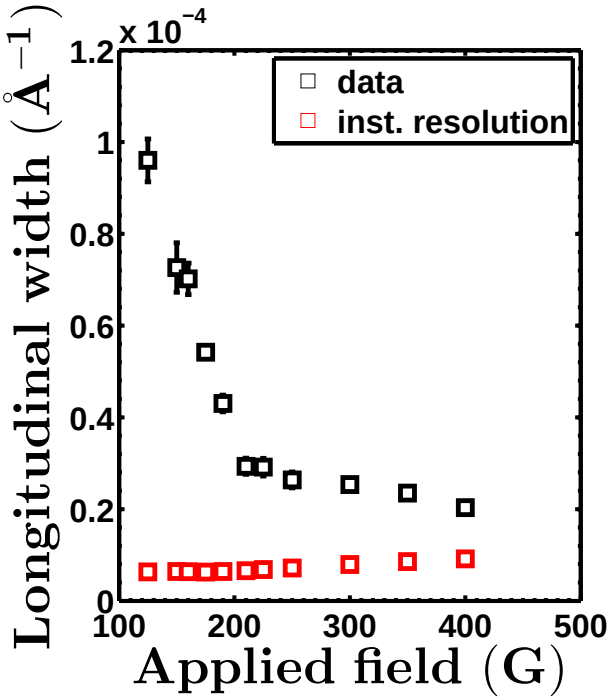

Figure 2.60: Longitudinal width versus field, B ∥ {101} and T = 1.1 K

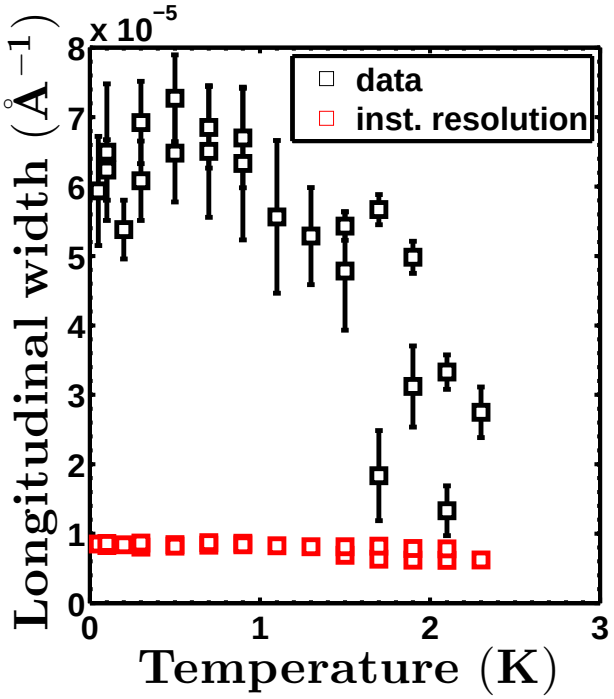

Figure 2.61: Longitudinal width versus temperature, B ∥ {010} and B = 200 G

Figures 2.58 and 2.61 illustrate the variation of the radial and longitudinal widths. Unlike the previous

graphs, these quantities are above instrumental resolution. We can clearly see a general decrease with increasing temperature and field. Since the quantities measured are correlation lengths in reciprocal space, this means the quality of the FLL improves in both directions: radially, the FLL has less deviations from the average structure, and out-of-the plane, the flux lines are straighter. This can be explained by a depinning effect induced both by increasing temperature (thermal fluctuations) and field (vortex-vortex repulsion).
As previously discussed, given the conditions of our experiments, the presence of an observable melting transition is unlikely. The fact that we do not see an increase in correlation length, characteristic behaviour of a vortex lattice undergoing a melting transition, reinforces that conclusion.

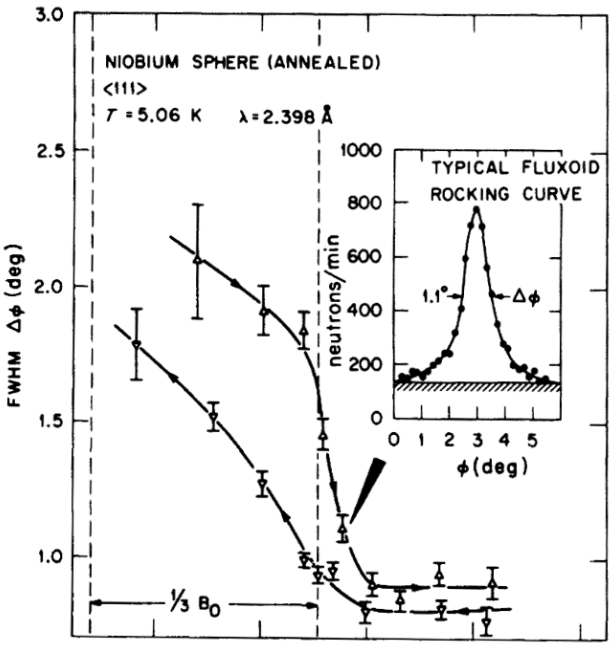

Figure 2.62: Rocking curve FWHM versus applied field for a niobium sphere at T = 5.06 K. From Christen *et al.* [69]

Figure 2.61 shows a sharp decrease the longitudinal correlation length with increasing field in the IMS. This effect, also seen by Christen *et al.* [69] (figure 2.62), is claimed to be caused by particle broadening, an effect which links the size τ of domains to the broadening of the peak β by $\beta \propto \frac{1}{\tau}$. As field increases, the domain size of superconducting regions containing a vortex lattice increases, leading to a decrease of the width/broadening.

2.3.7 Muon spin rotation

Muon spin rotation or μSR is a technique taking advantage of the precession of the muon in a magnetic field. Once deposited inside the sample, usually at interstitial lattice sites (muons have a positive charge), their spin precess in the local field until they decay, with a half-life $T_\mu \approx 2.2\ \mu$s. The decay process emits a positron with an asymmetric distribution, preferentially along the spin direction. The value of the asymmetry is measured over multiple muon decays and over time, as illustrated in figures 2.63 and 2.64 and is used to calculate the internal field distribution.

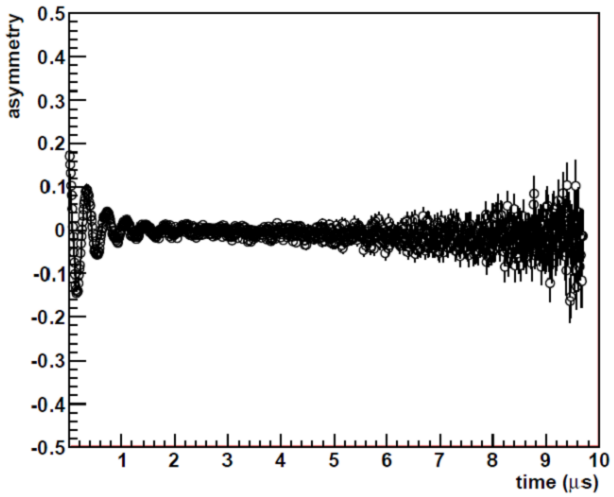

Figure 2.63: Asymmetry versus time at 1.6 K and 200 G, B ∥ {010}

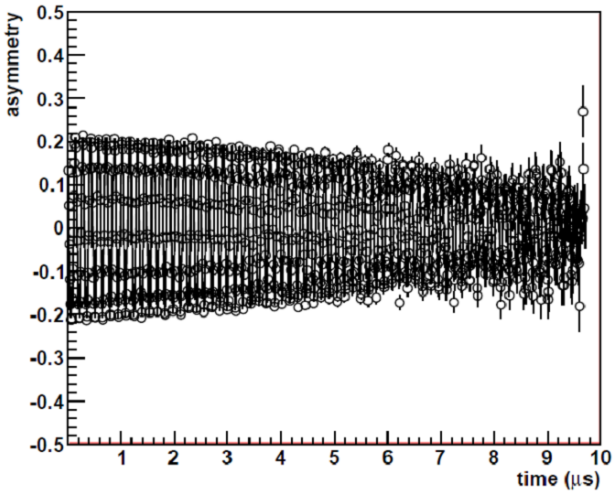

Figure 2.64: Asymmetry versus time at 1.6 K and 500 G, B ∥ {010}

Its characteristic decay time, also called depolarisation rate σ, has a direct link to the penetration depth [77]:

$$\sigma \approx \frac{0.0609\,\gamma_\mu\,\Phi_0}{\lambda^2}$$

where γ_μ is the gyromagnetic ratio of the muon.

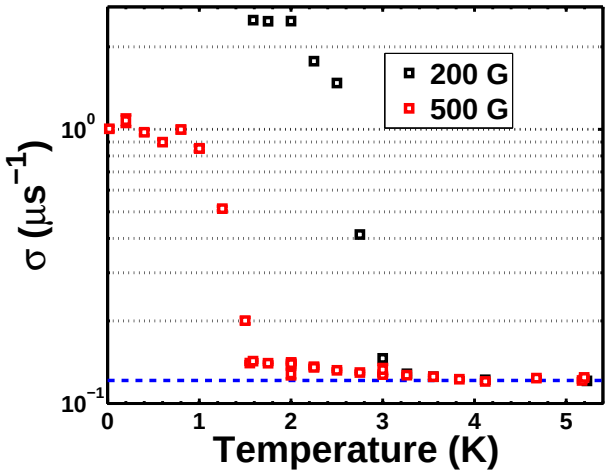

Figure 2.65: Depolarisation rate of BiPd versus temperature for 200 G and 500 G

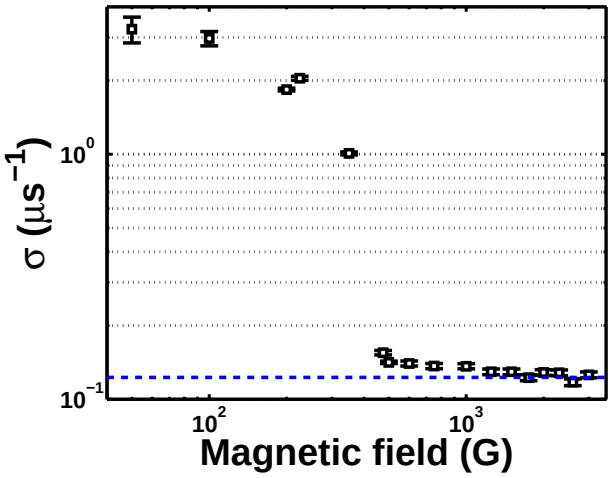

Figure 2.66: Depolarisation rate versus applied field at 1.6 K

Discussion

Figures 2.65 and 2.66 show the variation of σ with temperature and field, indicating that BiPd undergoes a transition from a fast to a slow depolarisation rate. The dotted blue line represents the background signal, caused by the magnetic field of the nuclear spins. The temperatures and field which mark the end of the initial decrease roughly agrees with the previously measured H_{c2} values.

We notice a signal slightly above background remaining after this sharp decrease, slowly decreasing as field or temperature increase. From the σ value, we calculate that this 'thin tail' corresponds to a $\lambda \approx 9000\,\text{Å}$. This is to be compared to the value of the penetration depth at low temperature of 2100 Å for 200 G, and 3300 Å for a field of 500 G.

We originally thought this crossover from a small to large λ to be the sign of multiband superconductivity. However, in light of the proposed enhancement of H_{c2} decribed earlier, we raise the possibility of explaining this behaviour by the fact that the local field distribution probed by μSR near the twin boundaries, being significantly different from the bulk, alters the measured field distribution, resulting in the 'thin tail' observed. Fitting the form factor with such a large value of λ, leaving the other parameter unconstrained, gives us a fitting curve unable to describe the experimental data.

Adding to the confusion, the low-temperature λ values are consistent with tunnel diode oscillations (TDO) carried out by Jiao *et al.* [67]. However, because of the established IMS phase described earlier, we measured the Ginzburg-Landau parameter to be close to 1, leading to an unrealistically high value of the coherence length corresponding to an unphysical $H_{c2} < 100$ G.

Knowing that the tunnel diode oscillation technique is a surface measurement, we argue it measures a larger value of λ due to impurity scattering. As for the value derived from the μSR measurements, the relation linking the depolarisation rate to the penetration depth commonly used (also the one described here) is only valid for high-κ superconductors or very low reduced fields, $\frac{H}{H_{c2}} \ll 1$ [78]. We can then reasonably doubt the resulting value of λ.

2.3.8 Gap symmetry

Many superconductors, for example the emblematic $YBa_2Cu_3O_7$ [79], display a variety of vortex lattice structures in their phase diagram, signs of a complex Fermi surface and gap symmetry. In BiPd, such a behaviour is not observed. Looking at the temperature and field dependence of the q anisotropy (figures 2.67 and 2.68) and the angle between spots (figures 2.69 and 2.70), we can see that there is no significantly large change, meaning there is no noticeable structural transition of the FLL.

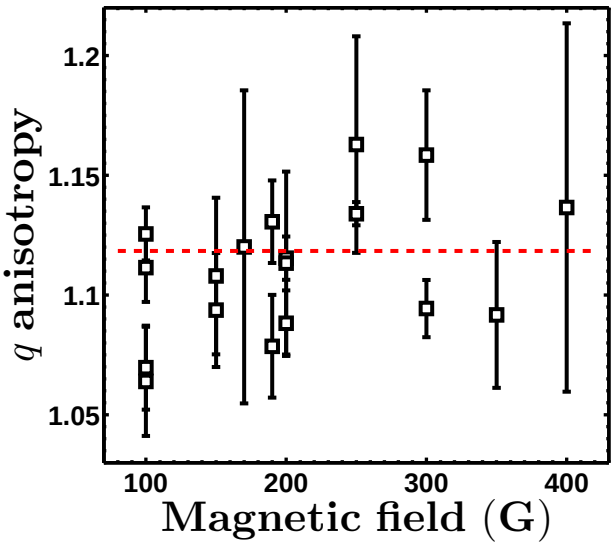

Figure 2.67: Q anisotropy versus B, B ∥ {010}, T = 1.5 K

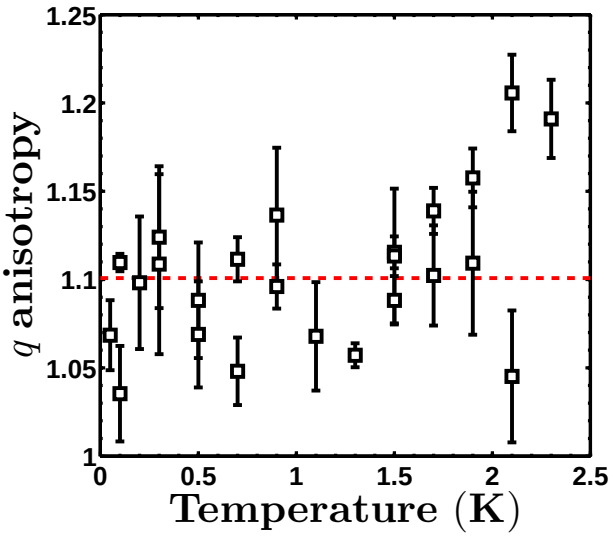

Figure 2.68: Q anisotropy versus T, B ∥ {010}, B = 200 G

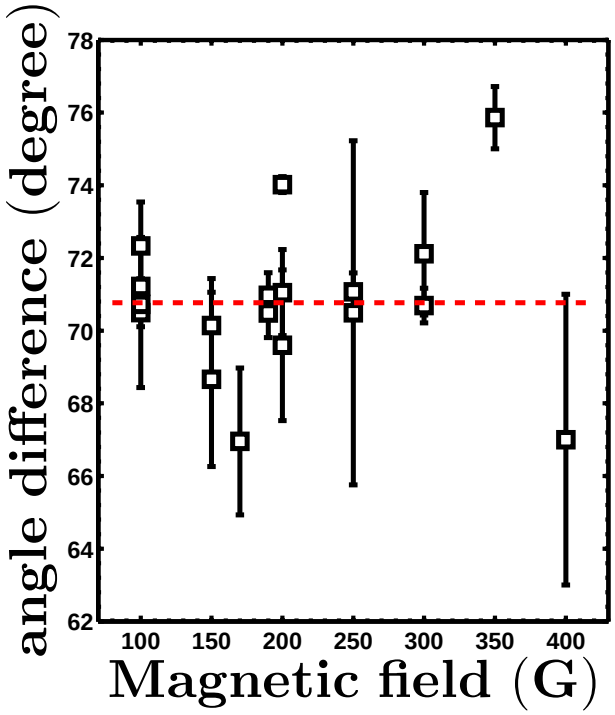

Figure 2.69: FLL angle versus B, B ∥ {010} T = 1.5 K

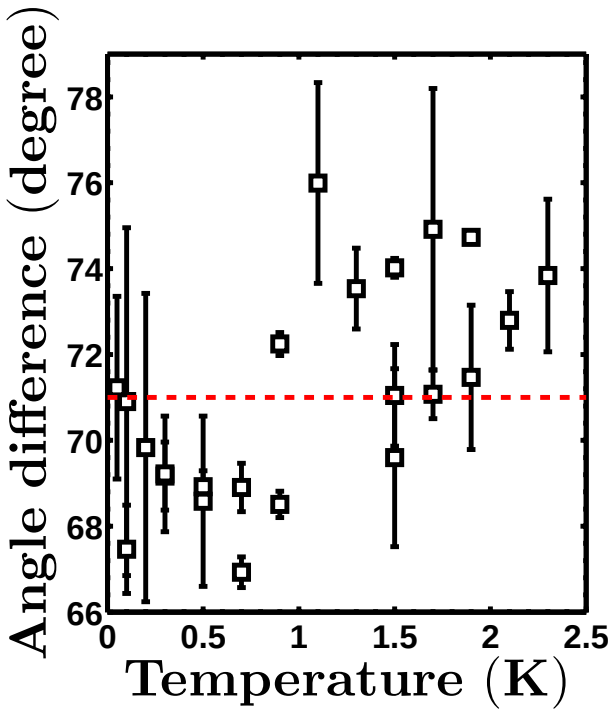

Figure 2.70: FLL angle versus T, B ∥ {010} B = 200 G

This evidence points to a fairly isotropic gap function. It can intuitively be viewed like so: as the field increases, the vortices get closer together. The shape of the core or any anisotropy in ξ will then be reflected on the vortex lattice. BCS theory states [4],

$$\Delta(0) = \frac{\hbar\, v_F}{\pi\, \xi_0}$$

where v_F is the k-dependent Fermi velocity.

This means that the presence of nodes in the gap may be reflected in the k-dependence of ξ, leading to a change in the vortex lattice structure as the inter-vortex distance varies.

When performing SANS experiments, the temperature dependence of the form factor is used [80] to analyse the gap symmetry. As mentioned in section 2.3, a common approximation is $FF \approx \frac{1}{\lambda^2}$. We can transform our experimental form factor data to a normalised variation of the penetration depth, allowing us to exploit the following low temperature approximation, which links the variation of the penetration depth to the magnitude of the gap at 0 K:

$$\frac{\delta\lambda(T)}{\lambda(0)} \approx \sqrt{\frac{\pi\,\Delta(0)}{2\,k_B\,T}}\, e^{\frac{-\Delta(0)}{k_B\,T}}$$

with $\delta\lambda(T) = \lambda(T) - \lambda(T = 0)$. This approximation is valid in the case of a BCS superconductors and assumes $\Delta(T) \approx \Delta(0)$, which is typically the case for conventional superconductors below $T < \frac{T_c}{3}$. Along with this approximation, figure 2.71 shows two other fits characteristic of the variation of the penetration depth in the presence of nodes in clean ($\delta\lambda(T) \propto T$) and dirty ($\delta\lambda(T) \propto T^2$) superconductors [81].

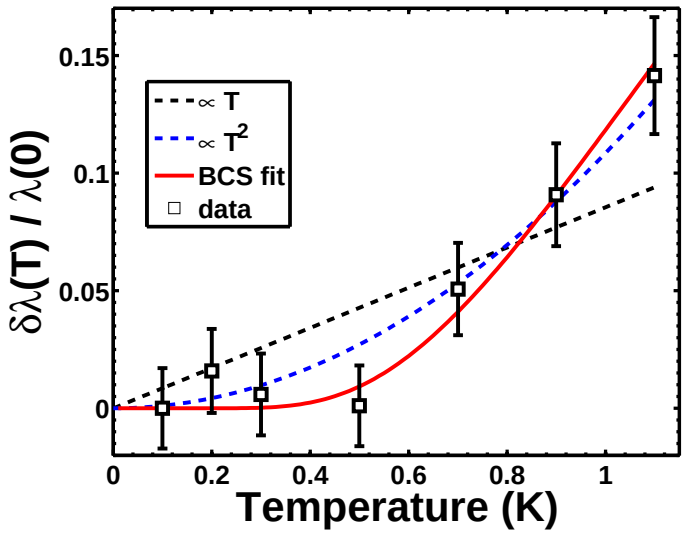

Figure 2.71: Penetration depth $\delta\lambda$ versus temperature, B ∥ {010} and B = 250 G

The resulting gap magnitude for the BCS fits is reported below.

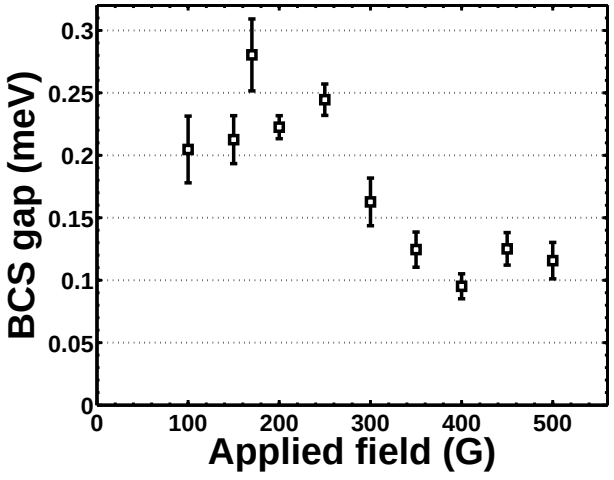

Figure 2.72: Magnitude of the gap in meV versus field for B ∥ {010}

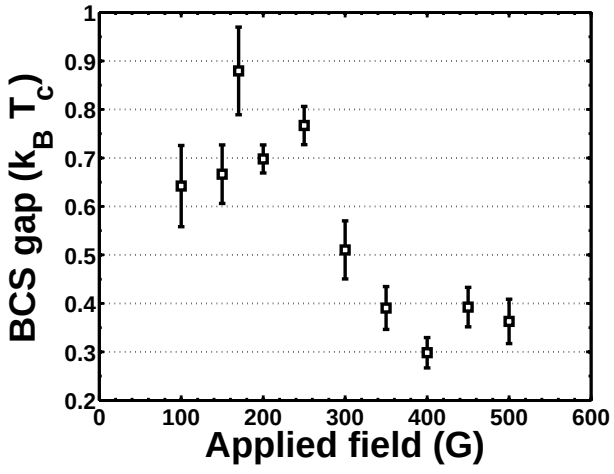

Figure 2.73: Magnitude of the gap in units of $k_B\, T_c$ versus field for B ∥ {010}

Discussion

There is no clear-cut answer when comparing the different models of the variation of the penetration depth because of the size of error bars and the lack of point density, although the BCS fit is the best fit.

Repeating this across all the different fields measured, the results are plotted in figures 2.72 and 2.73. We can see that the gap values are typically much smaller than the 0.5 - 0.6 meV (1.6 - 1.9 $k_B\,T_c$) gap reported in the literature [67] [65]. For comparison, the BCS weak-coupling value is 1.764 $k_B\,T_c$ or 0.56 meV.

We ought to be careful about interpreting the results from this analysis, as we transformed data using the London approximation, necessary to be able to convert the form factor into a penetration depth.

We attribute the large deviations from other experimental values to this reason, but it does not render the analysis useless: both the lack of structural transition with field and temperature and the relative agreement of the data with an isotropic gap fit suggest that the superconductivity in BiPd behaves conventionally. It is to be noted that all orientations show similar behaviour, but the signal extracted from the B $\parallel$ "{100}" and {101} experiments mixes in-plane (λ_{ac}) and out-of-plane (λ_b) contributions.

Discarding the absolute value of the gap, we can still conclude from the data that, if BiPd along {010} can be described by BCS theory, there is a clear suppression of the gap value with increasing field.

This stems from the fact that as the magnetic field goes up, the superfluid will be imparted more and more kinetic energy, subsequently needing less and less energy to depair, yielding an observed suppression of the gap magnitude with increasing field.

2.4 Conclusion

We carried out numerous experiments to map the superconducting phase diagram of BiPd, unveiling in the process an enhancement of the upper critical field, proposed to be caused by the altered superconductivity near twin boundaries in NCS superconductors. Due to the bulk nature of the SANS measurements, we argue that the value of H_{c2} we find, although not accurately measured, is the best value characterising the bulk behaviour of BiPd reported so far.

We have uncovered a rare behaviour in the landscape of superconductors, displayed by low-κ materials, the Intermediate Mixed State. This is a phase characterised by islands of constant-spacing vortex lattice surrounded by Meissner domains, whose volume vary as field changes.

While the complete extent of this phase remains unknown due to the quality of the measurements, we provided strong proof of its existence in the low fields and low temperature part of the superconducting phase of BiPd.

Measuring the correlation length characterising the FLL, we showed that, even though the intensity of the signal fades as field and temperature increase, the vortex lattice quality actually improves.

Fitting the variation of the form factor with field, we determined for the first time sensible values of the superconducting parameters λ and ξ. The value of these parameters is consistent with the presence of an IMS, a strong indication that BiPd is a low-κ material.

Our findings are consistent with the previously reported results that the superconductivity in BiPd behaves conventionally, with an order parameter governed by a BCS isotropic gap [65].

Orientation	$\boldsymbol{H_{c2}(0)}$	$\boldsymbol{H_{IMS}(0)}$	$\boldsymbol{\lambda(0)}$	$\boldsymbol{\xi(0)}$	$\boldsymbol{\kappa}$
B ∥ {010}	650 Å	225 Å	750 Å	710 Å	1.06
B ∥ {101}	700 Å	190 Å	820 Å	690 Å	1.19

Table 2.10: Summary of the results

However, TDO [67] and PCAR measurements [82] find two gaps, a scenario compatible with the two-component order parameter picture described in section 2.1. This is in contrast to STM measurements [65] which failed to see evidence of any spin-triplet component. NMR measurements report a suppressed height of the coherence peak of BiPd, possibly due to the presence of a spin-triplet component, but fail to see the signature of a second gap.

In summary, there is still conflicting evidence of the subject and the gap symmetry of BiPd is not uncontestably determined.

CHAPTER 3

Nb_3Sn

3.1 Motivation

Superconducting materials are commonly used in devices where a large current is required, for example to generate large magnetic fields such as nuclear magnetic resonance machines, large scale experiments (ITER, CERN) or in cryomagnets for a large number of condensed matter experiments (including the study of superconductors themselves, for example in the Birmingham 17 Tesla magnet [83]).

Apart from the critical temperature and fields described in the introductory chapter, another relevant parameter limits the superconducting domain: there is a maximum current density J_c above which the superconductivity is destroyed, as the moving charges would create too large a magnetic field. Vortex pinning plays a large role in its determination, as unpinned vortices cause energy dissipation when subjected to a sufficiently large driving force (i.e. a current), which generates a temperature increase, in turn causing a decrease in superfluid density, which lowers J_c, forming a vicious cycle destroying the superconducting state.

Increasing J_c is an important technological goal [84]. Nb_3Sn, discovered in 1954 by Matthias *et al.* [85], is one of the most widely used superconductors for these purposes.

The binary phase diagram of the $Nb_{1-\beta}Sn_\beta$ system is complex (see figure 3.1), and the region of interest is the tin doping range $\beta \sim$18-25 %, as both the neighbouring compounds Nb_6Sn_5 and $NbSn_2$ have critical temperatures below 3 Kelvin [86]. The relatively high T_c of Nb_3Sn is due to its A15 unit cell (figure 3.2), containing niobium chains comprised of closely separated atoms, at the origin of an enhancement of the DoS at the Fermi level [87].

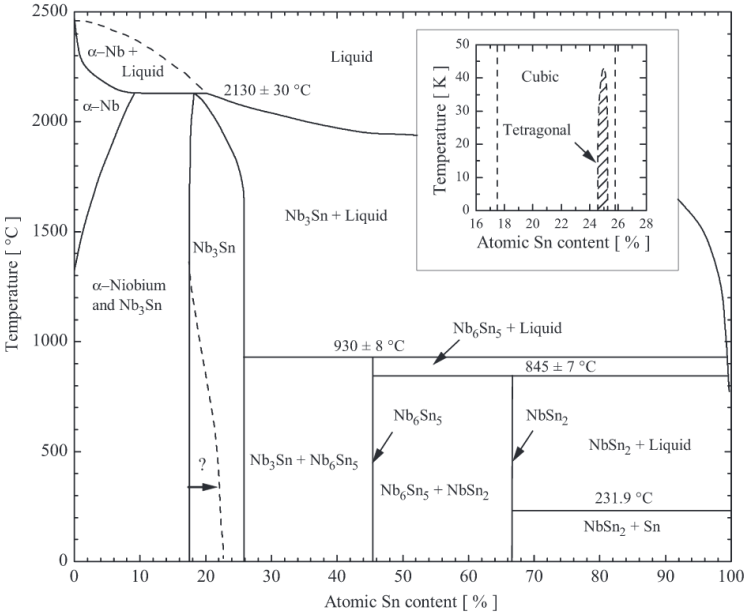

Figure 3.1: Phase diagram of the Nb-Sn alloy. From Godeke [86]

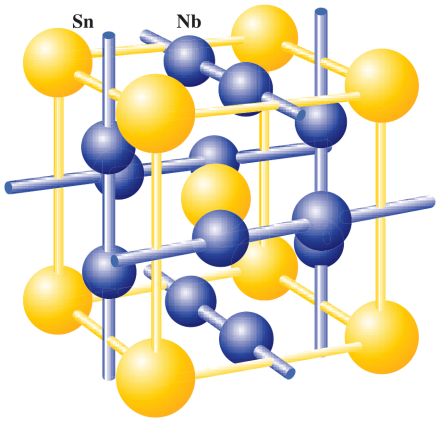

Figure 3.2: A15 unit cell of Nb_3Sn. From Godeke [86]

In the β ~18-25 % region, as tin doping increases, H_{c2} rises with β and suddenly falls above $\beta \approx 24.5$ atomic % (figure 3.3). This drop is associated with the appearance of a structural (martensitic [88]) transition T_M above T_c ($T_c \approx 18$ K and $T_M > 31$ K for $\beta > 0.245$), turning the crystal structure from cubic to tetragonal as temperature decreases, as shown in figure 3.4.

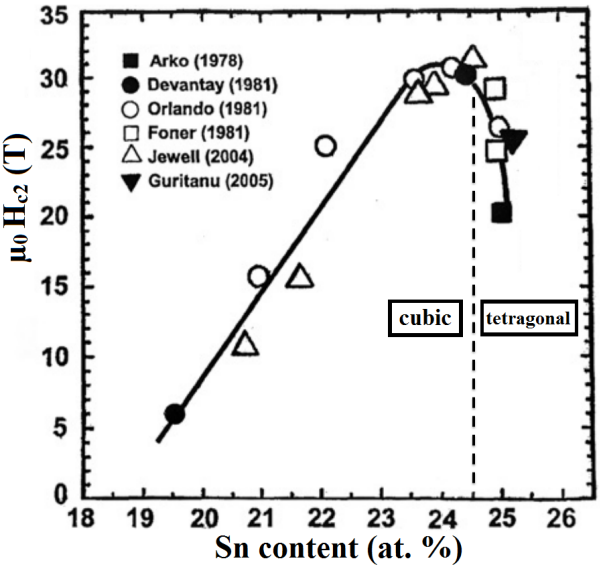

Figure 3.3: Second critical field versus Sn content. Adapted from Flükiger *et al.* [89]

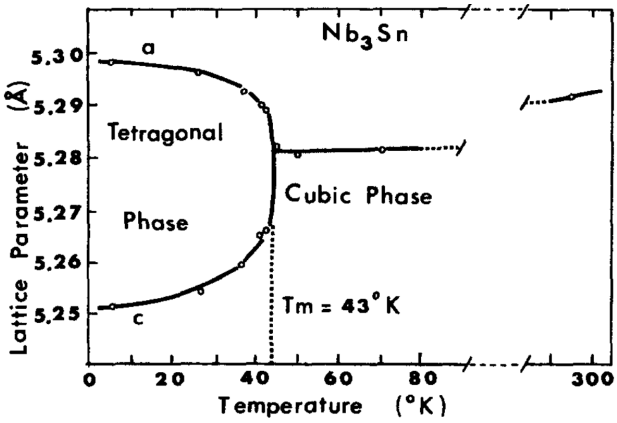

Figure 3.4: Lattice parameters versus temperature. From Mailfert *et al.* [90]

Zhou *et al.* [91] were able to suppress the transition in samples of varying tin content by using Hot Isostatic Pressing (HIP) processes at different temperatures, as seen in the change of X-ray diffraction (XRD) structural peaks in figure 3.5. The authors found no influence of the crystal structure on H_{c2} (figure 3.6) and consider the previously observed differences in H_{c2} to be caused by the fact that the measurements were performed on samples with different shapes (thin films, single and polycrystals).

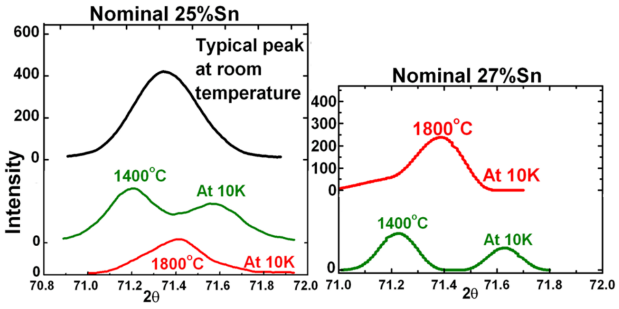

Figure 3.5: Structural peaks for different HIP treatments, from Zhou *et al.* [91]

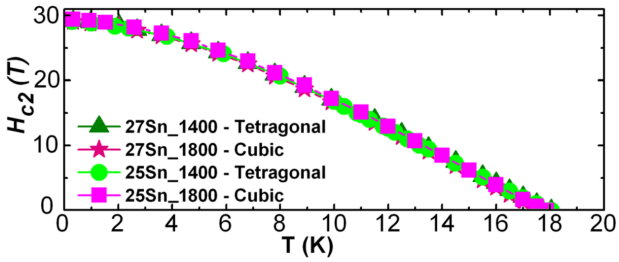

Figure 3.6: Resistivity measurements showing the same $H_{c2}(T)$ for different samples, described in the text. From Zhou *et al.* [91]

This absence of H_{c2} variation warranted further study of the superconducting state in Nb_3Sn and an experiment was conducted on four samples described in table 3.1. These samples were prepared by the same methods as in Ref. [91], by the same group.

name	**nominal Sn content (at. %)**	**measured Sn (at. %)**	**annealing temp. (°C)**	**structure**
sample 1	27	24.6 ± 0.2	1400	tetragonal
sample 2	27	23.7 ± 0.4	1800	cubic
sample 3	25	24.6 ± 0.3	1400	tetragonal
sample 4	25	23.3 ± 0.7	1800	tetr. (target=cubic)

Table 3.1: Comparison of the different Nb_3Sn samples studied. Despite having the same heat treatment as sample 2, sample 4 was found to have tetragonal symmetry.

The samples are polycrystalline, in the shape of cubes of edge length ∼5 mm , pictured in figure 3.8. We scanned the phase diagram up to 7 Tesla and 18 K (figure 3.7). Preliminary measurements indicate all four samples to have $T_c \approx 18$ K and $H_{c2}(0.3\,K) \sim 29$ T.

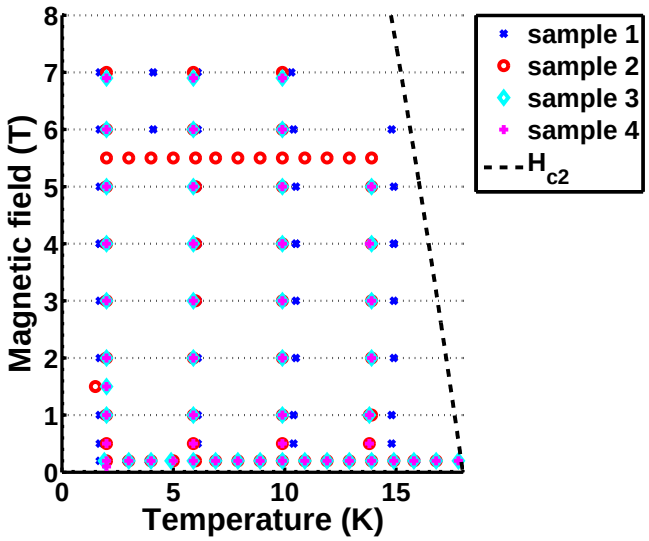

Figure 3.7: Summary of scans carried out at ILL. The dotted line represents the phenomenological law $H_{c2}(T) = H_{c2}(0)(1 - \frac{T}{T_c})^2)$

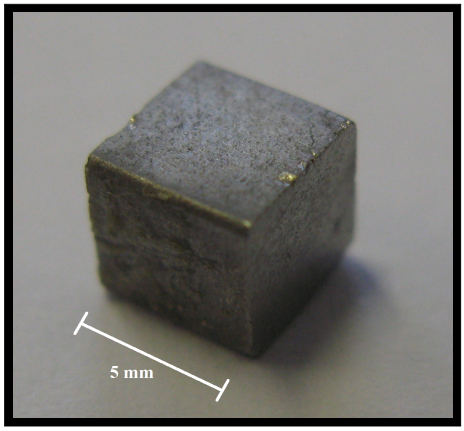

Figure 3.8: Sample of Nb_3Sn

The experiments were carried out at the Institut Laue-Langevin using D33. Depending on the applied magnetic fied, three different detector distances were used (table 3.2). All the measurements were done using a neutron wavelength of 12 angströms and using the field cool procedure explained in the previous chapter.

Field range (T)	**sample-detector distance (m)**
0.2, 0.5	12.8
1 - 4	5
5 - 7	3

Table 3.2: Experimental configuration

3.2 Data analysis

In the range of applied fields, the inter-vortex spacings goes from approximately 16 to 100 nm. Comparing this with the typical grain size $> 1\,\mu m$ (which depends on the heat treatment temperature [92]), we see that each grain contains many vortices. The samples being polycrystals, the detected diffraction pattern is the result of the vortex lattice implanted in many grains with different crystal orientations and a diffraction ring appears, as seen in figure 3.9. Unlike single crystal diffraction, it is not possible to isolate diffraction spots, as they are all distributed along the diffraction ring. This warrants a different analysis approach which we describe below.

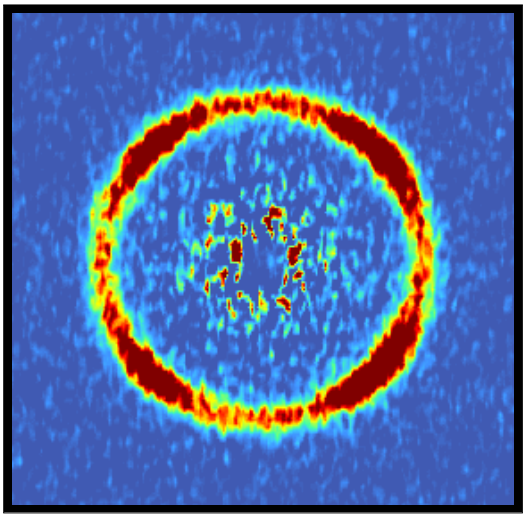

Figure 3.9: Diffraction pattern assembled from vertical and horizontal rocks of sample 1 for B = 2 T and T = 1.7 K

We plot the scattering vector versus field in figure 3.10. We see that the q-value varies with field, but the extent of the variation is not clearly visible. One way to remedy to this is to calculate a *normalised* q-value :

$$q_{norm} = \frac{q - q_{square}}{q_{hex} - q_{square}}$$

which reflects the evolution of the scattering vector without the scale due to the different applied fields, resulting in :

$$\begin{cases} q_{norm}(q = q_{hex}) = 1 \\ q_{norm}(q = q_{square}) = 0 \end{cases}$$

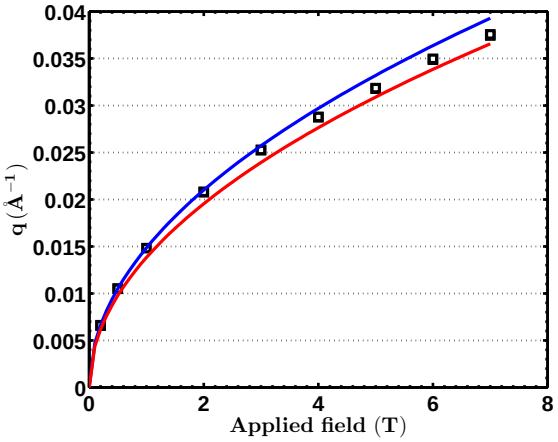

Figure 3.10: Average scattering vector versus applied field for sample 1 at 1.7 K

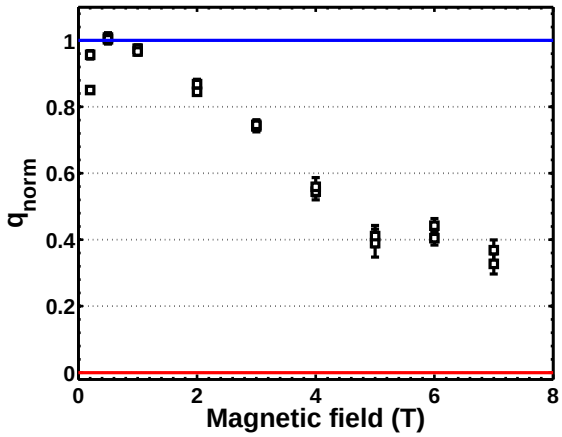

Figure 3.11: Normalised q versus field (sample 1, 1.7K)

Another way of visualising the data is to think in terms of the effect of the crystal lattice on the FLL. Setting aside the (not easily quantifiable) Fermi surface effects and adopting a purely geometrical view, we can see that if the field is aligned along the $\{1\,1\,1\}$ plane family, the FLL 'sees' an underlying lattice with a 6-fold symmetry and therefore (within this crude approximation) would tend to arrange itself into a hexagonal lattice.

As figure 3.11 shows, the field changes the amount of hexagonal vortex lattice. This can be modelled by saying that a given amount of hexagonal FLL (indicated by q_{norm}) corresponds to a the solid angle occupied by cones of opening angle θ_{OA} (see figure 3.12) :

$$q_{norm} = \frac{8\,(1-\cos\theta_{\mathrm{OA}})\,2\,\pi}{4\,\pi} \quad \text{leading to} \quad \theta_{\mathrm{OA}} = \mathrm{acos}(1-\frac{q_{norm}}{4})$$

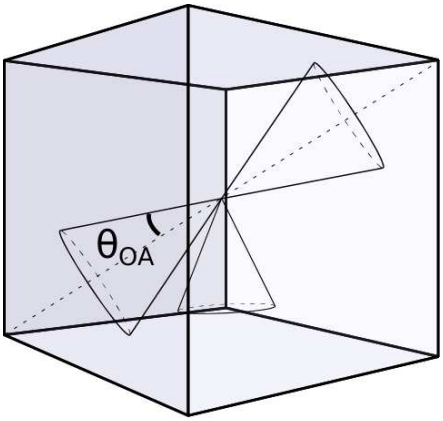

Figure 3.12: Diagram illustrating the solid angle cones oriented towards the unit cell vertices, characterising the opening angle θ_{OA}.

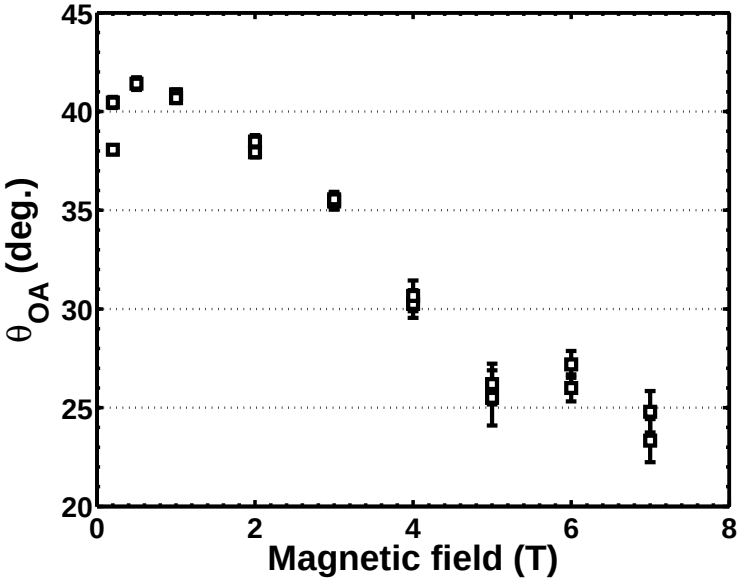

Figure 3.13: Opening angle versus field (sample 1, T = 1.7 K)

Both figures 3.11 and 3.13 show a decrease of the proportion of hexagonal vortex lattice as the applied field increases. This can be compared to the data of Kadono *et al.* [93], who observe a crossover from hexagonal FLL at low fields to a square VL at higher fields in a single crystal with $\mathbf{H} \parallel \{0\,0\,1\}$, as pictured in figure 3.14.

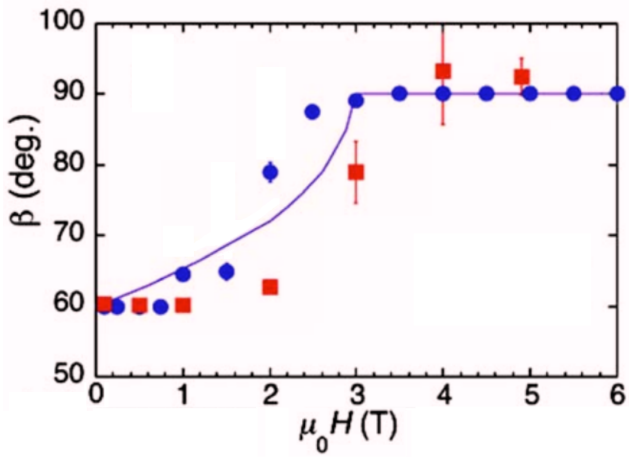

Figure 3.14: Apex angle of the vortex lattice in a single crystal of Nb_3Sn (see text). The blue points represent data extracted from μSR fits (real space), red from SANS. From Kadono *et al.* [93]

The q-values used are obtained by fitting the diffraction rings by a Gaussian function in the detector plane and recording the peak values. We see that contrary to the single crystal data, in the range of applied fields it never reaches the value corresponding to a square FLL. In the same fashion as q_{norm}, we can construct a

model that treats the variance/FWHM/radial width of the signal as a weighted average of q_{hex} and q_{square}:

$$\sigma^2 = q_{norm}\,(q_{hex} - q)^2 + (1 - q_{norm})\,(q_{square} - q)^2 = (q - q_{square})\,(q_{hex} - q)$$

$$\text{FWHM} = \sqrt{(q - q_{square})\,(q_{hex} - q)\,8\,\ln 2} + W_{int}$$

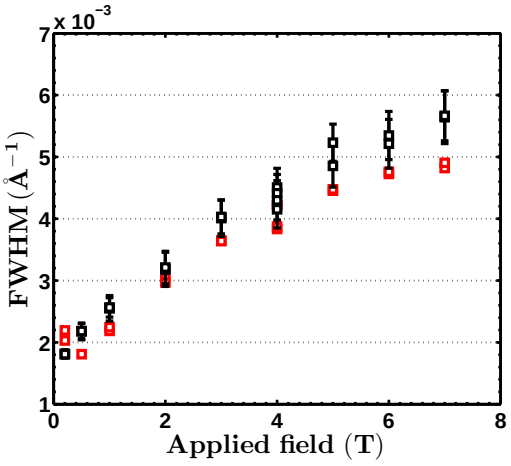

Figure 3.15: Experimental FWHM (black) and modelled FWHM (red) versus applied field (see text)

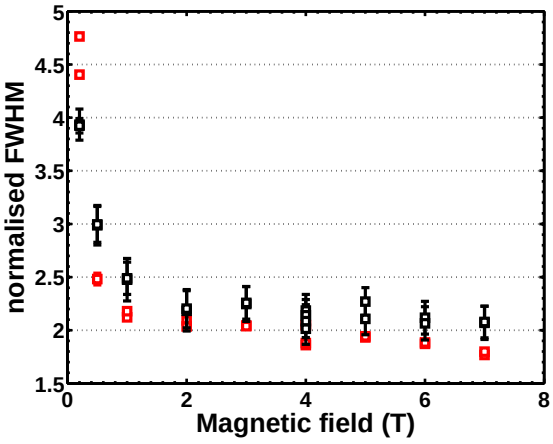

Figure 3.16: Normalised width of the diffraction ring (see text) versus field (sample 1, T = 1.7 K)

The data is corrected for the instrumental resolution (see section 2.3):

$$FWHM_{reported} = \sqrt{FWHM^2_{measured} - FWHM^2_{inst.}}$$

We add a constant W_{int} term to account for the intrinsic width of the signal at low fields, taken as the experimental value. Figure 3.16 shows the width of the diffraction ring normalised by $(q_{hex} - q_{square})$. The model indicates a maximum width for $q = \frac{q_{hex} - q_{square}}{2}$ or $q_{norm} = 0.5$, which corresponds to $B \approx 4$ T and subsequently decreases as more FLL adopt a square geometry.

Interpreting the results is difficult due to the spread of the data, but the graphs seem to show a relative agreement to the model until ~ 4 T. The data seems to indicate that while the peak q-value shifts towards the square value with increasing field, the relative width of the distribution of q-values remains unchanged above 4 T, possibly an indication of field inhomogeneity or non-local effects affecting the vortex lattice. One also has to keep in mind that the FLL might display a distorted hexagonal structure, a possibility that is neglected in this approach.

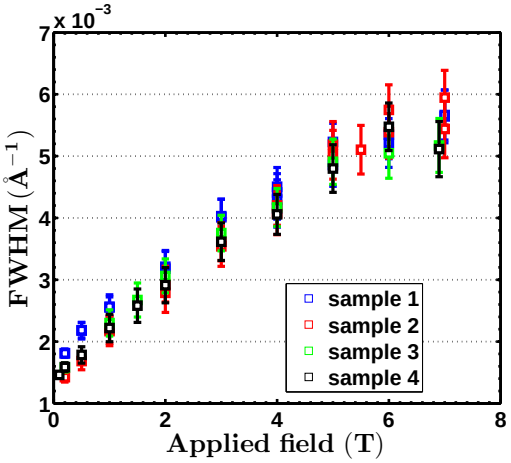

Figure 3.17: Diffraction ring width versus applied field for all samples (T = 1.7 K)

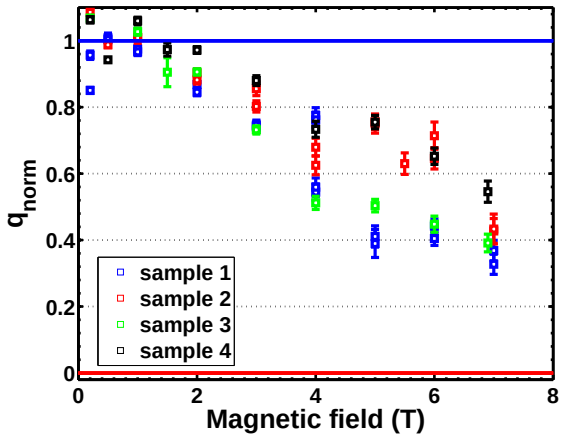

Figure 3.18: Normalised q versus applied field for all samples (T = 1.7 K)

Figures 3.17 and 3.18 compare the FWHM and normalised q-values of all samples to each other. We see that the FWHM does not significantly differ from sample to sample, but that there is a change in behaviour between samples (2,4) and samples (1,3) in the 3-7 Tesla region. Sample 2 was annealed at 1800 °C to retain a cubic crystal lattice. Sample 4, despite being subjected to the same treatment, was found to still undergo the martensitic transition.

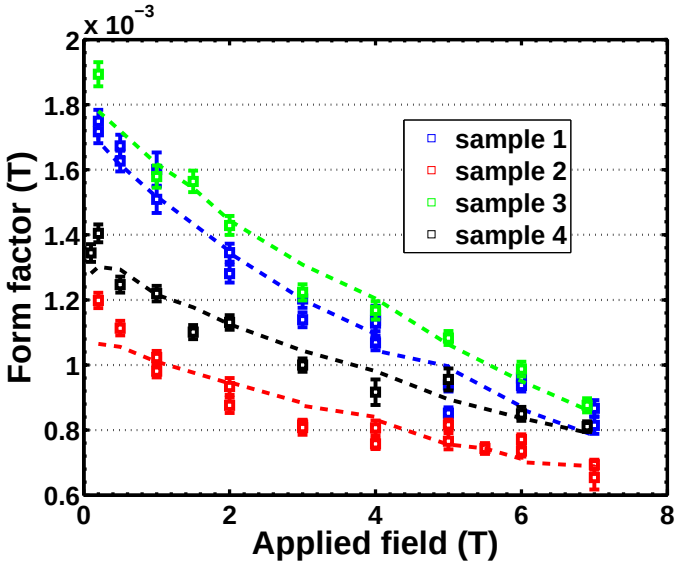

Figure 3.19: Form factor versus applied field for all samples at T = 1.7 K. The dotted lines represent the fits, described in the text.

Extracting the form factor proved to be a more delicate endeavour. Because of the polycrystalline nature

of the samples, the diffracted intensity is distributed around the entire diffraction ring. Delimiting an area around a particular diffraction spot is no longer possible, so an arbitrary sector was set with a 45 degrees azimuthal width centred on the rocking direction. We correct the intensity by the following terms:

$$I_{\text{eff}} = I_{\text{measured}} \left[q_{norm} \frac{45}{60} + (1 - q_{norm}) \frac{45}{90} \right] = I_{\text{measured}} \left[\frac{q_{norm}}{4} + \frac{1}{2} \right]$$

$$\cos \zeta_{lor} = \frac{\cos 0 + \cos 45/2}{2} \approx 0.76$$

These corrections characterise the (varying) amount of square FLL and the average Lorentz factor. In their single crystal experiment, Kadono *et al.* [93] use the following form factor expression:

$$FF = \frac{B\, e^{-q^2 \xi^2}}{1 + q^2 \lambda^2 + \alpha(q^4) \lambda^4}$$

where $\alpha(q^4)$ is a parameter which depends on the details of the Fermi surface, detailed by Kogan *et al.* [94]. However, because our signal is essentially a mixture of all directions in space, it does not make sense for us to use the values of α they find and we opt to use the simple isotropic model ($\alpha = 0$).

Figure 3.19 shows that there is a striking difference between samples, with the emergence of the two previously identified groups.

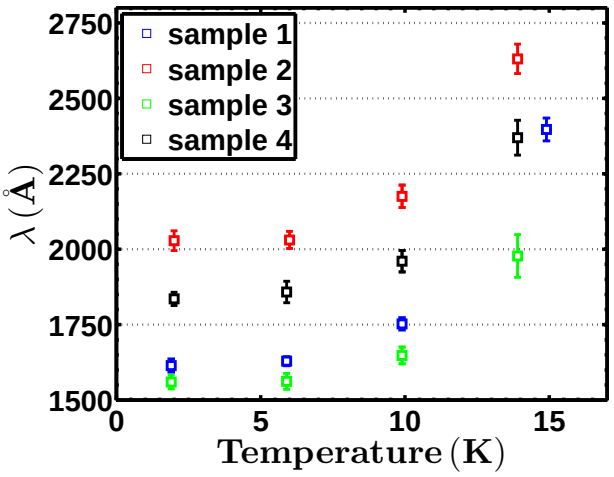

Figure 3.20: Penetration depth versus temperature for the four Nb_3Sn samples

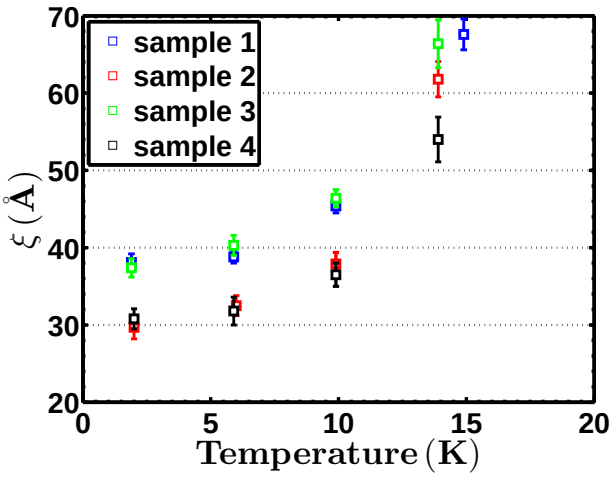

Figure 3.21: Coherence length versus temperature

The isotropic model sensibly fits the data; this separation is reflected in both in the penetration depth (figure 3.20) and the coherence length (figure 3.21).

The next step is to analyse the temperature dependence of the data. Figures 3.22 and 3.23 show the q-value

and the radial width of the signal as a function of temperature. The vertical shift of sample 1 data (blue) is not seen at different applied fields. Because it corresponds only to a 4% field difference (at 0.2 T, this is a shift of 80 G), it is reasonable to assume that is caused by trapped field inside the cryomagnet or another type of systematic error.

We clearly see that both graphs do not present any significant variation, a behaviour that is suggesting that no vortex lattice transition is taking place when varying temperature.

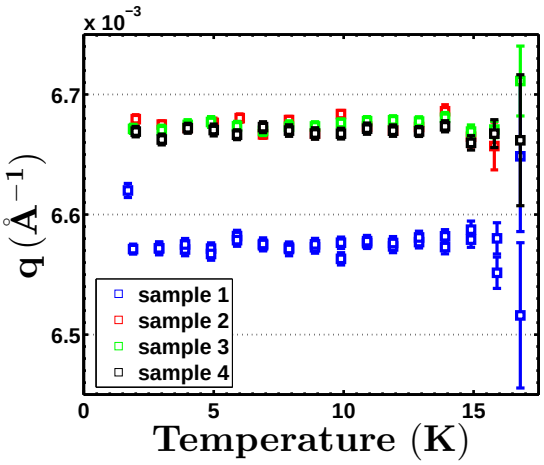

Figure 3.22: Scattering vector norm versus temperature at B = 0.2 T

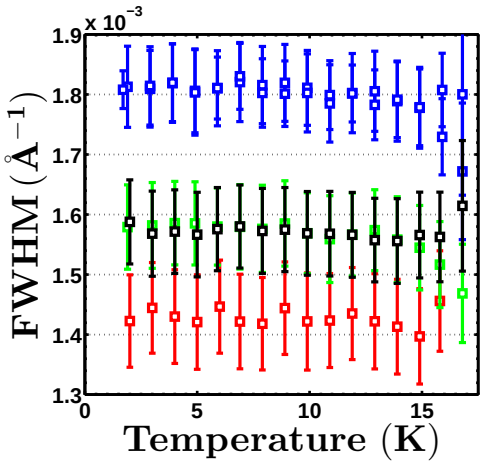

Figure 3.23: FWHM (corrected for instrumental resolution) versus temperature at B = 0.2 T)

In order to analyse the temperature dependence of the form factor, a commonly used approach (e.g. see Furukawa *et al.* [95]) is to calculate both $\lambda(T)$ and $\xi(T)$ by proxy, evaluating the following quantities:

$$\frac{1}{\lambda(T)^2} = \rho(T) = 1 - \frac{1}{2\,k_B\,T}\int_0^\infty \cosh^{-2}\left(\frac{\sqrt{\epsilon^2+\Delta(T)^2}}{2\,k_B\,T}\right)d\epsilon$$

$$\text{and} \quad \frac{1}{\xi(T)} \propto \Delta(T) = \Delta_0\,\tanh\left(1.78\sqrt{(\frac{T_c}{T}-1)}\right)$$

Figures 3.24 shows the different temperature dependences of the form factor curves for all samples. As for figure 3.19, the same sample groups appear. The resulting gap values extracted are represented in figure 3.25 and will be discussed below.

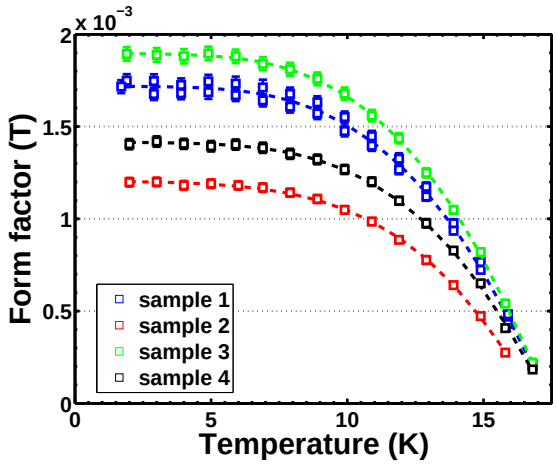

Figure 3.24: Form factor versus temperature for all Nb_3Sn samples (B = 0.2 T). The dotted lines represent the fits.

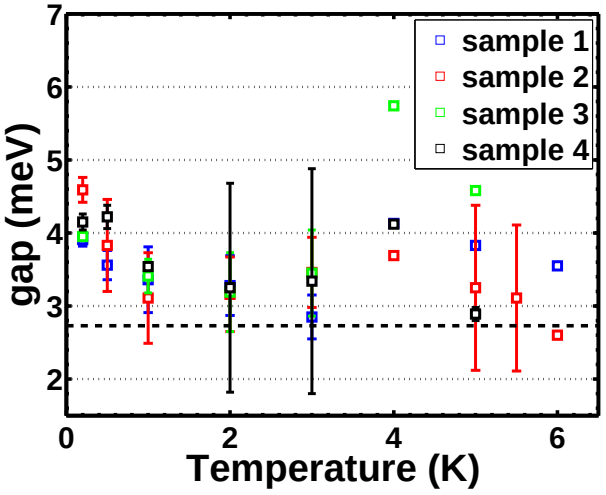

Figure 3.25: Superconducting gap values versus magnetic field, extracted from form factor temperature dependence. The dotted line represents the BCS gap value, and the points with no visible error bars have an uncertainty > 2 meV.

3.3 Discussion and conclusion

As previously stated, we notice a clear separation between sample (1,3) and (2,4) when looking at the different experimental quantities extracted from the data. Figure 3.26 shows the original graph from which stems this investigation, on which we superimpose the B_{c2} values that should have been measured should the proposed (although empirical) relationship linking Sn % to B_{c2} hold.

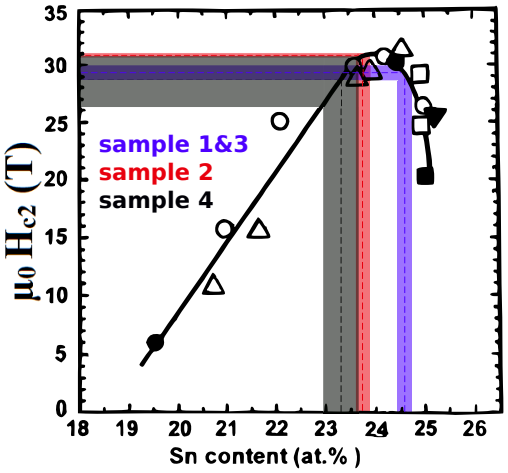

Figure 3.26: Predicted range of B_{c2} from measured spread of Sn content. Adapted from Flükiger *et al.* [89]

Tin content was determined using energy dispersive X-ray spectrosocopy (EDS), a surface-sensitive technique, which means that the accuracy of the reported value depends on the homogeneity of the sample. Growing Nb_3Sn samples is associated with an inherent spread in tin concentrations (see figures 3.27 and 3.28): the strength of this study lies in the fact that all samples have the same geometry and were grown and processed in a similar way.

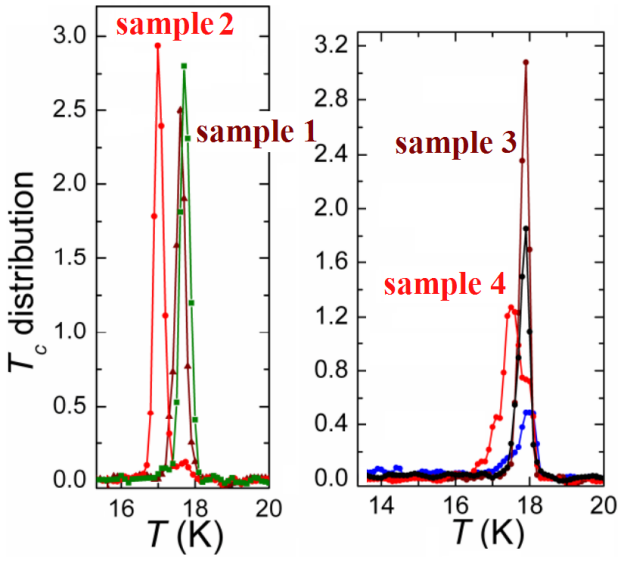

Figure 3.27: Probability density function of T_c obtained from deconvolution of heat capacity measurements. Adapted from J. Zhou [96]

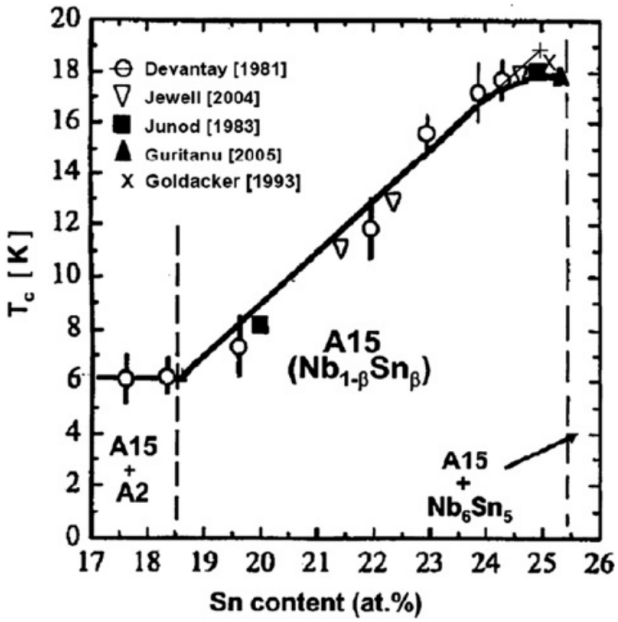

Figure 3.28: Critical temperature as a function of tin content, from Flükiger *et al.* [89]

With these limitations in mind, we see that by converting the values of the coherence length in B_{c2} (figure 3.29), the predicted $B_{c2}(0)$ differ significantly from the previously measured $B_{c2}(0.3\,K) \sim 29$ T, with values approximately of 24 T for samples (1,3) and 36 T for samples (2,4).

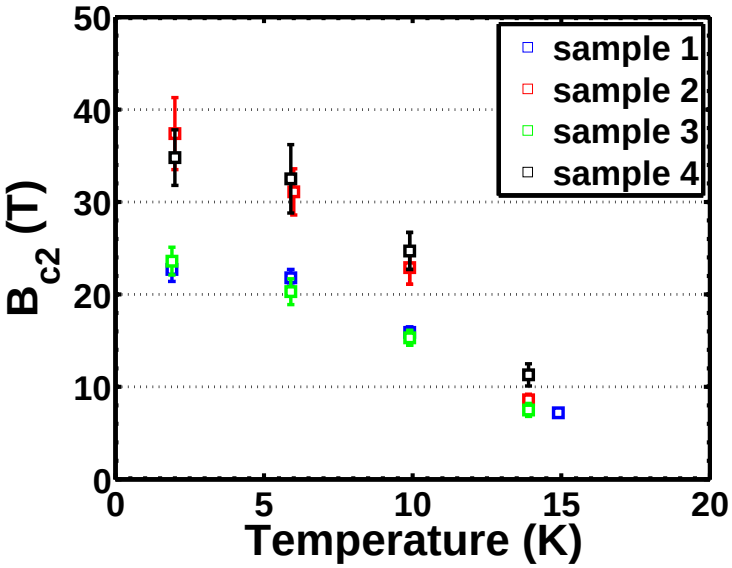

Figure 3.29: Second critical field versus temperature for all Nb_3Sn samples.

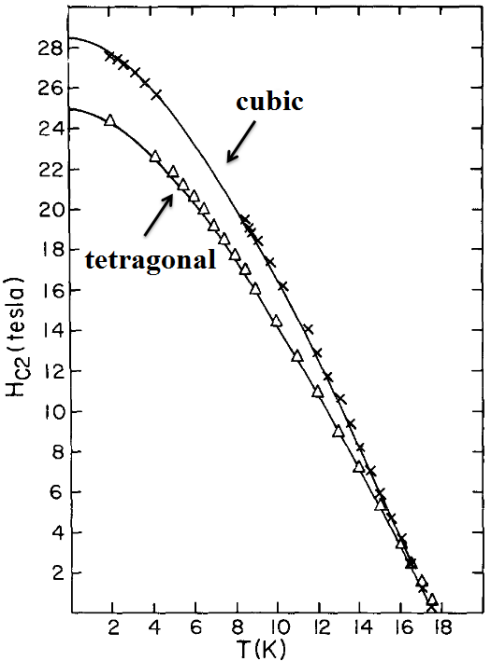

Figure 3.30: H_{c2} versus temperature for polycrystalline Nb_3Sn samples, adapted from Foner *et al.* [97].

This is in clear contradiction with the results that started this investigation, and in agreement with earlier results which support the fact that the martensitic transition does influence the value of H_{c2}, as seen on figure 3.30. While the absolute values of the critical field might be questioned (i.e. there is a large unexplained difference between the experimental values reported of figures 3.26, 3.30 and our values), we argue the difference between groups of samples may not.

The observed lack of differentiation could be caused by the H_{c2} measurement being extracted from resistivity curves (90% point), which only probe the best part of the samples. The intrinsic inhomogeneity previously mentioned may be at the origin of this observation.

Table 3.3 summarises the observations made for the two groups of sample:

samples	**target structure**	$\mathbf{H_{c2}(0)}$ **(measured here)**	$\mathbf{H_{c2}(0)}$ **(literature)**	$\lambda(\mathbf{0})$	**FLL**
1&3	tetragonal	∼24 T	∼25 T	∼ 1600 Å	less hex. at high fields
2&4	cubic	∼36 T	∼28.5 T	∼ 1900 Å	more hex. at high fields

Table 3.3: Comparison of observations for the two groups of samples

We see that in addition of a change in H_{c2} between the two groups, there is also an increase of the penetration depth when the martensitic transition is suppressed, corresponding to a decrease of H_{c1}. Both

these effects could be realised if a significant mean free path reduction takes place between the cubic and tetragonal samples (see section 1.1). All samples have RRR in the ∼2-5 range, placing them in the dirty limit, but looking at the values (detailed in Ref. [91]) provides no basis for classifying the samples in groups. It is worth noting that our values of λ are more than twice the values found by Kadono *et al.* [93] in their single crystal. This large difference remains unexplained.

Another troubling fact is that despite the EDS and structural peak of sample 4 indicating it has a tetragonal symmetry, its measurements distinctly classify it in the second group. This is another manifestation of the inhomogeneity associated with the sample-growing process.

The increase of λ can be either caused by an increase in effective electron mass, an effect which to our knowledge has not been reported in the literature, or a decrease in superfluid density. Interestingly, Escudero *et al.* [98] [99] reported point-contact spectroscopy and specific-heat measurement supporting the appearance of a charge density wave gap in Nb_3Sn samples presenting a martensitic transition. If real, this effect would cause an increase of λ in tetragonal samples, but we precisely observe the opposite behaviour.

Nb_3Sn has been separately argued to possess an anisotropic [100], two [101] or a single [102] gap. Our data have excellent agreement with single (full) gap fits of approximately 4 meV. This is slightly larger than the most recent value of 3.7 meV measured by Jo *et al.* [102] using heat capacity.

We also notice that the gap value does not vary between sample groups. By virtue of the BCS formula (see Annett [103]):

$$\xi = \frac{\hbar\, v_F}{\pi\, \Delta_0},$$

and by considering that the penetration depth as well as the behaviour of the FLL at high field change between groups, we can deduce that the superconducting state in Nb_3Sn is under the influence of non-local/Fermi surface effects.

CHAPTER 4

CONCLUSIONS AND FURTHER WORK

BiPd

As previously outlined, BiPd is only one example of a non-centrosymmetric superconductor. Theoretically, the lack of centrosymmetry is expected to lead to multiple exotic properties, and there is indeed already a wide variety of observed phenomenons in NCS superconductors in the literature (see Bauer *et al.* [53]). A few materials (e.g. $LaNiC_2$) have been reported to display non-conventional behaviour [104].

In this thesis, we studied the flux line lattice of BiPd, mapping its temperature-magnetic field phase diagram and uncovering the presence of an Intermediate Mixed State, only seen in a few superconducting materials so far. This investigation of the vortex lattice, a novel study in itself, also allowed us to determine various quantities describing the superconducting state of BiPd. Our results support the conclusion that, despite the strong spin-orbit scattering, BiPd shows no evidence of mixture of spin singlet and triplet pairing channels, possibly due to the fact that the order parameters associated with the Fermi surface splitting are of the same sign or near equal [54]. Other experimental work also points to this [105].

Another possible avenue to explore would be the recent development of the Dark Field Imaging technique by Reimann *et al.* [106], which would allow us to study the IMS and vortex lattice distribution of BiPd in a more direct way (i.e. in real space) and compare them with the results presented here. For example, probing the limits of the IMS in field and temperature would be a good addition to the results shown in this thesis.

Nb_3Sn

Creating superconducting wires with optimal properties using Nb_3Sn is a balancing act between its intrinsic characteristics (associated with the superconducting properties of the A15 phase) and extrinsic properties (e.g. minimising the composition gradient, maximising the grain boundary density ...) [107].

This analysis characterises the vortex lattice in several polycrystalline Nb_3Sn samples, and shows that recent findings concerning the variations of H_{c2} with the presence or absence of structural transition are unlikely to be a bulk effect. In addition, our results are consistent with a fully gapped Nb_3Sn, although with inherent limitations.

The fundamental study of the vortex lattice in Nb_3Sn would be best undertaken using single crystals, as currently all directional information is lost because of the polycrystalline nature of the samples. Determining the gap symmetry in more details, which is still controversial at the time this thesis is written, as well as a more precise study of the variation of the vortex lattice structure with different tin concentrations, would for example both require single crystals. However, we would then lose the connection to the commercial preparation technique.

We also note that the question of the decrease of H_{c2} still has not been settled, mostly because of the inherent inhomogeneity of the materials. Apart from creating samples with a narrower tin doping range, which, to the extent of our knowledge does not seem possible with the existing sample-growing techniques, it would be interesting to look at the distribution of upper critical fields inside the material [108] and characterise its relationship with the range of tin content in order to better understand this system.

APPENDIX A

BRIEF DESCRIPTION OF THE FITTING ALGORITHM

In this thesis, we use a non-linear fitting algorithm to fit the models to the data. Given a set of parameters $\boldsymbol{\beta}$ the model curve $f(x_i, \boldsymbol{\beta})$ fits the data (x_i, y_i), the least squares fitting method consists in minimising the sum of squares, that is:

$$S(\boldsymbol{\beta}) = \sum_{i=1}^{m} e_i^2$$

$$\text{with } e_i = y_i - f(x_i, \boldsymbol{\beta})$$

For very simple models, a simple method is used, called gradient descent. It consists in altering $\boldsymbol{\beta}$ at each iteration in the following fashion:

$$\boldsymbol{\beta}_{i+1} = \boldsymbol{\beta}_i - \alpha \nabla_{\boldsymbol{\beta}} e_i$$

this means that at each iteration we take a step proportional to the gradient of the error function e_i, evaluated for every (x_i, y_i). This method could be improved by using the second derivative of the error function, but doing so is computationally expensive because of the calculation of the Hessian matrix.
A common approximation is to linearise f, using a first-order Taylor expansion:

$$f(x_i, \boldsymbol{\beta}) \approx f(x_i, \boldsymbol{\beta}_0) + (\boldsymbol{\beta} - \boldsymbol{\beta}_0) \frac{\partial f(x_i, \boldsymbol{\beta}_0)}{\partial \boldsymbol{\beta}}$$

This is the Gauss-Newton (GN) method, which is essentially approximating the least square function S as quadratic, approximating the Hessian $\boldsymbol{H}$ to a simpler expression, with the following update rule:

$$\boldsymbol{\beta}_{i+1} = \boldsymbol{\beta}_i - \boldsymbol{H}^{-1}\boldsymbol{d}$$

where $\boldsymbol{d} \propto \nabla_\beta e$.

The quadratic approximation is not always an improvement on gradient descent since it requires to be close to a minimum. Levenberg made a contribution to the situation by creating a model that allows to transition between the two behaviours [109],

$$\boldsymbol{\beta}_{i+1} = \boldsymbol{\beta}_i - (\boldsymbol{H} + \lambda \boldsymbol{I})^{-1}\boldsymbol{d}$$

When λ is small, it approaches the GN approximation. When large, it is close to gradient descent with

$$\boldsymbol{\beta}_{i+1} = \boldsymbol{\beta}_i - \frac{1}{\lambda}\boldsymbol{d}$$

When running the fitting algorithm, the value of λ is tuned. If the error increases from the previous step, this means the quadratic approximation is not well suited. We reduce the value of λ, placing more emphasis on the gradient descent, after reverting to the previous value of $\boldsymbol{\beta}$.
If the sum of squares decreases, the approximation works and we want to increase its effect, so we decrease λ and continue updating.

Marquardt noticed [110] that when λ is large, the information of the Hessian does not play a role in the update as it is negligible compared to λ. By replacing the identity matrix with the diagonal of the Hessian,

$$\boldsymbol{\beta}_{i+1} = \boldsymbol{\beta}_i - (\boldsymbol{H} + \lambda \cdot diag(\boldsymbol{H}))^{-1}\boldsymbol{d}$$

we favour the direction along which the gradient is small, an improvement on the regular gradient descent. This Levenberg-Marquardt method is widely used in science. It is a heuristic method (not optimal) and works well in practice.
It is well suited for medium-sized problem, but when the number of parameters is too large, the cost of matrix inversion becomes too high and other methods are preferred.

LIST OF REFERENCES

[1] K. I. Wysokinski. Remarks on the first hundred years of superconductivity. *ArXiv e-prints*, November 2011.

[2] P. Drude. Zur elektronentheorie der metalle. *Annalen der Physik*, 306(3):566–613, 1900.

[3] W. Meissner and R. Ochsenfeld. Ein neuer Effekt bei Eintritt der Supraleitfähigkeit. *Naturwissenschaften*, 21:787–788, November 1933.

[4] M. Tinkham. *Introduction to Superconductivity: Second Edition (Dover Books on Physics)*. Dover Publications, second edition edition, June 2004. ISBN 0486435032.

[5] F. London and H. London. Supraleitung und diamagnetismus. *Physica*, 2(112):341 – 354, 1935.

[6] V. L. Ginzburg and L. D. Landau. On the theory of superconductivity. *Zh. Eksp. Teor. Fiz*, 20: 1064–1082, 1950.

[7] M. Cyrot. Ginzburg-landau theory for superconductors. *Reports on Progress in Physics*, 36(2):103, 1973.

[8] H. Fröhlich. Theory of the superconducting state. I. the ground state at the absolute zero of temperature. *Phys. Rev.*, 79:845–856, Sep 1950.

[9] E. Maxwell. Isotope effect in the superconductivity of mercury. *Phys. Rev.*, 78:477–477, May 1950.

[10] L. N. Cooper. Bound electron pairs in a degenerate fermi gas. *Phys. Rev.*, 104:1189–1190, Nov 1956.

[11] J. Bardeen, L. N. Cooper, and J. R. Schrieffer. Theory of superconductivity. *Phys. Rev.*, 108:1175–1204, Dec 1957.

[12] U. Mizutani. *Introduction to the Electron Theory of Metals*. Cambridge University Press, 2001. ISBN 9780511612626. Cambridge Books Online.

[13] I. Giaever. Electron tunneling between two superconductors. *Phys. Rev. Lett.*, 5:464–466, Nov 1960.

[14] J. de Launay. The isotope effect in superconductivity. *Phys. Rev.*, 93:661–665, Feb 1954.

[15] A. Chainani, T. Yokoya, T. Kiss, and S. Shin. Photoemission spectroscopy of the strong-coupling superconducting transitions in lead and niobium. *Phys. Rev. Lett.*, 85:1966–1969, Aug 2000.

[16] G. M. Eliashberg. Vzaimodeistvie elektronov s kolebaniyami reshetki v sverkhprovodnike. *h. Eksp. Teor. Fiz.*, 38:966, 1960. [G.M. Eliashberg, Interactions between electrons and lattice vibrations in a superconductor, Sov. Phys. JETP 11(3), 696-702 (1960)].

[17] W. L. McMillan. Transition temperature of strong-coupled superconductors. *Phys. Rev.*, 167:331–344, Mar 1968.

[18] F. Steglich, J. Aarts, C. D. Bredl, W. Lieke, D. Meschede, W. Franz, and H. Schäfer. Superconductivity in the presence of strong pauli paramagnetism: $CeCu_2Si_2$. *Phys. Rev. Lett.*, 43:1892–1896, Dec 1979.

[19] R. Hott, R. Kleiner, T. Wolf, and G. Zwicknagl. Review on Superconducting Materials. *ArXiv e-prints*, June 2013.

[20] J. G. Bednorz and K. A. Mller. Possible high Tc superconductivity in the BaLaCuO system. *Zeitschrift für Physik B Condensed Matter*, 64(2):189–193, 1986.

[21] R. J. Cohn. Record superconductor at 22.3 K. *Physics Today*, 26:17, 1973.

[22] A. B. Pippard. An experimental and theoretical study of the relation between magnetic field and current in a superconductor. *Proceedings of the Royal Society of London A: Mathematical, Physical and Engineering Sciences*, 216(1127):547–568, 1953.

[23] J. S. Chapman. *Macroscopic Models of Superconductivity.* PhD thesis, Oxford University, 1991.

[24] D.-X. Chen, J. A. Brug, and R. B. Goldfarb. Demagnetizing factors for cylinders. *Magnetics, IEEE Transactions on*, 27(4):3601–3619, Jul 1991.

[25] E. H. Brandt. The flux-line lattice in superconductors. *Reports on Progress in Physics*, 58(11):1465, 1995.

[26] L.V. Shubnikov, V. I. Khotkevich, Y. D. Shepelev, and Y. N. Ryabinin. Magnetic properties of superconducting metals and alloys. *Ukrainian Journal of Physics*, 53:42–52, 1957.

[27] A. A. Abrikosov. The magnetic properties of superconducting alloys. *Journal of Physics and Chemistry of Solids*, 2(3):199 – 208, 1957.

[28] V. L. Ginzburg. Nobel lecture: On superconductivity and superfluidity (what I have and have not managed to do). *Rev. Mod. Phys.*, 76:981–998, Dec 2004.

[29] W. H. Kleiner, L. M. Roth, and S. H. Autler. Bulk solution of ginzburg-landau equations for Type II superconductors: Upper critical field region. *Phys. Rev.*, 133:A1226–A1227, Mar 1964.

[30] L. Onsager. Magnetic flux through a superconducting ring. *Phys. Rev. Lett.*, 7:50–50, Jul 1961.

[31] B. S. Deaver and W. M. Fairbank. Experimental evidence for quantized flux in superconducting cylinders. *Phys. Rev. Lett.*, 7:43–46, Jul 1961.

[32] G. M. Braverman, S. A. Gredeskul, and Y. Avishai. Multiquantum vortices in conventional superconductors with columnar defects near the upper critical field. *Phys. Rev. B*, 57:13899–13906, Jun 1998.

[33] G. E. Volovik. Monopoles and fractional vortices in chiral superconductors. *Proc Natl Acad Sci U S A*, 97(6):2431–2436, Mar 2000.

[34] C. P. Poole, H. A. Farach, R. J. Creswick, and R. Prozorov. 6 - Ginzburg-Landau Theory. In Charles P. Poole, Horacio A. Farach, and Richard J. Creswick Ruslan Prozorov, editors, *Superconductivity (Second Edition)*, pages 143 – 169. Academic Press, Amsterdam, second edition edition, 2007. ISBN 978-0-12-088761-3.

[35] W. Friedrich, P. Knipping, and M. Laue. Interferenzerscheinungen bei röntgenstrahlen. *Annalen der Physik*, 346(10):971–988, 1913.

[36] W.L. Bragg. The diffraction of short electromagnetic waves by a crystal. In *Proceedings of the Cambridge Philosophical Society*, volume 17, pages 43–57, 1913.

[37] L. Van Hove. Correlations in space and time and born approximation scattering in systems of interacting particles. *Phys. Rev.*, 95:249–262, Jul 1954.

[38] N. A. Egetenmeyer. *Interplay between superconductivity and magnetism*. PhD thesis, ETH, 2013.

[39] P. G. de Gennes and J. Matricon. Collective modes of vortex lines in superconductors of the second kind. *Rev. Mod. Phys.*, 36:45–49, Jan 1964.

[40] D. Cribier, B. Jacrot, L. Madhav Rao, and B. Farnoux. Mise en evidence par diffraction de neutrons d'une structure periodique du champ magnetique dans le niobium supraconducteur. *Physics Letters*, 9 (2):106 – 107, 1964.

[41] D. Cribier, B. Jacrot, L. Madhav Rao, and B. Farnoux. Chapter IV study of the superconductive mixed state by neutron diffraction. volume 5 of *Progress in Low Temperature Physics*, pages 161 – 180. Elsevier, 1967.

[42] H. London. Proc. lnternat. conf. low temperature physics p. 157. In *Proc. lnternat. Conf. Low Temperature Physics*, page 157, 1951.

[43] F. Pobell. *Matter and Methods at Low Temperatures*. Springer-Verlag Berlin Heidelberg, Reading, MA, 2007.

[44] E. N. Smith and R. C. Richardson. *Experimental techniques in condensed matter physics at low temperatures*. Adv. Book Classics. Addison-Wesley, Reading, MA, 1988.

[45] E. Bauer, G. Hilscher, H. Michor, Ch. Paul, E. W. Scheidt, A. Gribanov, Y. Seropegin, H. Noël, M. Sigrist, and P. Rogl. Heavy fermion superconductivity and magnetic order in noncentrosymmetric $CePt_3Si$. *Phys. Rev. Lett.*, 92:027003, Jan 2004.

[46] G. Bihlmayer, O. Rader, and R. Winkler. Focus on the Rashba effect. *New Journal of Physics*, 17(5): 050202, 2015.

[47] J. Alicea. New directions in the pursuit of Majorana fermions in solid state systems. *Reports on Progress in Physics*, 75(7):076501, July 2012.

[48] K. Maki, H. Y. Kee, and Y. Morita. Triplet superconductivity in a nutshell. *Journal of Superconductivity and Novel Magnetism*, 22(1):71–74, 2009.

[49] P. A. Frigeri, D. F. Agterberg, A. Koga, and M. Sigrist. Superconductivity without inversion symmetry: MnSi versus $CePt_3Si$. *Phys. Rev. Lett.*, 92:097001, Mar 2004.

[50] J Chen, L Jiao, J L Zhang, Y Chen, L Yang, M Nicklas, F Steglich, and H Q Yuan. Evidence for two-gap superconductivity in the non-centrosymmetric compound $LaNiC_2$. *New Journal of Physics*, 15 (5):053005, 2013.

[51] W.H. Lee, H.K. Zeng, Y.D. Yao, and Y.Y. Chen. Superconductivity in the ni based ternary carbide $LaNiC_2$. *Physica C: Superconductivity*, 266(1):138 – 142, 1996.

[52] S. Kuroiwa, Y. Saura, J. Akimitsu, M. Hiraishi, M. Miyazaki, K. H. Satoh, S. Takeshita, and R. Kadono. Multigap superconductivity in sesquicarbides La_2C_3 and Y_2C_3. *Phys. Rev. Lett.*, 100:097002, Mar 2008.

[53] E. Bauer and M. Sigrist. *Non-Centrosymmetric Superconductors: Introduction and Overview*. Springer-Verlag Berlin Heidelberg, 2012. ISBN 978-3-642-24623-4.

[54] Sungkit Yip. Noncentrosymmetric superconductors. *Annual Review of Condensed Matter Physics*, 5 (1):15–33, 2014.

[55] A. D. Hillier, J. Quintanilla, and R. Cywinski. Evidence for time-reversal symmetry breaking in the noncentrosymmetric superconductor $LaNiC_2$. *Phys. Rev. Lett.*, 102:117007, Mar 2009.

[56] B. Joshi, A. Thamizhavel, and S. Ramakrishnan. Superconductivity in noncentrosymmetric BiPd. *Phys. Rev. B*, 84:064518, Aug 2011.

[57] P.W. Anderson. Theory of dirty superconductors. *Journal of Physics and Chemistry of Solids*, 11(12): 26 – 30, 1959.

[58] E. M. Forgan, S. J. Levett, P. G. Kealey, R. Cubitt, C. D. Dewhurst, and D. Fort. Intrinsic behavior of flux lines in pure niobium near the upper critical field. *Phys. Rev. Lett.*, 88:167003, Apr 2002.

[59] E. H. Brandt. The vortex lattice in conventional and high-Tc superconductors. *Brazilian Journal of Physics*, 32:675 – 684, 09 2002.

[60] E. H. Brandt and U. Essmann. The flux-line lattice in Type-II superconductors. *physica status solidi (b)*, 144(1):13–38, 1987.

[61] C.J. Bowell, R.J. Lycett, M. Laver, C.D. Dewhurst, R. Cubitt, and E.M. Forgan. Absence of vortex lattice melting in a high-purity Nb superconductor. *Phys. Rev. B*, 82(14):144508, October 2010.

[62] J. E. Sonier. *The Magnetic Penetration Depth and the Vortex Core Radius in Type-II Superconductors*. PhD thesis, University of British Columbia, 1998.

[63] R. Cubitt, E. M. Forgan, G. Yang, S. L. Lee, D. McK Paul, H. A. Mook, M. Yethiraj, P. H. Kes, T. W. Li, A. A. Menovsky, Z. Tarnawski, and K. Mortensen. Direct observation of magnetic flux lattice melting and decomposition in the high-tc superconductor $Bi_{2.15}Sr_{1.95}CaCu_2O_{8+x}$. *Nature*, 365(6445): 407–411, Sep 1993.

[64] J. Kierfeld and V. Vinokur. Lindemann criterion and vortex lattice phase transitions in Type-II superconductors. *Phys. Rev. B*, 69:024501, Jan 2004.

[65] M. Sun, Z.and Enayat, A. Maldonado, C. Lithgow, E. Yelland, D. C. Peets, A. Yaresko, A. P. Schnyder, and P. Wahl. Dirac surface states and nature of superconductivity in noncentrosymmetric BiPd. *Nat Commun*, 6, Mar 2015.

[66] K. Aoyama, L. Savary, and M. Sigrist. Signatures of the helical phase in the critical fields at twin boundaries of noncentrosymmetric superconductors. *Phys. Rev. B*, 89:174518, May 2014.

[67] L. Jiao, J. L. Zhang, Y. Chen, Z. F. Weng, Y. M. Shao, J. Y. Feng, X. Lu, B. Joshi, A. Thamizhavel, S. Ramakrishnan, and H. Q. Yuan. Anisotropic superconductivity in noncentrosymmetric BiPd. *Phys. Rev. B*, 89:060507, Feb 2014.

[68] N. R. Werthamer, E. Helfand, and P. C. Hohenberg. Temperature and purity dependence of the superconducting critical field, H_{c2}. iii. electron spin and spin-orbit effects. *Phys. Rev.*, 147:295–302, Jul 1966.

[69] D. K. Christen, F. Tasset, S. Spooner, and H. A. Mook. Study of the intermediate mixed state of niobium by small-angle neutron scattering. *Phys. Rev. B*, 15:4506–4509, May 1977.

[70] U. Essmann. Observation of the mixed state. *Physica*, 55:83–93, October 1971.

[71] E. H. Brandt and M. P. Das. Attractive vortex interaction and the intermediate-mixed state of superconductors. *Journal of Superconductivity and Novel Magnetism*, 24(1-2):57–67, 2011.

[72] M. Laver, C. J. Bowell, E. M. Forgan, A. B. Abrahamsen, D. Fort, C. D. Dewhurst, S. Mühlbauer, D. K. Christen, J. Kohlbrecher, R. Cubitt, and S. Ramos. Structure and degeneracy of vortex lattice domains in pure superconducting niobium: A small-angle neutron scattering study. *Phys. Rev. B*, 79: 014518, Jan 2009.

[73] S. Mühlbauer, C. Pfleiderer, P. Böni, M. Laver, E. M. Forgan, D. Fort, U. Keiderling, and G. Behr. Morphology of the superconducting vortex lattice in ultrapure niobium. *Phys. Rev. Lett.*, 102:136408, Apr 2009.

[74] P. G. Kealey, T. M. Riseman, E. M. Forgan, L. M. Galvin, A. P. Mackenzie, S. L. Lee, D. McK. Paul, R. Cubitt, D. F. Agterberg, R. Heeb, Z. Q. Mao, and Y. Maeno. Reconstruction from small-angle neutron scattering measurements of the real space magnetic field distribution in the mixed state of Sr_2RuO_4. *Phys. Rev. Lett.*, 84:6094–6097, Jun 2000.

[75] E. H. Brandt. Precision Ginzburg-Landau solution of ideal vortex lattices for any induction and symmetry. *Phys. Rev. Lett.*, 78:2208–2211, Mar 1997.

[76] R. Cubitt, E. M. Forgan, D. M. Paul, S. L. Lee, J. S. Abell, H. Mook, and P. A. Timmins. Neutron diffraction by the flux lattice in high-T_c superconductors. *Physica B Condensed Matter*, 180:377–379, June 1992.

[77] S. J. Blundell. Spin-polarized muons in condensed matter physics. *Contemporary Physics*, 40:175–192, March 1999.

[78] W. Barford and J.M.F. Gunn. The theory of the measurement of the london penetration depth in uniaxial type II superconductors by muon spin rotation. *Physica C: Superconductivity*, 156(4):515 – 522, 1988.

[79] J. S. White, R. W. Heslop, A. T. Holmes, E. M. Forgan, V. Hinkov, N. Egetenmeyer, J. L. Gavilano, M. Laver, C. D. Dewhurst, R. Cubitt, and A. Erb. Magnetic-field-induced nonlocal effects on the vortex interactions in twin-free $YBa_2Cu_3O_7$. *Phys. Rev. B*, 84:104519, Sep 2011.

[80] R. Morisaki-Ishii, H. Kawano-Furukawa, A. S. Cameron, L. Lemberger, E. Blackburn, A. T. Holmes, E. M. Forgan, L. M. DeBeer-Schmitt, K. Littrell, M. Nakajima, K. Kihou, C. H. Lee, A. Iyo, H. Eisaki, S. Uchida, J. S. White, C. D. Dewhurst, J. L. Gavilano, and M. Zolliker. Vortex lattice structure in $BaFe_2(As_{0.67}P_{0.33})_2$ via small-angle neutron scattering. *Phys. Rev. B*, 90:125116, Sep 2014.

[81] R. Prozorov and R. W. Giannetta. Magnetic penetration depth in unconventional superconductors. *Superconductor Science and Technology*, 19(8):R41, 2006.

[82] M. Mondal, B. Joshi, S. Kumar, A. Kamlapure, S. C. Ganguli, A. Thamizhavel, S. S. Mandal, S. Ramakrishnan, and P. Raychaudhuri. Andreev bound state and multiple energy gaps in the noncentrosymmetric superconductor BiPd. *Phys. Rev. B*, 86:094520, Sep 2012.

[83] A. T. Holmes, G. R. Walsh, E. Blackburn, E. M. Forgan, and M. Savey-Bennett. A 17 T horizontal field cryomagnet with rapid sample change designed for beamline use. *Review of Scientific Instruments*, 83(2):–, 2012.

[84] S. R. Foltyn, L. Civale, J. L. MacManus-Driscoll, Q. X. Jia, B. Maiorov, H. Wang, and M. Maley. Materials science challenges for high-temperature superconducting wire. *Nat Mater*, 6(9):631–642, Sep 2007.

[85] B. T. Matthias, T. H. Geballe, S. Geller, and E. Corenzwit. Superconductivity of Nb_3Sn. *Phys. Rev.*, 95:1435–1435, Sep 1954.

[86] A. Godeke. A review of the properties of Nb_3Sn and their variation with A15 composition, morphology and strain state. *Superconductor Science and Technology*, 19(8):R68, 2006.

[87] D. Dew-Hughes. Superconducting A15 compounds: A review. *Cryogenics*, 15(8):435 – 454, 1975.

[88] Cyril Cayron. One-step model of the face-centred-cubic to body-centred-cubic martensitic transformation. *Acta Crystallographica Section A*, 69(5):498–509, Sep 2013.

[89] R. Flükiger, D. Uglietti, C. Senatore, and F. Buta. Microstructure, composition and critical current density of superconducting Nb_3Sn wires. *Cryogenics*, 48(78):293 – 307, 2008. Special Issue: Low-Tc Superconducting Materials.

[90] R. Mailfert, B.W. Batterman, and J.J. Hanak. Low temperature structural transformation in Nb_3Sn. *Physics Letters A*, 24(6):315 – 316, 1967.

[91] J. Zhou, Y. Jo, Z. H. Sung, H. Zhou, P. J. Lee, and D. C. Larbalestier. Evidence that the upper critical field of Nb_3Sn is independent of whether it is cubic or tetragonal. *Applied Physics Letters*, 99(12), 2011.

[92] D. Kapoor and R. N. Wright. Structural characteristics of Nb_3Sn produced by three P/M techniques. *Metallurgical Transactions A*, 11(5):685–692, 1980.

[93] R. Kadono, K. H. Satoh, A. Koda, T. Nagata, H. Kawano-Furukawa, J. Suzuki, M. Matsuda, K. Ohishi, W. Higemoto, S. Kuroiwa, H. Takagiwa, and J. Akimitsu. Magnetic field-induced quasiparticle excitation in Nb_3Sn: Evidence for anisotropic *s*-wave pairing. *Phys. Rev. B*, 74:024513, Jul 2006.

[94] V. G. Kogan, P. Miranović, Lj. Dobrosavljević-Grujić, W. E. Pickett, and D. K. Christen. Vortex lattices in cubic superconductors. *Phys. Rev. Lett.*, 79:741–744, Jul 1997.

[95] H. Kawano-Furukawa, C. J. Bowell, J. S. White, R. W. Heslop, A. S. Cameron, E. M. Forgan, K. Kihou, C. H. Lee, A. Iyo, H. Eisaki, T. Saito, H. Fukazawa, Y. Kohori, R. Cubitt, C. D. Dewhurst, J. L. Gavilano, and M. Zolliker. Gap in KFe_2As_2 studied by small-angle neutron scattering observations of the magnetic vortex lattice. *Phys. Rev. B*, 84:024507, Jul 2011.

[96] Jian Zhou. *The Effects Of Variable Tin Content On The Properties Of A15 Superconducting Nb_3Sn.* PhD thesis, The Florida State University, 2011.

[97] S. Foner and E.J. McNiff Jr. Upper critical fields of cubic and tetragonal single crystal and polycrystalline Nb_3Sn in DC fields to 30 tesla. *Solid State Communications*, 39(9):959 – 964, 1981.

[98] R. Escudero and F. Morales. Point contact spectroscopy of crystals: Evidence of a CDW gap related to the martensitic transition. *Solid State Communications*, 150(1516):715 – 719, 2010.

[99] R. Escudero, F. Morales, and F. Bernes. Specific heat studies of pure Nb_3Sn single crystals at low temperature. *Journal of Physics: Condensed Matter*, 21(32):325701, 2009.

[100] V. Hoffstein and R.W. Cohen. The anisotropic superconducting energy gap of Nb_3Sn. *Physics Letters A*, 29(10):603 – 604, 1969.

[101] V. Guritanu, W. Goldacker, F. Bouquet, Y. Wang, R. Lortz, G. Goll, and A. Junod. Specific heat of Nb_3Sn: The case for a second energy gap. *Phys. Rev. B*, 70:184526, Nov 2004.

[102] Y. J. Jo, J. Zhou, Z. H. Sung, P. J. Lee, and D. C. Larbalestier. Specific heat of Nb_3Sn: The case for a single gap. *APL Mater.*, 2(10), 2014.

[103] J.F. Annett. *Superconductivity, Superfluids and Condensates.* OUP Oxford, 2004.

[104] I. Bonalde, R. L. Ribeiro, K. J. Syu, H. H. Sung, and W. H. Lee. Nodal gap structure in the noncentrosymmetric superconductor $LaNiC_2$ from magnetic-penetration-depth measurements. *New Journal of Physics*, 13(12):123022, 2011.

[105] K. B. Pabitra. Superconductivity group winter science meeting. unpublished, 2015.

[106] T. Reimann, S. Muhlbauer, M. Schulz, B. Betz, A. Kaestner, V. Pipich, P. Boni, and C. Grunzweig. Visualizing the morphology of vortex lattice domains in a bulk type-ii superconductor. *Nat Commun*, 6, Nov 2015. Article.

[107] C. Tarantini, P. J. Lee, N. Craig, A. Ghosh, and D. C. Larbalestier. Examination of the trade-off between intrinsic and extrinsic properties in the optimization of a modern internal tin Nb_3Sn conductor. *Superconductor Science and Technology*, 27(6):065013, 2014.

[108] C. Tarantini and M. Brown. Proposal to the national high magnetic field laboratory. unpublished, 2014.

[109] K. Levenberg. A method for the solution of certain non-linear problems in least squares. *The Quarterly of Applied Mathematics*, 2:164–168, 1944.

[110] D. W. Marquardt. An algorithm for least-squares estimation of nonlinear parameters. *Journal of the Society for Industrial and Applied Mathematics*, 11(2):431–441, 1963.